

CRANFIELD UNIVERSITY

SEBASTIAN GEORG WIRTH

**ENHANCED MICROWAVE IMAGING OF THE
SUBSURFACE FOR HUMANITARIAN DEMINING
APPLICATIONS**

SCHOOL OF INFORMATICS AND SYSTEMS
ENGINEERING

PhD

Academic Year: 2020

Supervisor: Dr. Ivor L. Morrow

May 2020

CRANFIELD UNIVERSITY

SCHOOL OF INFORMATICS AND SYSTEMS
ENGINEERING

PhD

Academic Year: 2020

SEBASTIAN GEORG WIRTH

**Enhanced Microwave Imaging of the Subsurface for
Humanitarian Demining Applications**

Supervisor: Dr. Ivor L. Morrow
May 2020

This thesis is submitted in partial fulfilment of the requirements
for the degree of PhD.

© Cranfield University 2020. All rights reserved. No part of
this publication may be reproduced without the written
permission of the copyright owner.

ABSTRACT

This thesis presents a theoretical analysis and applied evaluation deploying ground penetrating radar (GPR) for landmine detection.

An original contribution has been made in designing and manufacturing a light-weight, low-cost, fully polarimetric antenna system for GPR, enabling easy transportation and assembly. This facilitates extensive use by various smaller communities in remote areas. By achieving the goal of supplying various smaller communities with advanced ground penetrating radar technology the technological standard of landmine detection can be improved beyond existing solutions such as metal detection or manual probing. The novel radar system itself allows detection of various subsurface targets of different shapes and sizes, metallic and non-metallic, in a number of different soils, such as sand, loam or gravel and therefore can be used in versatile environments.

The GPR system has been realised by designing novel light-weight, 3D printed X-band horn antennas, manufactured from single piece plastic then copper electroplated. These antennas are 50% lighter than their commercial equivalents. They are incorporated in an antenna array as a group of four to allow full-polarimetric imaging of the subsurface. High resolution images of landmines and calibration targets were performed in the subsurface over an experimental sand test bed.

For performing subsurface measurements in the near-field, four novel gradient-index (GRIN) lenses were designed and 3D printed to be incorporated in the apertures of the X-band antennas. The improved target detection from these lenses was proven by scanning the test bed and comparing the imaging data of the antenna array with and without lenses

ABSTRACT

attached.

A rigorous theoretical study of different decomposition techniques and their effect on the imaging and detection accuracy for polarimetric surface penetrating data was performed and applied to the gathered imaging data to reliably isolate and detect subsurface targets. Studied decomposition techniques were Pauli decomposition parameters and Yamaguchi polarimetry decomposition. It was found that it is paramount to use both algorithms on one set of subsurface data to detect all features of a buried target.

A novel temporal imaging technique was developed for exploiting natural occurring changes in soil moisture level, and hence its dielectric properties. Contrary to the previously introduced imaging techniques this moisture change detection (MCD) mechanism does not rely on knowledge of the used measurement setup or deploying clutter suppression techniques. This time averaged technique uses several images of a moist subsurface taken over a period while the moisture evaporates from the soil. Each image pixel is weighted by the phase change occurring over the evaporation period and a resulting B-scan image reveals the subsurface targets without surrounding clutter.

Finally, a multi-static antenna set-up is examined on its capability for suppressing surface clutter and its limitations are verified by introducing artificial surface clutter in form of pebbles to the scene. The resulting technique was found to suppress up to 30

The GPR antenna system developed in this thesis and the corresponding imaging techniques have contributed to a significant improvement in subsurface radar imaging performance and target discrimination capabilities. This work will contribute to more efficient landmine clearance in some of the most challenged parts of the world.

Acknowledgements

Firstly, I would like to thank my parents. Without their love, patience and encouragement over the last 32 years I would not be where I am now and none of this work would have been possible. Thank you, Mum and Dad, for all that you do for me.

Thank you to my supervisors, Dr. Ivor Morrow and Dr. Daniel Andre. You have both been incredibly supportive and understanding throughout my time as a PhD student and I deeply appreciate your sharing of your experience, knowledge and ideas with me. In addition, thank you John Economou for chairing my review meetings and thank you Stephen Hobbs for the given advise and reviewing my thesis.

I would also like to thank my fellow students, friends, colleagues and family for their support, discussions and banter over the course of my studies. Thank you all for all the good times, and thank you for being there during the hard times. You have all contributed more to this research than you know.

Finally, I would like to thank the Sir Bobby Charlton charity *Find A Better Way* for funding this PhD studentship under the DETERMINE research programme and making this work possible and also the support of the Defence Academy of the UK who had made available to us the devices employed in the project.

TABLE OF CONTENTS

ABSTRACT	3
ACKNOWLEDGMENTS	5
LIST OF FIGURES	10
LIST OF TABLES	13
LIST OF ABBREVIATIONS	14
LIST OF SYMBOLS	16
1 INTRODUCTION TO THE RESEARCH	1
1.1 Background and Motivation	1
1.2 Types of land-mines	6
1.3 Minefields	8
1.4 Common Detection Methods used for Humanitarian Demining	9
1.4.1 Manual Techniques	9
1.4.2 Electromagnetic Induction	9
1.4.3 X-Ray Backscattering Method	11
1.4.4 Neutron Backscattering Techniques	11
1.4.5 Biological Methods	11
1.4.6 Acoustic and Ultrasound Techniques	13
1.4.7 Infrared Technique	13
1.4.8 Ground Penetrating Radar	13
1.5 Aims and Objectives	14
1.6 Thesis Outline	16
1.7 Original and Novel Contributions	18
1.8 Summary	20
1.9 Publications Arising from this Research	21
1.9.1 Journal Papers	21
1.9.2 Conference papers	21

TABLE OF CONTENTS

REFERENCES	24
2 ULTRA-WIDEBAND TECHNIQUE FOR DEMINING SCANNING SYSTEMS	27
2.1 Background	27
2.2 The Radar Range Equation	33
2.2.1 GPR Range Equation	34
2.3 Radar Waveform Types	35
2.4 UWB Waveform Capability	36
2.4.1 Penetration Depth	36
2.4.2 Range Resolution	39
2.4.3 Processing Technique	43
2.5 Preliminary Characterisation of Soil and Targets	45
2.5.1 Experimental Setup	45
2.5.2 Permittivity Measurements	48
2.5.3 Monostatic RCS of APMs	52
2.6 Summary Comments	55
REFERENCES	58
3 ADDITIVE MANUFACTURED ANTENNAS FOR GPR	60
3.1 Introduction	60
3.2 System Requirements	62
3.2.1 Efficiency	64
3.2.2 Sensitivity Factor	64
3.2.3 Ultra Wideband	65
3.3 Antennas for Ground Penetrating Radar	65
3.3.1 Spiral Antennas	65
3.3.2 Crossed Dipoles	66
3.3.3 Vivaldi Antennas	67
3.3.4 Dielectric Rod Antennas	67
3.3.5 Horn Antennas	68
3.4 Novel Fabrication Techniques	69
3.4.1 Construction	69
3.4.2 Additive Manufactured Horn Antenna	70
3.5 Design of an additive manufactured X-band horn antenna	71
3.5.1 Analytic Equations and Results	71
3.5.2 Antenna Simulation	74
3.5.3 Antenna Manufacture	76
3.6 Horn Antenna Array	83
3.7 Summary Comments	85
REFERENCES	86

TABLE OF CONTENTS

4	ADDITIVE MANUFACTURED LENSES FOR GPR	90
4.1	Lenses For Millimeter Wave Applications	91
4.1.1	Analytic Equations and Results	92
4.1.2	Lens Manufacture	95
4.2	Results of Antenna and Lens Integration	97
4.3	Polarimetric Near-field SAR and First Results	100
4.4	Summary Comments	102
	REFERENCES	104
5	ADVANCED POLARIMETRY FOR SUBSURFACE IMAGING	106
5.1	Introduction	106
5.2	Polarised Wave	107
5.2.1	Jones Vectors	107
5.2.2	Scattering Matrix	109
5.2.3	Stokes Parameters	110
5.3	Pauli Decomposition Parameters	112
5.4	Yamaguchi Polarimetry Decomposition	112
5.5	The Experiments	116
5.5.1	Experiment 5 A - Low Band Configuration	116
5.5.2	Experiment 5 B - High Band Configuration	123
5.6	Discussion	127
5.6.1	Experiment 5 A - Low Band Configuration	128
5.6.2	Experiment 5 B - High Band Configuration	131
5.7	Summary Comments	134
	REFERENCES	135
6	TEMPORAL IMAGING FOR GROUND PENETRATING RADAR	136
6.1	Introduction	136
6.2	The Dobson Four Component model	138
6.3	Experiment 6 C - High Band Moisture Change Detection	140
6.3.1	Experimental Setup	140
6.3.2	Methodology	142
6.4	Analysis	143
6.4.1	Data Collection	143
6.4.2	Moisture Change Detection	144
6.4.3	Phase Weighted Imagery	146
6.5	Differential Interferometric Polarimetry	147
6.6	Summary Comments	150
	REFERENCES	151

TABLE OF CONTENTS

7	MULTISTATIC POLARIMETRY IN CLUTTERED GROUND	153
7.1	Introduction	153
7.2	Methodology	155
7.2.1	Multi-static Measurement Description	157
7.3	The Experiments	160
7.3.1	Experiment 7 D - Multistatic Full Polarimetry Configuration	160
7.3.2	Experiment 7 E – Multistatic Full Polarimetry in Ground Clutter	161
7.4	Results and Performance Discussion	163
7.4.1	Experiment 7 D - Multistatic Full Polarimetry Configuration	163
7.4.2	Experiment 7 E - Multistatic Full Polarimetry in Clutter	166
7.5	Polarisation Ratios	166
7.6	Summary Comments	170
	REFERENCES	171
8	CONCLUSIONS AND FUTURE WORK	172
8.1	Research Summary	172
8.2	Future Research	174
	APPENDICES	177
A.1	Antennas	178
A.1.1	Spiral antenna papers	179
A.1.2	Crossed dipole papers	180
A.1.3	Horn antenna papers	182
A.1.4	Vivaldi antenna papers	183
A.1.5	Dielectric rod antenna papers	184
A.1.6	Lense papers	185
A.1.7	3D printed antenna papers:	186
	REFERENCES	189

LIST OF FIGURES

1.1	Metal detector used for demining operation. Picture from arnehodalic.com . .	4
1.2	Land-mines: L10 Ranger, Valmara 59, TS-50	7
1.3	Landmines: PFM-1, PMN-1, Surrogate Schuhbox	8
1.4	Metal detector used for demining operation. Picture from Igarapé Institute. .	10
1.5	African giant pouch rat. Photo from hi-us.org	11
1.6	Dog used in demining operation. Photo from hi-us.org	12
2.1	Ground penetrating radar block diagram	29
2.2	Noon criterion: limit of resolution for two point scatters [10]	41
2.3	(a) Calibration targets and antenna head, (b) Sketch of measurement setup, (c) Laboratory scene (d) Landmine 1 is an Italian TS-50 landmine, (e) Landmine 2 is a Russian PMN-1 landmine.	47
2.4	Section of coaxial airline filled with an annular bead of sample material (taken from [15])	48
2.5	Eletron microscope images of ground sand, soil (loam) and gravel samples. .	50
2.6	Photograph of coaxial waveguide system setup with ground samples in flasks.	51
2.7	Photograph of coaxial waveguide system with sample holder filled with sand.	52
2.8	Ball bearing (30 mm) on cup used for system calibration measurement. . . .	54
2.9	Ball bearing (30 mm) on cup used for system calibration measurement. . . .	55
3.1	Pyramidal horn and coordinate system.	73
3.2	Schematic design of the 3D printed Pyramidal horn antenna (a) end view (b) side view.	73
3.3	Calculated principal E and H radiation patterns for the Pyramidal Horn antenna.	74
3.4	HFSS simulation of antenna phase centre for the Pyramidal horn antenna. . .	76
3.5	Horn antenna apertures showing different conductive surface finishes applied (a) Zinc, (b) Copper tape, (c) Copper spray and (d) Copper electroplating. . .	78
3.6	Simulated and measured optimum feed length.	79
3.7	Measured reflection coefficient responses S_{11} for the Pyramidal horn for different metal coating applied.	79
3.8	Additive manufactured and copper electroplated horn antenna.	80

LIST OF FIGURES

3.9	Simulated and measured radiation patterns of the manufactured pyramidal horn antenna in the E-plane and H-plane over the 8-12 GHz frequency range (measured data only covers 0-180°).	82
3.10	(a) Measured and simulated antenna gain, (b) Measured and simulated reflection coefficient.	83
3.11	(a) Polarimetry array incorporating two 3D printed horn antennas (1, 2) and two commercial horns (3, 4) (b) S_{11} measured at the terminals of the horns.	84
3.12	(a) Co- and cross-polar mutual antenna coupling in E-plane, (b) Co- and cross-polar mutual antenna coupling in E-plane.	84
4.1	Sketch showing the constant thickness lens composed of annular rectangular ring of decreasing dielectric constant material.	92
4.2	Comparison of effective permittivity model prediction and measured permittivity for PLA and air over a range of volume fractions.	94
4.3	Photograph of the rectangular printed flat GRIN lens.	96
4.4	Measured and simulated reflection coefficient of 3D printed horn antenna with and without near-field lens.	98
4.5	Measured and simulated gain of 3D printed horn antenna with and without near-field lens.	98
4.6	(a) S_{11} measurement of all four antennas in the array without lenses attached to antenna apertures, (b) S_{11} measurement of all four antennas in the array with lenses attached to antenna apertures.	99
4.7	(a) Co- and cross-polar mutual antenna coupling in E-plane, measured with lenses attached to antenna apertures, (b) Co- and cross-polar mutual antenna coupling in E-plane, measured with lenses attached to antenna apertures.	99
4.8	Polarimetry array incorporating two 3D printed horn antennas (1, 2) and two commercial horns (3, 4).	101
4.9	Laboratory sand bay with several calibration objects(A = sphere, B = dihedron, C = trihedron) and a PMN-1 landmine (D).	102
4.10	B-scans without lenses attached.	103
4.11	B-scans with lenses attached.	103
5.1	Poincare Sphere. [2]	110
5.2	(a) Calibration targets and antenna head, (b) Sketch of measurement setup, (c) Laboratory scene (d) Landmine 1 is an Italian TS-50 landmine, (e) Landmine 2 is a Russian PMN-1 landmine.	118
5.3	Schematic diagram illustrating the polarimetric correction calibration procedure, using a brass rod inclined on the horizontal at 22.5°.	120
5.4	Difference in phase Φ_c and amplitude A_c of 20 increments away from calibration target	121
5.5	Calibrated low band B-scans, indicating a sphere (40 mm) and a brass rod as calibration targets as well as two landmines where landmine 1 is an Italian TS-50 landmine and landmine 2 is a Russian PMN-1 landmine.	122

LIST OF FIGURES

5.6	(a) Sketch of high band experimental setup and scene with calibration targets indicated, (b) Dihedral used in the scene, (c) Trihedral used in the scene, (d) TS-50 landmine used in the scene.	125
5.7	Calibrated high band B-scans.	126
5.8	Top: Stokes parameters I_0 and Q , Bottom: I_v and I_h	128
5.9	(a) Pauli a, (b) Pauli b, (e) Pauli c.	129
5.10	Co- and cross-polar polarimetric clutter suppression.	130
5.11	Top: Stokes parameters I_0 and Q , Bottom: I_v and I_h	131
5.12	(a) Pauli a, (b) Pauli b, (e) Pauli c.	132
5.13	Co- and cross-polar polarimetric clutter suppression.	133
6.1	Computed complex dielectric constant for a range of moisture levels for sandy soil (% by volume water at 21.5°C).	139
6.2	Schematic diagram and photo showing a view of the experimental radar scene (units in cm).	141
6.3	Structure of data stored in each polarimetry data cube.	143
6.4	B-scan image of the radar scene, indicating a sphere (40 mm), two dihedrals (70 mm), a trihedral and a TS-50 landmine.	144
6.5	Observed experimental phase change of the trihedral and TS-50 landmine over all time lapsed scans.	145
6.6	Summed magnitude weighted differential phase contrast B-scan ($\alpha = 1$). . .	147
6.7	Co- and cross-polar DinPol results, indicating a sphere (40 mm) and a brass rod as calibration targets as well as two landmines where landmine 1 is an Italian TS-50 landmine and landmine 2 is a Russian PMN-1 landmine. . . .	149
7.1	A range of views of the multi-static full polarimetric GPR setup.	155
7.2	(a) Multistatic polarimetric antenna array (b) Monostatic polarimetric antenna array. The distance between the bistatic array was 72 cm and the array heads were 35.5 cm above the surface of the sand.	157
7.3	Radar scene and schematic diagram of object locations (Dimensions in cm). .	159
7.4	Random pebble surface clutter distributions above the buried PMN-2 anti-personnel landmine.	162
7.5	Calibrated VV and VH B-scans.	164
7.6	Calibrated HH and HV B-scans.	165
7.7	Calibrated VV B-scans.	167
7.8	Calibrated VV B-scans.	168

LIST OF TABLES

1.1	Specifications for land-mines depicted in figure 1.2	8
1.2	Specifications for land-mines depicted in figure 1.4	8
2.1	Separation of two pulses by their bandwidth and range bins accordingly. . . .	40
2.2	Landmine thickness and its required bandwidth for appropriate range resolution	43
2.3	Measured dielectric properties of sand samples dry and at 10% moisture level.	53
2.4	Near-field RCS(dB) measured in VV	55
3.1	Dimensions of the Pyramidal antenna shown in Figure 3.2 (units in mm). . .	74
4.1	Summary design data on the GRIN lens. Tabulated values of lens thickness versus annular rectangular section radius, effective dielectric constant and PLA/air volume fractions for the seven annular sections (the * value indicates a suspect T value)	94
5.1	Polarimetric response of objects in the radar scene.	121
7.1	Polarimetric response of objects in the radar scene.	160
7.2	List of surface clutter experiments conducted.	161
7.3	List of polarisation ratios for sphere and a buried landmine at 45° and 0° . . .	169

LIST OF ABBREVIATIONS

AGI	Air-Ground Interface
AP	Anti Personnel
AT	Anti Tank
ERW	Explosive Remnants of War
FFT	Fast Fourier Transform
GPR	Ground Penetrating Radar
GUI	Graphical User Interface
IFFT	Inverse Fast Fourier Transform
MATLAB	MATrix LABoratory
MCD	Moisture Change Detection
RCS	Radar Cross Section
RDX	Research.Department.Explosive (cyclonite)
RFI	Radio Frequency Interference
RMS	Root Mean Square
SAR	Synthetic Aperture Radar
SCR	Signal to Clutter Ratio
SMC	Soil Moisture Content
SNR	Signal to Noise Ratio
UN	United Nation

LIST OF ABBREVIATIONS

UWB	Ultrawide-Band
UXO	UneXploded Ordinance

LIST OF SYMBOLS

\vec{E}	electric field vector
\vec{H}	magnetic field vector
α	attenuation factor
γ	complex propagation constant
k	propagation constant
k_0	= free space propagation constant
$\omega\sqrt{\mu_o\epsilon_o}$ $k_{x/y,m}$	modal transverse wavenumber
$\mu_o = 4\pi \times 10^{-7}$	permeability
μ_r	relative material permeability
$\epsilon_o = 8.87 \times 10^{-12}$	free space permittivity
ϵ_r	relative permittivity
ϵ_{eff}	effective permittivity
ϵ	complex permittivity
ϵ_r'	real part complex permittivity
ϵ_r''	Imaginary part complex permittivity
f	frequency
λ	wavelength
γ	complex reflection coefficient

LIST OF SYMBOLS

h	substrate height
R	distance from origin to observation point
θ	theta
ϕ	phi
σ	conductivity
η	radiation efficiency of antenna
$Z_o = 377$	free space impedance, Ω
Z_s	surface impedance
ω	radian frequency

Chapter 1

Introduction to the Research

This chapter covers the background and motivation for this research thesis. The first part of the chapter presents a general introduction to the global challenge and scourge of landmines. The landmine detection problem is defined in terms of their geometric and electromagnetic material composition and the material properties of the environments in which they are deposited. The current techniques and sensors used for humanitarian demining are described and compared and contrasted with each other. The main research questions and the objectives are stated, as are the areas of novelty and original contributions and the structure of the thesis is outlined.

1.1 Background and Motivation

On the first of March 1999, the 'Ottawa Convention' on the prohibition of the use, stockpiling, production and transfer of anti personnel land-mines (AP mines), and on their destruction entered into force. By 2019 the treaty was ratified by 164 countries world-wide. Countries that have not signed the treaty include the United States, China, Russia, India and Pakistan [1]. Today, about 60 million of uncleared anti personnel mines and anti tank mines (AT mines) can be found in more than 60 countries. From 9000 casualties in the late 1990s cases

1. INTRODUCTION TO THE RESEARCH

dropped to under 4000 in 2015 but then sharply rose again to a high of 9437 in 2016 and a slightly lower number of 7239 casualties in 2017 [2]. This reversal is mostly due to recent conflicts in Syria, Iraq, Yemen and Ukraine [3].

Land-mines have a far-reaching impact on the people living in those affected countries. In Cambodia, for example, the estimated number of amputee's is 36.000, which is, in other words, 1 amputee for every 236 citizens.

The presence of land-mines not only directly affects people's health, but has also a negative influence on the economic life of the country, by preventing access to precious rural land and other resources. For the particular example of Mozambique it was estimated that the GDP per capita in 2015 could have been up to 25 % lower without landmine clearance [4]. So it is clear that, even if the 'Ottawa Convention' can prevent new mines to be laid, there is a real and even more challenging problem to be solved: the reduction of landmine contaminated areas and the assistance to mine victims. One aspect in this challenge is the detection, identification and clearance of land-mines, called humanitarian demining. Humanitarian demining differs from military mine clearance operations in many aspects. The military mine clearance as applied in conflict situations accepts low rates of clearance efficiency and a higher rate of casualties. For these purposes it is often sufficient to punch a path through a minefield. The costs of these kinds of operations is usually not an issue, time is. For the humanitarian demining purposes, on the contrary, a high clearance efficiency is required (99.6% is required by UN [5]). This can until now only be achieved using the hand clearing method. Also the cost of the clearance operation and the safety of the deminers becomes important. In this work, only humanitarian demining will be considered.

In present-day situations the classical humanitarian demining is done using metal detectors and prodding sticks, to manually detect and clear the mines. The demining procedure varies in function of the mine clearance scenario, depending on the climate, the type of vegetation, the variety of mines, etc. The usual procedure, which might slightly vary to the given

1. INTRODUCTION TO THE RESEARCH

circumstances, is as follows: The deminers work in groups of two and in corridors of 1 m large. In a first stage deminer #2 is on stand-by at a safety distance behind deminer one. Deminer #1 starts with the execution of the tripwire drill, using a long stick. He will lift the stick up and look for wires. When there is no danger he cuts the vegetation. Deminer one will then step back and the demining process is proceeded by deminer #2. Deminer #2 manually scans with a metal detector an area of one meter large and 50 cm wide. When no signal is given, the zone is declared mine free and the procedure will start all over again. If there is a signal, deminer two will try to localise and mark the exact position of the signal. Deminer #2 will then step back and deminer #1 comes in again. He will probe the marked area, i.e. finding the object by sticking a dagger every 2 cm carefully in the ground and gently remove the topsoil from the suspicious object (1.1). This way the exclusion is made between a false target (false alarm) and a mine, and if it is a mine, its actual position and circumference is determined. The process is continued by excavating carefully the ground around the mine and by marking it with a red 'minedanger' tetrahedron. The lane is now closed and the two deminers will continue on another lane. At the end of the day the explosion team will destroy all the detected mines in-situ, to make sure the mines will not enter in circulation again.

A platoon of 30 well-trained deminers is able to demine approximately between 500 and 2500 m^2 a day. This method has not been changed since the Second World War.

The manual demining procedure is very time consuming and not without danger. Hence, manual demining is extremely costly. It has been estimated that an average of 1000 US \$ is needed for a manual demining of the 3 US \$ mine [6]. The reason for it is the high false alarm rate of the metal detector. For each piece of metal detected by the metal detector, the procedure with the first deminer is initiated. Minefields are often situated in post conflict areas where the contamination with metal can be very high (grenade fragments, cartridges, etc.). Typical values are 100 false alarms for 1 real mine. There is an obvious need for a more efficient portable demining device in order to achieve a more cost-effective demining

1. INTRODUCTION TO THE RESEARCH



Figure 1.1: Metal detector used for demining operation. Picture from arnehodalic.com

process.

Mine detector requirements

1. Detect mines with metal casing, as well as mines with low metal content
2. Detect both, anti-tank and anti-personnel mines
3. Meet the UN-norm safety requirement of 99.6% clearance efficiency
4. Detect mines in all kinds of soils
5. Detect mines from 0 cm (surface laid) up to a of depth of 20 cm
6. Work on rough, vegetation overwhelmed terrain
7. Work in all seasons, in all climatic conditions
8. Be able to operate 8 hours a day, 250 days a year
9. For safety reasons be held some cm above the ground

1. INTRODUCTION TO THE RESEARCH

10. Be light weighted
11. Be reliable (mean time between failure of at least 1000 hours and a reliable self test)
12. Not interfere with other sensors when used within 10 m from each other
13. Be easy to maintain
14. Be simple to use (for local people, having a minimum of special training)
15. Have a reasonable false alarm rate, in the order of 20 to 1.

The only technique that does meet almost all of these requirements (except requirement 15) is the combination of the metal detector and the prodding stick, but, as already mentioned, this method is too slow and not without risk. The demining community is well aware of this problem and of the lack of good alternative mine detectors. Therefore, there is a call from the demining community towards the scientific world to contribute in solving this world-wide problem by looking to new and better demining techniques.

It is necessary for a more cost-effective mine clearance method, to obtain for a given probability of detection a lower probability of false alarm. Such an improvement can be achieved in two ways: first it is always possible to enhance existing sensors or to investigate new sensor techniques. Secondly an improvement can be found in fusing the data of different sensors. It is commonly accepted by the research community that data fusion will be indispensable if all of the user requirements have to be satisfied in all scenarios of demining.

1. INTRODUCTION TO THE RESEARCH

Find A Better Way

Find A Better Way was founded in 2011 by England and Manchester United legend Sir Bobby Charlton. Sir Bobby Charlton's visit to Cambodia moved him to set up Find A Better Way as he felt, that with modern technological advances, there had to be a more efficient way of negating the effects of mines and improving safety for local communities whose lives are blighted by them. With significant amount of funding already committed to a portfolio of nine research projects at leading UK universities, Find A Better Way acts as a major funding body for vital, ground-breaking technological research into improving the tools available for the safe removal of land-mines and explosive remnants of war.

1.2 Types of land-mines

Generally, landmines can be classified according to their design or their targets. Classification according to targets includes anti personnel land-mines and anti vehicle landmines. Every land-mine consists of three components. These are, firstly, the casing, which can be metal, wood, plastic or a combination of materials. Secondly the explosive material, which may be TNT, RDX, TNT and RDX mixed, Tetryl or other high explosive material. Thirdly, the initiator, which can be a pressure or pull sensor, an electronic initiator or other kind of sensors.

The land-mine designs can be broken down to three categories, these are blast, bounding and fragmentation.

1.2.0.1 Blast Land-mines

A blast land-mine is normally shallowly buried and triggered by a pressure sensor, e.g. through treading on or driving over. Blast land-mines require a trigger pressure of approximately 5-16 kg. The main purpose is to harm anything in close proximity through a blast wave. Blast land-mines are not intended to kill, but to maim by destroying a persons foot or leg and often cause secondary damages through bone fragments and dirt being forced into

1. INTRODUCTION TO THE RESEARCH

the wound.

1.2.0.2 Bounding Land-mines

These landmines are usually not fully buried. When activated a propelling charge lifts the mine up about 1.5 metres, which then explodes in order to cause damage to a person's chest and head.

1.2.0.3 Fragmentation Land-mines

These land-mines cause damage through releasing fragments which normally consist from metal or glass. They are either designed to be directional or to distribute fragments in all directions and can injure up to a distance of 200 m and are lethal in close distance.

1.2.0.4 Land-mines used in our research



Figure 1.2: Land-mines: L10 Ranger, Valmara 59, TS-50

1. INTRODUCTION TO THE RESEARCH

Name	L10 Ranger	Valmara 59	TS-50
Diameter	60 mm	102 mm	90 mm
Height	30 mm	196 mm	45 mm
Weight	136 g	3200 g	185 g
Casing	plastic	steel	plastic
Explosive	RXD	Composite B	Composite B
Filling weight	109 g	460-560 kg	50 g
Operating pressure	5 kg	10.8 kg, 6 kg pull	12.5 kg
Origin	UK	Italy	Italy

Table 1.1: Specifications for land-mines depicted in figure 1.2



Figure 1.3: Landmines: PFM-1, PMN-1, Surrogate Schuhbox

Name	PFM-1	PMN-1	Schuhbox
Diameter	90 mm	120	various
Height	61 mm	57 mm	various
Weight	75 g	600 g	various
Casing	plastic	plastic	plywood
Explosive	VS6-D or VS-60D	TNT	TNT
Filling weight	37 g	240 g	200 g
Operating pressure	5-25 kg	5.8 kg	
Origin	Russia	Russia	Germany

Table 1.2: Specifications for land-mines depicted in figure 1.4

1.3 Minefields

There are different ways to lay land-mines. They can either be surface laid or buried, they can be laid manually or distributed. The preferred way to lay land-mines is the manual way,

1. INTRODUCTION TO THE RESEARCH

where they are positioned in patterns of alternating lines of AP (anti-personnel) and AT (anti-tank) mines and then rounded off by a line of barbed wire. The faster way to distribute land-mines is to automatically deploy them from an air plane, a helicopter or a cruise missile. Hence, land-mines might be found in regular patterns or distributed randomly. Sometimes minefields are also booby trapped to make clearance even more difficult. In some cases land-mines might as well be found stacked on each other, that is an AP mine on top of an AT mine. When the war is over mined areas are normally deserted and heavy weather and vegetation causes land-mines to move. This means that land-mines can be found at varies depths or on the surface in different conditions, like corroded or rusted, and often mixed with other objects, e.g. shell casings, barbed wire, beverage cans or shrapnel. What makes clearance even more difficult is that minefields can be encountered in a variety of landscapes, from deserts, mountains, forests to jungle, and a variety of wet or dry soil mixtures.

1.4 Common Detection Methods used for Humanitarian Demining

1.4.1 Manual Techniques

The most widely used method for clearing land-mines is still the manual one. When encountering an unusual object the ground is probed with a 30cm long plastic stick in a 45 degree angle. Visual inspection is used to identify a landmine. This means the person prodding can only inspect the surface and not investigate the subsurface. This method is not very effective, as it is slow and dangerous. Accidental detonation due to the displacement of the land-mine is probable.

1.4.2 Electromagnetic Induction

Electromagnetic induction (EMI) is the principle employed by metal detectors [7]. A metal detector comprises of a transmit and a receive coil. The transmit coil emits a time-varying

1. INTRODUCTION TO THE RESEARCH

magnetic field into the ground to induce eddy currents in nearby metallic objects. The induced current generates a magnetic field in this object which can then be detected by the receiver coil. Metal detectors are used to find land-mines since World War I and the technology has matured. The disadvantage of metal detectors is that mine fields are contaminated with all sorts of metallic objects and these thus generate a high false alarm rate. Furthermore, although metal detectors are able to detect even small amounts of metal fragments, modern land-mines are mostly made from plastic and make it very hard to be detected by just using metal detectors.



Figure 1.4: Metal detector used for demining operation. Picture from Igarapé Institute.

1. INTRODUCTION TO THE RESEARCH

1.4.3 X-Ray Backscattering Method

The X-Ray backscatter method [8][9] involves inducing photons into the ground and receiving the small amount of reflected radiation which varies according to the density and effective atomic number of the material it is induced to. This method suffers from a very weak penetration depth into the ground and a bulky and complex built, as well as hazardous radiation.

1.4.4 Neutron Backscattering Techniques

Neutron Backscattering (NBS) [10] is a well-established technique to find hydrogen, nitrogen and carbon in an object. It can be applied in land-mine detection by taking advantage of the fact that explosive material is abundant in hydrogen. Their drawbacks are a long processing time and operational limitations due to their size, weight and operating power.

1.4.5 Biological Methods



Figure 1.5: African giant pouch rat. Photo from hi-us.org

One of the most efficient ways to find land-mines is to train animals to sniff the explosives. Dogs (figure 1.6) are a well known example [11]. They can easily be trained to be used either in free ranging mode or working on a lead. They are perhaps more reliable than other animals. The problem with dogs is that their performance varies and highly depends on how

1. INTRODUCTION TO THE RESEARCH

often they were trained, by whom they have been trained and on the experience of the handler. Moreover, dogs that are trained to detect larger amounts of explosives are not necessarily able to detect smaller amounts of explosives too and need to be specially trained for that. Another well known animal to detect land-mines is the African giant pouch rat (figure 1.5) [12]. These rats are trained using food rewards to signal the presence of explosives by scratching the ground surface with their feet or by standing up. In Sri Lanka Mongoose are used to find land-mines in combination with a robot they pull [13]. The robot sets the pace and has additional sensors to scan the environment and track the rodent's path. Other animals used to find land-mines are bees [14]. They can easily be trained to find explosives by feeding them around points that have been impregnated with explosive material. Then there are special plants like the arabidosis thaliana that turns red under harsh conditions [15] and is used to indicate contaminated ground or an engineered strain of bacteria that can be sprayed over a mine field [16]. The bacteria is allowed to grow for several hours and fluoresces under ultraviolet light after exposure to explosive material.



Figure 1.6: Dog used in demining operation. Photo from hi-us.org

1. INTRODUCTION TO THE RESEARCH

1.4.6 Acoustic and Ultrasound Techniques

Acoustic waves are commonly used in land-mine detection. In ultrasound detection a sound wave of higher than 20 kHz is sent into the ground. The sound wave is reflected in the boundaries between materials of different acoustic properties. Ultrasound can be used in underwater conditions but encounters problems with the air to ground interface. The acoustic to seismic coupling technique [17][18] is used by vibrating the ground with acoustic or seismic waves. This technique relies on different mechanical properties of buried objects to the ground material.

1.4.7 Infrared Technique

Infrared radiation for land-mine detection [19][20] relies on the fact that land-mines have different thermal properties from the surrounding materials. Normally the ground surface is monitored with IR equipment and scanned for anomalies, like a particular area heating up more than the other. This can either be done passively or an active IR heat source can be used to illuminate the scanned area. This technique is safe, uses lightweight equipment and can scan large areas. The downside is that the performance of IR detection relies a lot on the environment at the time it is monitored. The system is affected by weather conditions, time of the day and the soil the landmine is buried in. Moreover, the limit of detecting buried targets is normally around 15 cm deep, which makes it difficult to detect deeper targets.

1.4.8 Ground Penetrating Radar

Ground Penetrating Radar (GPR) is an electromagnetic technique that is used in applications like archaeology, geology, geoprospecting, surveying and landmine detection, to detect buried objects [21]. Thus, depending on the scan directions 2-D (Bscan) or 3-D (Cscan) images can be formed. In GPR electromagnetic waves are emitted into the ground and the backscattered waves are received and processed. GPR is capable of detecting metallic and

1. INTRODUCTION TO THE RESEARCH

non-metallic objects, since the contrast in electrical properties of buried objects and the surrounding soils are exploited. That means that objects like roots, rocks and other dielectric objects are detected, as well, as the object of interest. These undesired objects are called clutter objects. In non landmine detection applications it is possible to directly couple electromagnetic waves into the ground. This is not possible in humanitarian demining. The detection system has to be elevated above the ground and due to this most of the emitted power is reflected from the air-ground interface before entering the ground. To reduce the loss in power it is desirable to operate as close to the ground as possible, which means we often need to operate in the near-field of the antenna. The choice of the antenna is an important factor in GPR, since the bandwidth determines the depth resolution in the ground. The type of soil that the system is operated in is equally relevant to the system performance, since the attenuation and propagation velocity are dependent on the electrical properties of the soil.

GPR systems traditionally employ narrow (typically ≤ 5) bandwidth and are single polarisation. During the 90's and 00's various national and international humanitarian research programmes resulted in ultra-wideband pulsed and coherent processing radar that were mostly single or exceptionally dual polarised [21]. Similarly antennas research were focussed mainly on ultra-wide band (UWB) pulsed antennas developments [22][23]. While it was recognised that GPR alone would not provide the whole solution to humanitarian demining (high P_d , low P_{fa}), in the last few years, UWB technology has been expressed again as having the potential for delivering demining advances compared to other sensing technologies.

1.5 Aims and Objectives

The objective of this thesis is to contribute toward the evolution of the next generation ground penetrating radar technology for humanitarian demining applications. This embraces critical re-examination on the limitation and advantages of the UWB technique, evolution of new antenna and array systems that exploit the latest design and manufacturing techniques and in-

1. INTRODUCTION TO THE RESEARCH

roducing new capabilities such as capturing full polarisation scattering matrix and providing multi-perspective sensing and imaging.

Specific research questions which the thesis aims to solve;

- Investigate ways to extend the UWB technique and improve or extrapolate down-range resolution.
- The cross-resolution is intimately dependant on the antenna half-power beamwidth and the synthetic aperture algorithm used to focus the beam. Thus if the directive antenna gain can be increased, even by a few dBi, cross-resolution can be improved.
- GPR antenna array are increasingly being used on autonomous near ground and low elevation airborne platforms. The weight of the antenna and or array is a substantial part of the payload. Thus ways to exploit novel additive and or subtractive manufacture techniques that results in light weight, low cost, microwave components and antennas are sought.

Enhancing down and cross-range resolution are significant factors but also equally well known and challenging is alleviating the high levels of clutter which GPR encounter in there operational environment. In order to address the latter issue it is intended;

- To introduce polarisation diversity into the context of GPR for humanitarian demining applications and better understand role of polarisations in treatment of sources of surface and sub-surface clutter. Build an equivalent scattering models appropriate to understanding the underlying physics of the application case and reducing the clutter levels.
- To investigate spatial and temporal diversity into the context of GPR for demining applications and develop the necessary polarimetry scattering theory.

1. INTRODUCTION TO THE RESEARCH

- Develop and apply electromagnetic material formulation theory integrated with environmental parameters such as soil moisture, temperature, and atmospheric pressure with sufficient fidelity to accurately model soil complex permittivity variations with moisture levels.
- Exploring super-resolution imaging techniques based on scattering physics and eigen decomposition methods for measured GPR data.

1.6 Thesis Outline

This thesis is comprised of seven chapters. Following the first chapter which covers the introduction and background to the thesis the content of the remaining chapters can be summarised as follows:

Chapter 2 introduces the radar principles of ground penetrating radar and the ultra-wideband technique and its ability to detect and image small non-metal objects buried in the ground. A brief history and explanation of commonly used waveforms is given including frequency modulated continuous wave (FMCW), pulsed and stepped frequency continuous wave (SFCW). Advantages and disadvantages of the UWB technique are highlighted as they apply to down- and cross-range resolution criteria and to the synthetic aperture radar (SAR) technique. An analytic constant Q and a more accurate Dobson data model fit for electromagnetic propagation in material media are developed and applied with the UWB pulse technique to determine UWB bandwidth, depth of penetration and resolution in different soil medium. Some confirmatory laboratory experiments on the waveform design are made that expose important parameters for the antenna design in the following chapters.

In Chapter 3 a literature review on antennas types used with ground penetrating radar and humanitarian demining in particular is performed. The review is blended with the waveform requirements to evolve two antenna systems; the Low-Band or LB (0.4 - 4.8 GHz) systems is

1. INTRODUCTION TO THE RESEARCH

a non-identical combination of polarimetric antennas consisting of TEM horn transmitter and loop antennas receiver and the; High Band (HB) (8.2-12.4 GHz) composed of an polarimetric array of X-band which are custom designed exploiting 3D printing techniques. The antennas are impedance matched and radiation pattern bandwidth is characterization by measurements and confirmed by analytic and full wave numerical modelling. The cross talk power level when polarimetry arrayed is characterised.

Chapter 4 extends the HB antenna investigation by examining the potential use of 3D additive and or subtractive techniques to develop planar graded refractive index lens (GRIN) for attachment to the horn antenna aperture. This provides two significant operation advantages to the polarimetric array. Firstly, it transforms a spherical wavefront to a planar wavefront and vice versa permitting polarimetry operation in the near-field and secondly it provides some modest antenna gain which enhances the focussing action. Analytic models for the material volume mixing ratios are used to derive 3D unit cells of material and to deduce the radial graded refractive index profile. Equivalent dielectric full wave models confirm the planar lens design operation when attached to pyramidal horn and are in close agreement with experimentally measured results.

In Chapter 5 the full polarimetry data acquisition of the Jones scattering matrix is begun to be exploited to provide power level clutter suppression. The mathematical formalism for the underlying physics of the scattering matrix is described and a null scattering matrix derived in a procedure similar to Yamaguchi to yield co-polar and cross-polar clutter filtered B-scan sub surface imagery. Techniques to evolve other clutter suppressed image products are investigated including Stokes and Pauli eigenvalue decompositions and hybrid co-polar and cross-polar power products. Some novel results with significant suppression of clutter power levels are described.

In Chapter 6 the polarimetric spatial changes measured in multi-temporal data are studied. The highly accurate Dobson soil model is adapted to precisely predict the complex dielectric

1. INTRODUCTION TO THE RESEARCH

changes taking place in the soil as the soil moisture changes. Experiments are conducted to cumulatively observe and plot these microwave electrical phase changes taking place as the soil moisture level change around a buried landmine. The Dobson model confirms the phase changes and a novel sub-wavelength cumulative phase change imaging product is derived that proves very effective at reducing the surface and sub-surface clutter levels. The procedure compares favourably with the results obtained in Chapter 5 and provides a complementary imaging tool to examine the sub-surface.

Chapter 7 determines if simultaneous multi-static/multi-perspective polarimetric imagery of the subsurface can better detect and discriminate buried and obscured targets. This is investigated via a series of experiments in which novel forward and backscattering GPR configurations with differing incidence angles and polarisations are used to acquire data on a range of calibration and buried landmine targets. Furthermore, the effect of increasing sub-surface clutter on the polarimetric performance is examined by gradually introducing pebbles layered on the sand-bay surface. These effects are quantified rigourously via applying polarisation ratios to the data and quantifying the co- and cross-polar responses for different scattering angles, frequencies and polarisation for the different targets.

Chapter 8 Summarises the main finding of the study and discusses the research implications and future work.

1.7 Original and Novel Contributions

Novel contributions to the state-of-the-art in humanitarian demining GPR have been made in the following areas;

- The limitation of ultra-wideband technique for landmine scanning systems has been exposed and the definition of two complementary bandwidth GPR waveforms for improved range resolution defined.

1. INTRODUCTION TO THE RESEARCH

- Experiments demonstrate that discrimination of a landmine by RCS and dual polarimetry alone may not be sufficient to identify landmines. Many commercial manufacturers' GPR while wide bandwidth and dual polar do not fully appreciate this limitation.
- This thesis has pioneered the use of compact and full polarimetric antenna arrays for near-field sensors integrated with novel multistatic GPR configurations. Investigations and feasibility analysis demonstrate exploiting polarimetry and multi-perspective sensing provides major new performance factors not being considered in conventional GPR technology.
- 3D additive manufacturing was used to design light weight, low cost, X-band pyramidal horn antenna suitable for in field assembly. Much novelty and ingenuity was demonstrated in the horn design; it was fabricated as a single item composed of rectangular waveguide, horn flare and a pre-set matching section. After electroplating an SMA launcher is manually interference fitted to the waveguide matching section. The resultant antenna had a measured performance comparable to commercial horn antenna.
- A novel subtractive manufactured lens was fabricated which when attached to the horn antenna apertures provide a spherical to planar wave (near-to-far field) transform function, which permits antenna array close operational proximity to the ground. The lens provides a few dB additional focussing gain which improves further SAR imagery. This is a worlds first ever application of a 3D printed antenna and lens integration demonstrated with subsurface imaging GPR.
- The full polarimetry and multi-perspective antenna arrays, for a first time, enable the full decomposition of GPR scattering matrices. This provides a new paradigm in subsurface imaging, where objects can now be distinguished based not only on qualitative differences in RCS level but quantitative differences in scattering mechanism e.g. sin-

1. INTRODUCTION TO THE RESEARCH

gle and double bounce, characteristic resonance, and quantum polarimetric rotation. Conventional Stokes and Pauli decompositions have been compared with eigen based methods such as Yamaguchi decomposition.

- One final original concept enabled by polarimetry was exploiting spatio-temporal variation in soil moisture levels to provide cumulative differential phase decomposition imaging, or a novel form of temporal super resolution imaging. This was demonstrated to be particularly effective at reducing GPR clutter.

1.8 Summary

While this thesis has been mostly concerned about microwave engineering and signal processing schemes one might equally well argue that the thesis is concerned with the science of techniques for improved down and cross-range resolution or super resolution methods contributing to the next generation of coherent wideband GPR.

1. INTRODUCTION TO THE RESEARCH

1.9 Publications Arising from this Research

1.9.1 Journal Papers

In review:

1. S. Wirth and I. L. Morrow, “Developments in Cutter Suppression Techniques for Microwave Subsurface Imaging ”, IEEE, Geoscience and Remote Sensing Letters. (Chapter 6)
2. S. Wirth and I. L. Morrow, “Additive Manufactured Antennas and Lenses for Multi-static Compact Polarimetric Near-field Microwave Imaging”, IEEE Access. (Chapters 4 and 5)
3. S. Wirth and I. L. Morrow, “Additive Manufacture of Polarimetric Antenna Lens Array for Sub-surface Image Profiling”, MDPI Remote Sensing. (Chapters 5 and 6)

1.9.2 Conference papers

Conference Proceeding:

1. S. G. Wirth, I. L. Morrow and I. Horsfall, “Fabrication procedure and performance of 3D printed X-band horn antenna,” The Loughborough Antennas & Propagation Conference (LAPC 2018), Loughborough, 2018, pp. 1-4, DOI: 10.1049/cp.2018.1481.
2. S. G. Wirth, I. L. Morrow and I. Horsfall, “Near-field microwave imaging using a polarimetric array of 3D printed antennas and lenses,” The Loughborough Antennas & Propagation Conference (LAPC 2018), Loughborough, 2018, pp. 1-6, DOI: 10.1049/cp.2018.1486.
3. S. G. Wirth and I. L. Morrow, “Comparison of polarimetric decomposition techniques to suppress subsurface clutter in GPR applications,” The Loughborough Antennas &

1. INTRODUCTION TO THE RESEARCH

- Propagation Conference (LAPC 2018), Loughborough, 2018, pp. 1-6, DOI: 10.1049/cp.2018.1474.
4. S. G. Wirth and I. L. Morrow, "Effective Polarization Filtering Techniques for Ground Penetrating Radar Applications," 2018 AMTA 2018 Proceedings, Williamsburg, VA, 2018, pp. 1-6, ISBN: 978-1-7281-1290-9.
 5. S. G. Wirth, I. L. Morrow and D. Andre, "Microwave Phase Contrast Imaging of the Subsurface using Variation in Soil Moisture Level," 2018 IEEE MTT-S International Conference on Numerical Electromagnetic and Multiphysics Modeling and Optimization (NEMO), Reykjavik, 2018, pp. 1-4, DOI: 10.1109/NEMO.2018.8503206.
 6. S. G. Wirth and I. L. Morrow, "Near-Field Microwave Sensor Composed of 3D Printed Antennas and Lenses," 2018 IEEE MTT-S International Conference on Numerical Electromagnetic and Multiphysics Modeling and Optimization (NEMO), Reykjavik, 2018, pp. 1-4, DOI: 10.1109/NEMO.2018.8503209.
 7. I. L. Morrow, S. Wirth and M. Finnis, "Discrimination of buried objects using time-frequency analysis and waveform norms," 2016 Loughborough Antennas & Propagation Conference (LAPC), Loughborough, 2016, pp. 1-4, DOI: 10.1109/LAPC.2016.7807605.

Presentations:

1. S. Wirth, I. L. Morrow, D. Andre and M. Finnis, "Can Small Changes in Soil Moisture Provide Enhanced Detection of Buried Landmines", in 2017 at Defence and Security Doctoral Symposium (DSDS) Cranfield University, Swindon Steam Museum, 3-4th Nov.

1. INTRODUCTION TO THE RESEARCH

2. S. Wirth, I. L. Morrow and M. Finnis, “3D Printed Novel Light Weight X-Band Horn Antenna and Lens”, in 2017 at Defence and Security Doctoral Symposium (DSDS) Cranfield University, Swindon Steam Museum, 3-4th Nov.
3. S. Wirth and I. L. Morrow, “Sensing Danger by Digging with Waves”, in 2017 at Cheltenham Science Festival, 3-5th July.
4. S. Wirth and I. L. Morrow, “Near-Field Microwave Sensor Composed of 3D Printed Antennas and Lenses,” in 2018 IEEE MTT-S International Conference on Numerical Electromagnetic and Multiphysics Modeling and Optimization, Iceland, 3-5 Aug.
5. S. G. Wirth and I. L. Morrow, “Effective Polarization Filtering Techniques for Ground Penetrating Radar Applications,” in 2018 AMTA, Williamsburg, USA, 2-4th Oct.

1. INTRODUCTION TO THE RESEARCH

References

- [1] E. Nieves. (2018) The 'Endless War' of land mines in the balkans. [Online]. Available: <https://www.nytimes.com/2018/04/04/lens/the-endless-war-of-land-mines-in-the-balkans.html>
- [2] (2018) Landmine monitor http://www.the-monitor.org/media/2918780/Landmine-Monitor-2018_final.pdf
- [3] P. Mordaunt. (2018) Landmines made by isis undo progress made by princess diana campaign. [Online]. Available: <https://www.theguardian.com/global-development/2018/sep/06/landmines-kill-almost-hourly-penny-mordaunt-princess-diana>
- [4] G. C. et al. (2018) What are the economic effects of landmine clearance? [Online]. Available: <https://voxdev.org/topic/infrastructure-urbanisation/what-are-economic-effects-landmine-clearance>
- [5] (2019) Minefield clearance operations. [Online]. Available: http://www.un.org/Depts/mine/Standard/chap_5.htm
- [6] (2017) Facts about landmines. [Online]. Available: <http://www.landminefree.org/2017/index.php/support/facts-about-landmines>
- [7] C. L. Brown, A. M. Zoubir, I. J. Chant, and C. Abeynayake, "Landmine detection using single sensor metal detectors," in *2002 IEEE International Conference on Acoustics, Speech, and Signal Processing*, vol. 4, May 2002, pp. IV–3948–IV–3951.
- [8] A. A. Faust, R. E. Rothschild, P. Leblanc, and J. E. McFee, "Development of a coded aperture x-ray backscatter imager for explosive device detection," *IEEE Transactions on Nuclear Science*, vol. 56, no. 1, pp. 299–307, Feb 2009.

1. INTRODUCTION TO THE RESEARCH

- [9] W. Dai, W. Mei, and X. Zhao, "Detection and segmentation of concealed objects in x-ray compton backscatter images," in *2013 Seventh International Conference on Image and Graphics*, July 2013, pp. 175–179.
- [10] C. P. Datema, V. R. Bom, and C. W. E. van Eijk, "Landmine detection with the neutron backscattering method," *IEEE Transactions on Nuclear Science*, vol. 48, no. 4, pp. 1087–1091, Aug 2001.
- [11] I. G. M. Ann Göth and J. Trevelyan. How do dogs detect landmines? [Online]. Available: https://www.gichd.org/fileadmin/pdf/publications/MDD/MDD_ch5_part1.pdf
- [12] B. Karin. (2017) These heroic rats detect land mines. now they might help save an endangered anteater. [Online]. Available: https://www.washingtonpost.com/news/animalia/wp/2017/12/22/these-heroic-rats-detect-land-mines-now-they-might-help-save-an-endangered-anteater/?noredirect=on&utm_term=.4782f2dbfb21
- [13] G. Paul. (2017) Man, mongoose, and machine. [Online]. Available: <https://harvardmagazine.com/2008/09/man-mongoose-and-machine.html>
- [14] (2014) 'sniffer bees' reared to detect landmines in balkans. [Online]. Available: <https://www.telegraph.co.uk/news/worldnews/europe/bosnia/10852715/Sniffer-bees-reared-to-detect-landmines-in-Balkans.html>
- [15] N. Laura. (2004) Plants to uncover landmines. [Online]. Available: <https://www.nature.com/news/2004/040129/full/news040126-10.html>
- [16] S. B. et al., "Remote detection of buried landmines using a bacterial sensor," *Nature Biotechnology*, vol. 35, no. 4, pp. 308–310, April 2017.

1. INTRODUCTION TO THE RESEARCH

- [17] H. Kasban, O. Zahran, M. El-Kordy, S. M. Elaraby, and F. E. Abd El-Samie, “Automatic object detection from acoustic to seismic landmine images,” in *2008 International Conference on Computer Engineering Systems*, Nov 2008, pp. 193–198.
- [18] J. M. Sabatier and N. Xiang, “Acoustic-to-seismic coupling and detection of landmines,” in *IGARSS 2000. IEEE 2000 International Geoscience and Remote Sensing Symposium. Taking the Pulse of the Planet: The Role of Remote Sensing in Managing the Environment. Proceedings (Cat. No.00CH37120)*, vol. 4, July 2000, pp. 1646–1648 vol.4.
- [19] N. T. Thanh, H. Sahli, and D. N. Hao, “Infrared thermography for buried landmine detection: Inverse problem setting,” *IEEE Transactions on Geoscience and Remote Sensing*, vol. 46, no. 12, pp. 3987–4004, Dec 2008.
- [20] L. J. Carter, A. Kokonozi, B. Hosgood, C. Coutsomitros, and A. Sieber, “Landmine detection using stimulated infrared imaging,” in *IGARSS 2001. Scanning the Present and Resolving the Future. Proceedings. IEEE 2001 International Geoscience and Remote Sensing Symposium (Cat. No.01CH37217)*, vol. 3, July 2001, pp. 1110–1112 vol.3.
- [21] D. Daniels, *Ground Penetrating Radar - 2nd Edition*. IET, 2004.
- [22] I. Morrow, “Tem horn optimized for transient radiation,” *Microwave and Optical Technology Letters*, vol. 30, pp. 161 – 164, 08 2001.
- [23] I. Morrow, J. Persijn, and P. van Genderen, “Rolled edge ultra-wideband dipole antenna for gpr application,” *IEEE Antennas and Propagation Society, AP-S International Symposium (Digest)*, vol. 3, pp. 484 – 487, 02 2002.

Chapter 2

Ultra-wideband Technique for Demining Scanning Systems

2.1 Background

The ability of radio-waves penetrating the subsurface to detect buried targets was discovered in the early twentieth century. In 1910 Leimbach and Loewy layed out a method of burying dipole antennas in an array of vertical boreholes and measuring the amplitude of neighbouring pairs of antennas. The method described that changes in the conductivity of the materials of the subsurface components between the antennas could be imaged. In 1911, the same researchers examined the use of a radar system which coupled electromagnetic waves directly into the ground to detect subsurface intersections. However, the distance in the subsurface could not yet be measured with the technique described, as for the procedure a continuous waveform (CW) was used. *Huelsbeck et al.* was the first to discover the use of pulsed radar for measuring the distance to a subsurface dielectric target. The first ground penetrating radar survey to be reported was the measuring of the depth of a glacier in 1929 by Stern [1]. Then the use of the technology seemed to have lost interest until the late 1950s. Cook, 1960 of the

2. ULTRA-WIDEBAND TECHNIQUE FOR DEMINING SCANNING SYSTEMS

Southwest Research Institute (SwRI) proposed a VHF pulsed radar (125 MHz mono-cycle) again for measuring ice thickness from an air-plane. From the beginning of the 1970s a lot of commercial applications using GPR are mentioned in the literature, for example by Morey [2]. Most of the systems used during this era were impulse time domain radar systems.

Ground Penetrating Radar is the name for a family of radar systems that image the sub-surface. Some authors prefer to speak of Surface Penetrating Radar (SPR) instead of Ground Penetrating Radar, but there is no essential difference between those two terms. Nowadays, Ground Penetrating Radar is a widely used technique. Ground Penetrating Radar is used to locate pipes and cables in the ground, in civil engineering (bridge inspection, finding voids), in security, for archeology investigation, for geophysical surveying and ice mapping. Ground Penetrating Radar (GPR) could be the most promising technology for humanitarian demining and identification of buried Anti Personnel (AP) land-mines in particular, due to its ability of detecting non-metallic objects in the sub-surface [3][4].

In Ground Penetrating Radar an EM wave is coupled into the ground and the backscattered wave is sampled. An EM wave will be reflected from any electrical parameter contrasts in the subsurface. With GPR it is in particular possible to locate and identify metallic, as well as non-metallic subsurface objects. The relative permittivity ϵ_r of a medium describes the behaviour for the electric field propagation. The relative permeability μ_r describes the behaviour for magnetic field propagation and σ defines the conductivity. All these three macroscopic parameters are in general a function of frequency.

Figure 2.1 shows a block diagram of a general GPR system. The antennas are normally scanned over the surface in close proximity to the ground. An EM wave coupled into the sub-surface will backscatter from any electrical parameter discontinuity. The backscattered waves are then sampled and processed by a receiver. GPR systems always use different antennas for transmit and receive functions. The difficulty of using a single antenna arises because there are no sufficiently fast switches available to protect the receiver from the transmitted power.

2. ULTRA-WIDEBAND TECHNIQUE FOR DEMINING SCANNING SYSTEMS

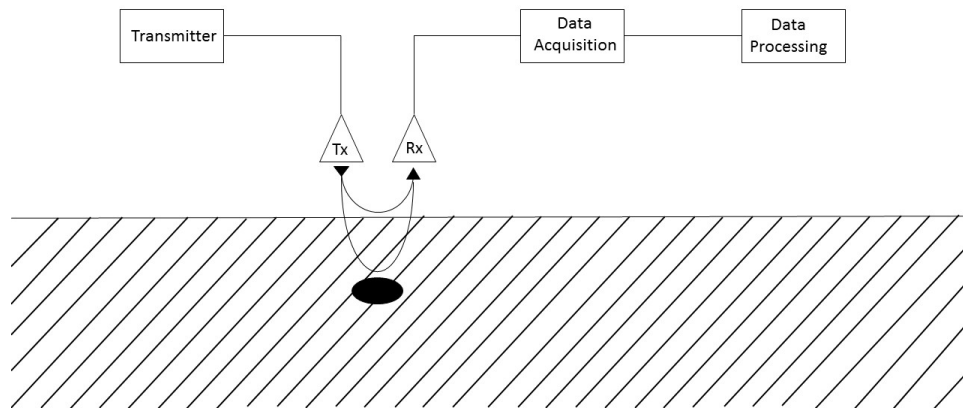


Figure 2.1: Ground penetrating radar block diagram

The first and normally the largest echo of the transmitted signal is due to the air-ground interface. Other echoes, appearing later in time are reflections on target or clutter in the subsurface. Two or three-dimensional images can be produced by moving the antennas on a line or a two dimensional grid. These different types of representation are called A-, B- and C-scans [5].

2. ULTRA-WIDEBAND TECHNIQUE FOR DEMINING SCANNING SYSTEMS

The potential of detecting non-metallic targets makes the GPR complementary to a metal detector in the application of AP landmine detection. The additional information on location and other target features could significantly reduce the false alarms, as well as speed up the clearance process of mine fields. In spite of this promising potential, the use of GPR in real demining operations for the moment is negligible. This is mainly due to four reasons or drawbacks:

1. The first drawback is the limited range resolution. The range resolution of a radar system is defined as "the ability to distinguish between two targets solely by the measurement of their ranges (distance from the radar); usually expressed in terms of the minimum distance by which two targets of equal strength at the same azimuth and elevation angles must be spaced to be separately distinguishable" (IEEE Std 686-1990 [6]). The range resolution ΔR (in this case depth resolution) of a GPR is just like in any other radar system directly related to the bandwidth of the system (B) and the propagation velocity v by

$$\Delta R = \frac{v}{2B} \quad (2.1)$$

In most of the conventional GPR systems, the bandwidth is smaller than 2 GHz. Using the quantitative definition (1) the depth resolution is limited, depending on the permittivity of the ground, to 4.7 cm for dry soil ($\epsilon_r = 2.55$) and to 1.7 cm for very wet soil ($\epsilon_r = 20$) for said bandwidth of 2 GHz. As anti personnel land-mines are often laid shallow, conventional GPR can have air-ground interface is smooth and flat, simple image processing techniques can enhance the depth resolution. However, post-conflict areas often have a rough ground surface and are covered with a lot of vegetation. In this case, the performance of these simple image-processing techniques will be insufficient and

2. ULTRA-WIDEBAND TECHNIQUE FOR DEMINING SCANNING SYSTEMS

more depth, which means bandwidth, is needed. The choice of the lower and the upper cut-off frequencies of the frequency band is not straightforward. Using ultra-wideband involves the use of higher frequencies, which are strongly attenuated by lossy soil. Low frequencies ($<1\text{GHz}$) on the other hand have a good penetration in the ground, but a poor resolution. So when mines are buried too deep and the frequency band is chosen too high, it is possible that we do not detect anything at all because of the dramatically increased attenuation of the soil with frequency (at a frequency of 9.6 GHz , typically 5.9 dB/m for dry sand (0.3 vol\%) [7]).

2. A second problem with the GPR systems is the ability of discriminating between a mine and a mine-like target. This problem, similar to point 1, is related to the frequencies used by the GPR system. The wavelengths radiated by the GPR have the same order of magnitude as the size of the land-mines. As a consequence, the backscattering on the mine is very complex and the backscattered signal is a combination of different backscattering mechanisms. Many authors suggest that there is a lot of information in the late-time response (resonant part) of buried objects to short EM impulses. Regarding the GPR system as a linear response system, the larger the bandwidth at the input of the system, the more information one can get on the system. This additional information can be very useful for clutter reduction and/or classification of targets. So again a UWB approach imposes itself.
3. The third drawback concerns the antennas used in commercially available GPR systems. Antennas are a critical part in a GPR system. Most of the GPR systems are designed for applications other than demining and the antennas do not meet the specific requirements needed for this application. The most apparent example is the element antenna. Element antennas, like dipoles, are widely used in GPR systems. Unfortunately they have a low directivity and therefore perform best when they are in contact with

2. ULTRA-WIDEBAND TECHNIQUE FOR DEMINING SCANNING SYSTEMS

the ground, to couple as much energy as possible into the ground. For safety reasons, deminers do not want to use a sensor that is in direct contact with the ground. Further, minefields have often a very rough surface and are covered with a lot of vegetation. So the mobility and hence the dimensions and weight of the antenna become an issue. In the demining application, antennas that can be used off-ground are needed.

4. The last drawback is a more practical one. The output of a GPR is usually an image representing a vertical slice in the subsurface. These images are sometimes difficult to analyse and expert knowledge of the system and the physics behind the operating principle of the system is needed for correct interpretation of the results. In demining operations the deminers are usually not highly educated and they are anyway under too much stress to perform such a complex interpretation. This requires advanced discrimination techniques (e.g. HMM, SVD 3D maps) and simplified display of the subsurface image.

In this research we investigate the feasibility of possible solutions for all of these four drawbacks. The general aim is to provide advanced hard- and software for landmine detection. Present GPR technology is sufficient for fields like civil engineering or archeology, where it is relatively easy to detect anomalies several centimetres in the ground. Unfortunately, these technologies do not provide a good enough resolution and discrimination capabilities to find small objects buried in the air-ground interface.

Chapter 2 provides a brief history of GPR and a general description of conventional GPR. The different types of operational waveforms and their characteristics is described as well as an electromagnetic model that describes the earth environment that the wave must propagate through. An analysis contrasts the advantages, such as reflection from purely dielectric objects and disadvantages mainly due to those associated with penetration depth, range resolution and cost of using the UWB technique. The second part of the chapter presents some

2. ULTRA-WIDEBAND TECHNIQUE FOR DEMINING SCANNING SYSTEMS

initial experiments to characterise the dielectric constant and behaviour of sandy soil used in our laboratory based study and characterise the RCS for some commonly encountered landmine types.

2.2 The Radar Range Equation

The power received by a monostatic radar system (a system which uses the same antenna for both transmitting and receiving signals) when observing a point target can be estimated using the following equation [8],

$$P_r = P_t \frac{G^2 \lambda^2 \sigma}{(4\pi)^3 R^4 l} \quad (2.2)$$

Where P_r is the power received by the radar system (measured at the receiver input), P_t is the power transmitted (measured at the receiver output), G is the gain of the antenna, σ is the radar cross section of the target, R is the range to the target and l is a term to account for losses in the radar system itself.

The same equation can be slightly modified and used for a bistatic radar system (a system which uses different antennas for transmitting and receiving- these antennas may or may not be co-located) as follows.

$$P_r = P_t \frac{G_t G_r \lambda^2 \sigma}{(4\pi)^3 R_t^2 R_r^2 l} \quad (2.3)$$

Where G_t is the gain of the transmit antenna, G_r is the gain of the receive antenna, λ is the wavelength in use, σ is the radar cross section of the target, R_t is the range from the transmit antenna to the target and R_r is the range from the receive antenna to the target.

The maximum range that a target can be detected at can be estimated according to the following equation, which is a modification and rearrangement of the basic monostatic radar

2. ULTRA-WIDEBAND TECHNIQUE FOR DEMINING SCANNING SYSTEMS

equation previously given in equation 2.2.

$$R = \left[\frac{P_m T_c G^2 \lambda^2 \sigma}{(4\pi)^3 (SNR)_0 k T_0 F l} \right]^{\frac{1}{4}} \quad (2.4)$$

When P_m is the mean transmitted power, T_c is the coherent processing duration, $(SNR)_0$ is the signal to noise ratio the system requires to detect a target, k is Boltzmann's constant, T_0 is the operating temperature and F is the receiver noise figure.

This equation shows that there are several ways to improve the maximum detection range of a given radar system for a particular target. Increasing the transmitted power and/or the processing duration increases the detection range. Equivalently, decreasing the required signal to noise ratio, operating temperature or system losses will have the same effect.

2.2.1 GPR Range Equation

The standard radar equation (defined in eq. 2.3) needs to be modified to determine the penetration performance for GPR. The radar equation assumes a small point scattering target for the RCS term σ_T compared to the resolution cell size. For most GPR systems the point scatterer assumption is not suitable, because the resolution cell size is similar to the size of buried targets, in our case landmines. Therefore σ from equation 2.3 should be substituted with an RCS of a real target σ_T . Moreover, the antenna characteristics for GPR systems are divided in two separate terms, which are directional gain (G_{Tx} and G_{Rx}) and the coupling efficiency ζ_{Tx} for a wave from the air into the ground and ζ_{Rx} the coupling efficiency from the ground into the air. Another modification to the standard radar equation 2.2 is the substitution of the attenuation losses in the ground, $e^{4\alpha R}$ for the power loss factor l . Adding these factors to the standard radar equation gives us equation 2.5 where R denotes the distance in down range.

$$P_R = \frac{P_T G_{Tx} G_{Rx} \zeta_{Tx} \zeta_{Rx} \lambda^2 \sigma_T e^{4\alpha R}}{(4\pi)^3 R^4} \quad (2.5)$$

2. ULTRA-WIDEBAND TECHNIQUE FOR DEMINING SCANNING SYSTEMS

2.3 Radar Waveform Types

2.3.0.1 FMCW

Frequency Modulated Continuous Wave (FMCW) allows a wide bandwidth and a high mean power [9]. With a dwell time t_d , also called Ramp Repetition Interval (RPI), FMCW transmits a continuous wave (CW) in a triangular or sawtooth swept over a bandwidth B . The CW signal reflected from the target is multiplied with a reference signal, which is a replica of the transmitted signal, using a homodyne mixer. The difference in frequencies, or the beat frequencies f_b , are then allowed to move to an analogue-digital converter (ADC). The signal is then FFT'ed and the resulting signal is a time profile of the measured targets with respect to their travel times. The beat frequency is related to the travel time t_t by,

$$f_b = \frac{Bt_t}{t_d} \quad (2.6)$$

2.3.0.2 Pulse Compression GPR

An example for pulse compression GPR are impulse waveforms which transmitted through a log-periodic or logarithmic spiral antenna and expanded its time to resemble a chirp waveform [10]. At the receiver, the waveforms can be compressed in time using analogue or digital matched filtering. The advantage of this method is the extremely broad fractional bandwidth (decade) of the spiral antennas, which allows very high resolving capability. These antennas also possess a circular polarisation with the ability to detect long, thin objects (such as pipes and cables) independent of orientation. Phase shift keying (PSK) pulse compression methods have been used to determine the ice thickness of glaciers. This technique involves the transmission of a carrier frequency which is phase modulated with coded sequences. A synchronous receiver determines the I and Q baseband signals from reflected waveforms in an almost identical fashion. A matched filter correlates the I and Q signals with delayed versions of the transmitted signal to produce a time profile of targets. Yet another type of

2. ULTRA-WIDEBAND TECHNIQUE FOR DEMINING SCANNING SYSTEMS

pulse compression used for GPR has been noise modulation. In this system, ultra-wideband noise is transmitted and a matched receiver is used as a correlator to produce a time profile of targets.

2.3.0.3 SFCW

The stepped-frequency continuous wave radar transmits a waveform comprising of single frequency tones stepped in Δf Hertz frequency intervals across a bandwidth B [11]. Continuous wave (CW) radars continuously broadcast radar waveforms, which may be considered to be pure sine waves. Radar echoes arise from stationary targets and return back to the broadcasting unit, where they are detected by the receiving antenna. The phase of the returning echoes may be used for range determination, although in practice, a series of stepped frequencies must be employed to obtain reasonable maximum distances.

2.4 UWB Waveform Capability

2.4.1 Penetration Depth

EM waves are coupled into the ground and the backscattered waves are sampled. An EM wave is backscattered by any electrical parameter contrast in the ground, such as the permittivity ϵ , the permeability μ or the conductivity σ . In practice mostly a contrast in permittivity leads to a reflection of the EM waves coupled into the ground. Ground materials that are non-magnetic have a relative permeability of $\mu_r = \mu/\mu_0$ of 1, with $\mu_0 = 4\pi 10^{-7} H/m$ being the permeability of free space. In this case no contrast in permeability will be recognised. A change in conductivity primarily affects the absorption of EM waves in the medium. Therefore, the variation in permittivity between materials has the biggest impact on the impedance of mediums, thus contrasts in permittivity ϵ of materials results in reflections.

The Helmholtz wave equation can be derived from Maxwell's equation for plane waves propagating through a general lossy medium. A solution to the Helmholtz wave equation is

2. ULTRA-WIDEBAND TECHNIQUE FOR DEMINING SCANNING SYSTEMS

the electric field $E(z)$, described by equation (2.7), of the plane wave propagating in the z direction.

$$E(z) = E_0 e^{-\gamma z} = E_0 e^{-\alpha z} e^{-j\beta z} \quad (2.7)$$

E_0 is an electric field constant, e is the base exponential and γ is the propagation constant, which is made up of a real and an imaginary component: attenuation constant α (equation 2.8) and phase constant β (equation 2.9). The propagation constant of each model material layer can be defined as $(\gamma = \alpha + j\beta)$, where α is the attenuation constant, β is the phase constant, and δ is the skin depth constant which can be defined by equations 2.8-2.10, respectively:

$$\alpha = \omega \left[\frac{\mu\epsilon}{2} \sqrt{1 + \tan^2 \delta} - 1 \right]^{\frac{1}{2}} \quad (NP/m) \quad (2.8)$$

$$\beta = \omega \left[\frac{\mu\epsilon}{2} \sqrt{1 + \tan^2 \delta} + 1 \right]^{\frac{1}{2}} \quad (rad/m) \quad (2.9)$$

$$\delta = \frac{1}{\alpha} = \frac{1}{\omega \left[\frac{\mu\epsilon}{2} \sqrt{1 + \tan^2 \delta} + 1 \right]^{\frac{1}{2}}} (m) \quad (2.10)$$

For those equations, ω is the radian frequency ($\omega = 2\pi f$, where f is the electromagnetic frequency), μ is the magnetic permeability and ϵ the electric permittivity of the medium. The $\tan \delta$ term is the loss tangent defined in equation (2.11)

$$\tan \delta = \frac{\epsilon''}{\epsilon'} = \frac{\sigma}{\omega\epsilon} \quad (2.11)$$

Here, ϵ' is the real component and ϵ'' is the imaginary component of the permittivity ϵ and σ is the conductivity of the medium. The attenuation constant α of equation (2.8) has the dimensions of Nepers per metre. Attenuation of the ground material is usually expressed in

2. ULTRA-WIDEBAND TECHNIQUE FOR DEMINING SCANNING SYSTEMS

decibels per metre (dB/m). The conversion of α from Np/m to dB/m is obtained by equation (2.12).

$$\alpha[dB/m] = 20 \log_{10} e^{\alpha} = 20\alpha \log_{10} e = 8.686\alpha[Np/m] \quad (2.12)$$

The phase constant β (radians per metre) can be converted to phase velocity v using equation (2.13)

$$v = \lambda f = \frac{\omega}{\beta} \left[\frac{\mu\epsilon}{2} \sqrt{1 + \tan^2 \delta} + 1 \right]^{-\frac{1}{2}} \quad (2.13)$$

2.4.1.1 Constant Q Model

The quality factor Q is a well established measurement of the ratio of 2π times the energy stored to the energy radiated and dissipated in one cycle. The quality factor is related to the attenuation constant α and the propagation velocity v as seen in equation 2.14, where λ is the wavelength in the ground and ω is the angular frequency.

$$Q = \frac{\omega}{2v\alpha} = \frac{\pi}{\lambda\alpha} \quad (2.14)$$

The quality factor for ground materials is relatively constant over a wide range of wavelength according to (Stacey et al). This suggests that the attenuation α is linear with the wavelength λ . The attenuation constant α is also linear with frequency f for a constant propagation velocity v .

Siggins and Turber, 1992 proposed a similar constant Q propagation model for describing radar propagation in the ground. For the low loss media (where $\tan^2 \delta \ll 1$), the attenuation constant α is approximately equal to $\frac{1}{2}\omega\sqrt{\mu\epsilon} \tan \delta$ and then substituted into the Q definition of equation 2.14 forms equation 2.15

$$Q = \frac{2\omega}{2v\omega\sqrt{\mu\epsilon} \tan \delta} = \frac{2\omega v}{2v\omega \tan \delta} = \frac{1}{\tan \delta} \quad (2.15)$$

2. ULTRA-WIDEBAND TECHNIQUE FOR DEMINING SCANNING SYSTEMS

For this reason, commercial GPR companies and researchers try to use a lower centre frequency ≤ 1 GHz for the systems in which the penetration depth is the key parameter. On the other hand, by lowering the centre frequency, the pulse bandwidth will be reduced and consequently the resolution will also be decreased. The resolution is a vital non-negotiable system requirement in humanitarian demining equipment.

2.4.2 Range Resolution

2.4.2.1 Unambiguous Range

The bandwidth to compute the range resolution is created by stepping across a series of discrete frequencies in a linear chirp. These frequencies are separated by a fixed frequency Δf , in accordance to the number of steps. These frequency steps result in a so called unambiguous range, which is given by,

$$R_{unambig} = \frac{c}{2\Delta f} \quad (2.16)$$

With $R_{unambig}$ being the unambiguous range, c the speed of light in a vacuum and Δf the frequency step. The fractional bandwidth B/f_c of a simple pulsed waveform can be expressed as $1/rf_c$, with f_c be in the centre frequency, of the $1/B$ envelope width of the pulse.

2.4.2.2 Down Range Resolution

One important characteristic of the radar is spatial resolution, defined as "the ability to distinguish between two targets solely by measurement of their ranges (distances from the radar: usually expressed in terms of the minimum distance by which two targets of equal strength at the same azimuth and elevation angles must be spaces to be separately distinguishable)".

The quantitative definition of resolution for radar signals has been adapted from *Rayleigh's criterion* for optical resolution. For the radar case, this criterion states that "two point targets whose reflected signals are of equal amplitude are resolved when the peak response from one

2. ULTRA-WIDEBAND TECHNIQUE FOR DEMINING SCANNING SYSTEMS

target falls on the first minimum of the second target” [12]. Figure 2.2 shows two sinc signals of equal amplitude, whose resolution in time is defined when the peak of the first pulse response is directly over the first minimum of the second pulse response. This is the case when both pulses cross at their $-4dB$ points where both peaks are separated by $1/B$ second [10].

However, GPR Radar engineers have adapted this definition with less stringent resolution criterion. As mentioned above, Noon [10] uses a resolution criterion of one range bin in his work:

$$bin = \frac{1}{B} \quad (2.17)$$

where the pulses cross at their $-4dB$ points and both pulses are separated by $1/B$, as shown in Figure 2.2. For Harris [13] (*Harris-Window*) two peaks have to cross at their $-6dB$ points which means both pulses are separated by 1.21 range bins:

$$BW_{6dB} = 1.21 * \frac{1}{B} \quad (2.18)$$

Further common pulse separation criteria are displayed in Table 2.1 [14]:

Table 2.1: Separation of two pulses by their bandwidth and range bins accordingly.

separated by bandwidth	relative width of bins
3dB	0.89
4dB	1
6dB	1.21
7dB	1.28

The pulse width is the key factor in the range resolution. A radar system, with all other elements at maximum efficiency, should be able to distinguish targets separated by one-half of the pulse width time; hence, the theoretical range resolution of a radar system can be defined as,

$$\Delta R = R_{n-1} - R_n = \frac{c\tau}{2\sqrt{\epsilon_r}} \quad (2.19)$$

2. ULTRA-WIDEBAND TECHNIQUE FOR DEMINING SCANNING SYSTEMS

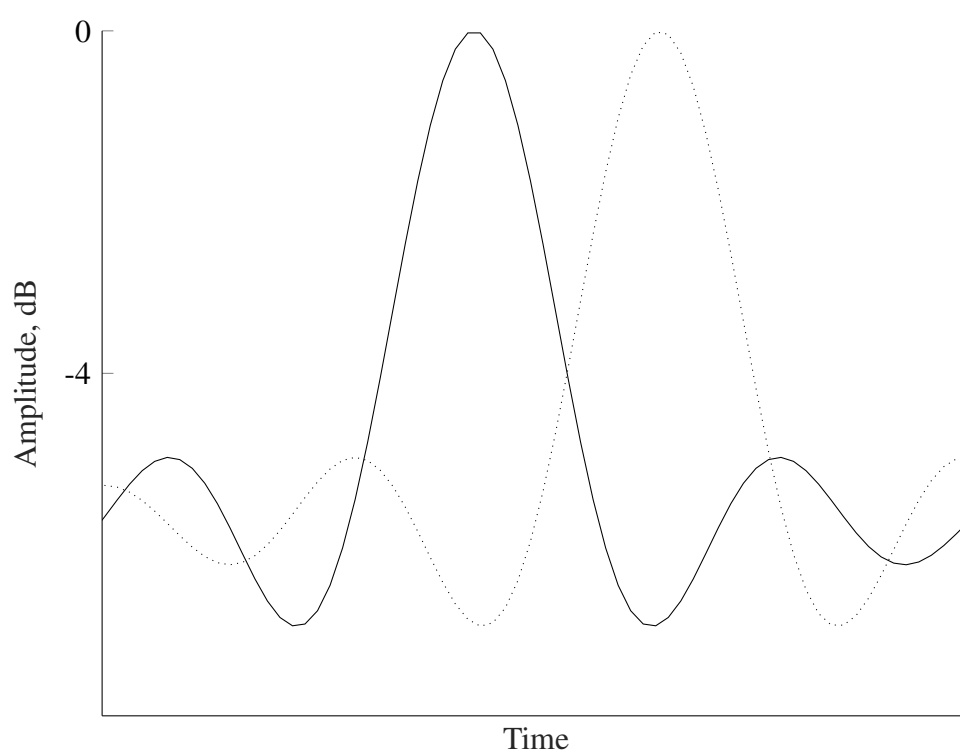


Figure 2.2: Noon criterion: limit of resolution for two point scatterers [10]

2. ULTRA-WIDEBAND TECHNIQUE FOR DEMINING SCANNING SYSTEMS

where c represents speed of light in free space, $\tau(s)$ is the pulse width in second and ΔR (m) is the distance between two targets in meter. This means by reducing the pulse width and hence increasing the pulse bandwidth, smallest target can be resolved by the system due to eliminating the problem of overlapping of the reflected pulses. In the case that is a limitation for decreasing the pulse width due to the sampling and down conversion issues that are introduced for the system design, a pulse compression technique can be employed to increase the pulse bandwidth. The range resolution of the radar is given by the bandwidth of the transmitted pulse B , instead of its pulse width. This allows very high resolution to be obtained with long pulses, thus resulting in a higher average power.

$$\Delta R = \frac{c}{2B\sqrt{\epsilon_r}} \rightarrow B \geq \frac{c}{2\Delta R\sqrt{\epsilon_r}} \quad (2.20)$$

Since in this work we want to detect landmines, it is necessary to choose our system bandwidth according to the dimensions of a generic landmine. The landmines used in this work have a thickness between 15 and 50 mm. Thus the required bandwidth for any landmine type with a different thickness can be calculated and the results are presented in Table 2.2. This indicates that for detection of a 2 mm dielectric layer, such as a landmine ($\epsilon_r=2.55$) in free space, there is a need of a pulse with a bandwidth of higher than 47 GHz, which is not achievable using the UWB pulses. However, given Equation 2.20, the bandwidth needed for detection can be reduced to 26.9 GHz if said dielectric layer is introduced to another medium, such as lossy sand with 4% moisture level ($\epsilon_r=8$). This means, for the detection of a landmine buried in moist sand, with an average thickness of 15 mm, a bandwidth of 3.53 GHz is needed. Accordingly, for a landmine buried in moist sand, with an average thickness of 50 mm, a bandwidth of 1.06 GHz is needed. As a result, size and weight of the system detecting objects in the subsurface are significantly lower than for a system designed for free space.

There are other processing techniques that are being developed and further used in the

2. ULTRA-WIDEBAND TECHNIQUE FOR DEMINING SCANNING SYSTEMS

Table 2.2: Landmine thickness and its required bandwidth for appropriate range resolution

Landmine thickness (mm)	Bandwidth $B \geq \frac{c}{2\Delta R\sqrt{\epsilon_r}}$ (GHz) free-space	Bandwidth $B \geq \frac{c}{2\Delta R\sqrt{\epsilon_r}}$ (GHz) sand (4%)
2	46.9	26.9
10	15	5.31
15	10	3.53
20	7.5	2.65
35	4.28	1.51
50	2.9	1.06
75	2.0	0.707

previous researches, to reduce the cost of the overall system which has its own limitations, according to the following:

2.4.3 Processing Technique

2.4.3.1 Cross Range Resolution

The cross range resolution of a real antenna radar system is governed by the physical size of the antenna in the cross range direction and the distance to the target under observation. Fundamentally, the beamwidth β produced by a real aperture antenna is given by:

$$\beta = \frac{\lambda}{D_{real}} \quad (2.21)$$

Where λ is the wavelength being transmitted and D_{real} is the physical dimension of the antenna aperture in the cross range dimension. From this, simple geometry shows that the resolution from the beam is dependent on the range of the target. As the beamwidth changed linearly with distance, this results in a cross range resolution of a real aperture radar system being given by:

$$Res_{CR} = \frac{\lambda R}{D_{real}} \quad (2.22)$$

2. ULTRA-WIDEBAND TECHNIQUE FOR DEMINING SCANNING SYSTEMS

As seen in equation 2.22 clearly shows that the larger an antenna is the better the cross range resolution at a given distance will be. Unfortunately, as the range to the target increases the antenna size required to maintain a given resolution also increases.

Similarly, the cross range resolution degrades (becomes larger) as the radar wavelength increases. This means that as the frequency decreases, the cross range resolution will degrade. For sub-surface radar imaging, this is a particular concern as lower frequencies offer better penetration into soil and are therefore preferred.

The SAR technique takes advantage of the movement of a radar platform to synthesise a much larger antenna aperture than that given by the physical antenna. As the platform moves a given scatterer in the target scene is illuminated by the real antenna's main beam for a period of time, during which the scatterer is hit by a number of pulses which each produce an echo, which are recorded by the radar system in complex form (amplitude and phase). By processing the recorded echoes according to their phase shift it is possible to synthesise an antenna which is as long as the distance which the platform moves whilst the scatterer is still in the main beam of the real antenna.

The movement and operation of the radar platform can be thought of as a series of individual elements. For the simplest mode of SAR operation, summing the returns from each of the individual antenna elements generates the synthetic aperture. This is directly equivalent to the summing performed by the electrical interconnections in a physical array antenna. This unfocused operation does not take into account the phase differences present in the returns from a single target over multiple elements. Due to sequential sampling of each individual element in the synthetic array the cross range resolution of a SAR system is improved over a real aperture system. In the SAR case, the cross range resolution is given by

$$X_{res} = \frac{\lambda R}{2L_{Eff}} \quad (2.23)$$

where L_{Eff} is the effective aperture of the SAR, and the factor of 2 in the denominator

2. ULTRA-WIDEBAND TECHNIQUE FOR DEMINING SCANNING SYSTEMS

represents the cross range resolution improvement due to sequential sampling.

From this, it may seem that the cross range resolution can be infinitely improved by increased L_{Eff} . However, ignoring focussing issues and assuming a non-steerable antenna the factor that limits L_{Eff} (and hence the maximum cross range resolution) is the beamwidth of the SAR system's real antenna. This limitation arises due to the necessity to keep a target in the view of all elements of the synthetic array. This limitation is expressed by,

$$L_{Max} = \frac{\Delta R}{D_{real}} \quad (2.24)$$

Where L_{Max} is the maximum possible length of the synthetic aperture. This can be determined by multiplying the beamwidth by the range (beamwidth at range R).

From this we can derive the maximum resolution

$$X_{MaxRes} = \frac{\Delta R}{2L_{Max}} = \frac{\Delta R D_{real}}{2\Delta R} = \frac{D_{real}}{2} \quad (2.25)$$

This shows that the cross range resolution of a SAR system is directly proportional to the length of the real antenna, where a smaller antenna gives a better resolution, and is not dependent on range to the target.

2.5 Preliminary Characterisation of Soil and Targets

2.5.1 Experimental Setup

Experiments have been conducted on the indoors soil facility which consists of one soil bay (2.4Lx1.2Wx0.8H meters) filled with sand; and one bay (1.2Lx1.2Wx0.8H meters) filled with RAM for placing calibration targets, such as a 40 mm sphere for co-polar calibration and a brass rod, placed in an 22.5° angle perpendicular to the direction of antenna movement, for cross-polar calibration. The soil is maintained within a 1-3% moisture content and at a constant temperature of $25^\circ C$. A Near-Field Measurement System (NFMS) has been erected over the two bays with a 3 m long linear automated positioner. The antenna array acquires the

2. ULTRA-WIDEBAND TECHNIQUE FOR DEMINING SCANNING SYSTEMS

scattering parameter S_{21} across the 0.4-4.8 GHz frequency spectrum and takes measurements at 1 cm intervals along the horizontal x-axis. Figure 2.3 shows the dual polarised near-field antenna configuration. The setup uses a linear polarised TEM (Scientific Atlanta) horn that illuminates the ground scene in vertical (V) polarisation. The local back-scattered electromagnetic field is collected by two loop antennas arranged orthogonally and in front of the TEM antenna to acquire VV and VH (vertical-horizontal) co- and cross-polarised data. The loop antennas are 40 cm above the soil surface. The antenna height is typical of a stand-off GPR. This height is a trade-off between such factors as the energy attenuation, decreasing the antenna-soil coupling, avoiding possible obstacles of the ground surface, and forming sufficient antenna footprint for future SAR processing. To make orthogonal polarization measurements, i.e. HH and HV, the antenna array is rotated clockwise by 90° and data taken.

2. ULTRA-WIDEBAND TECHNIQUE FOR DEMINING SCANNING SYSTEMS

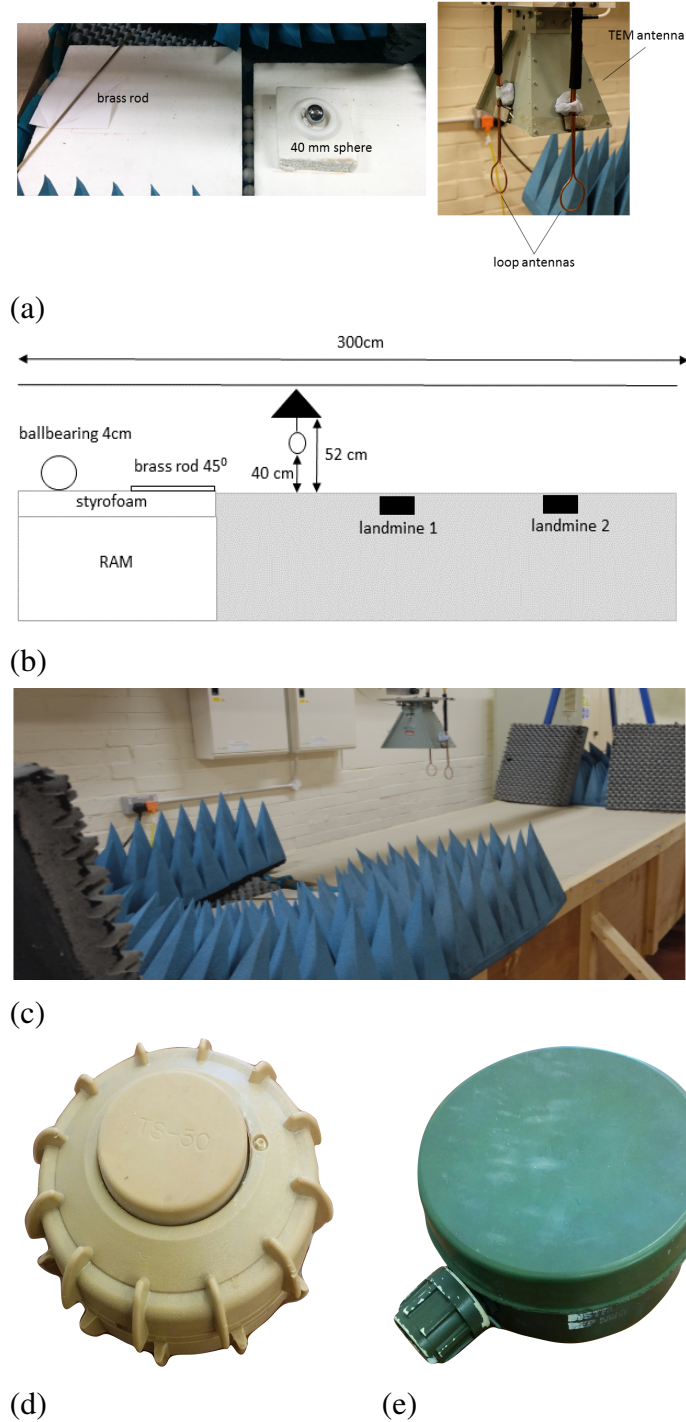


Figure 2.3: (a) Calibration targets and antenna head, (b) Sketch of measurement setup, (c) Laboratory scene (d) Landmine 1 is an Italian TS-50 landmine, (e) Landmine 2 is a Russian PMN-1 landmine.

2. ULTRA-WIDEBAND TECHNIQUE FOR DEMINING SCANNING SYSTEMS

2.5.2 Permittivity Measurements

To determine the permittivity and permeability of the material we use to bury our targets in, namely sand, gravel and loam, some preliminary experiments were conducted. The complex permittivity and permeability were determined by using the transmission reflection method. To process the data, the Nicolson-Ross-Weir (NRW) transmission reflection line theory was used.

2.5.2.1 The Transmission Reflection Method

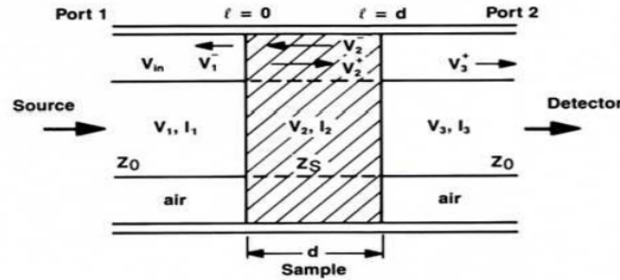


Figure 2.4: Section of coaxial airline filled with an annular bead of sample material (taken from [15])

Since we are using the Nicolson-Ross-Weir method the basic theory according to [15][16] is shortly reviewed. The complex permittivity and permeability can be determined from the transmission and reflection scattering parameters. Figure 2.4 shows a sketch of a 50 Ω coaxial guide filled with a material sample and where the symbols have their usual meaning. The NRW method has the advantage that it is non-iterative and applicable to a coaxial line section. The following equations relate to parameters S_{11} , the radiation emission of port 1 to that collected at port 1 and S_{21} the scattering parameter related to radiation emission from port 1, collected at port 2. Figure 2.4 depicts the relationship of Γ and T coefficients to port voltage and currents which can be related to two-port scattering parameters as,

$$A = S_{11} + S_{21} \quad (2.26)$$

2. ULTRA-WIDEBAND TECHNIQUE FOR DEMINING SCANNING SYSTEMS

$$B = S_{11} - S_{21} \quad (2.27)$$

which leads to,

$$k = \frac{1 - AB}{A - B} \quad (2.28)$$

$$\Gamma = k \pm \sqrt{k^2 - 1} \quad (2.29)$$

$$T = \frac{A - \Gamma}{1 - A\Gamma} \quad (2.30)$$

According to [16] the auxiliary variables x and y are derived from the transmission and reflection coefficients,

$$x = \frac{\mu_r}{\epsilon_r} = \left(\frac{1 + \Gamma}{1 - \Gamma} \right)^2 \quad (2.31)$$

$$y = \mu_r \epsilon_r = \left[\frac{j \ln(T)}{2\pi d} \right] \quad (2.32)$$

From that the the complex permittivity and permeability are given as,

$$\mu_r = \sqrt{xy} \quad (2.33)$$

$$\epsilon_r = \sqrt{y/x} \quad (2.34)$$

2.5.2.2 Soil Sample Preparation

Before the aforementioned soil samples could be measured they were processed in the following way. Each sample was first dried at 100 °C for six hours and then ground in a mortar. After that the samples were filtered through a 100 μm sieve. The samples of the grounded soils were then surveyed microscopically with an electron microscope. The results are shown in Figure 2.5. It can be seen that most of the sand particles are around 60 μm , while the soil (most $\leq 40\mu\text{m}$) and the gravel (most $\leq 60 \mu\text{m}$) samples seem to be much finer.

2. ULTRA-WIDEBAND TECHNIQUE FOR DEMINING SCANNING SYSTEMS

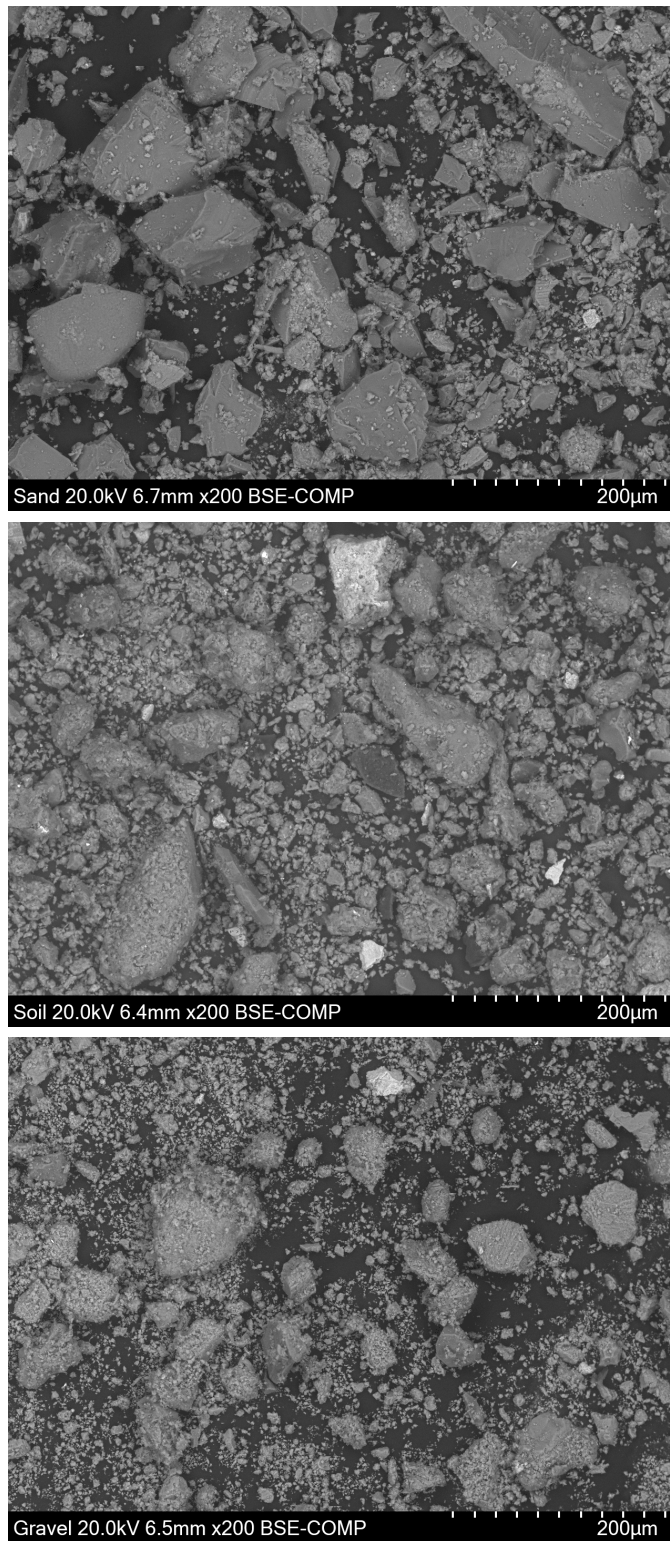


Figure 2.5: Eletron microscope images of ground sand, soil (loam) and gravel samples.

2. ULTRA-WIDEBAND TECHNIQUE FOR DEMINING SCANNING SYSTEMS

The permittivity measurement setup can be seen in Figure 2.6 and Figure 2.7 shows the sample holder filled with sand.



Figure 2.6: Photograph of coaxial waveguide system setup with ground samples in flasks.

A full TRL (transmission-reflection-load) two-port calibration was performed using the open, short and TEM cell test fixture on a HP8719C vector network analyser over the 50 MHz- 13.51 GHz range. The calibration establishes the coaxial impedance in air and reference planes for the measurement test ports. The complex permittivity for the different samples were extracted by the NRW technique using equation 2.26 to 2.34 to extract the relative complex permittivity. The results are given in Table 2.3. The data indicates that the nominal relative permittivity for dry sand is 2.61 ± 0.1 over the frequency range while the relative permittivity of sand with 10% moisture level is raised, particularly at lower frequencies, and monotonically decreases with increasing frequencies and this was anticipated. The 10% moisture level for this experiment was chosen, because it constitutes the percolation limit for most soils. This means at this moisture level the soil can not absorb any further moisture and a repeatability of experiments can not be guaranteed. In the further chapters the moisture level for our experiments will be held to 1-3% as this reflects a moisture level one would

2. ULTRA-WIDEBAND TECHNIQUE FOR DEMINING SCANNING SYSTEMS

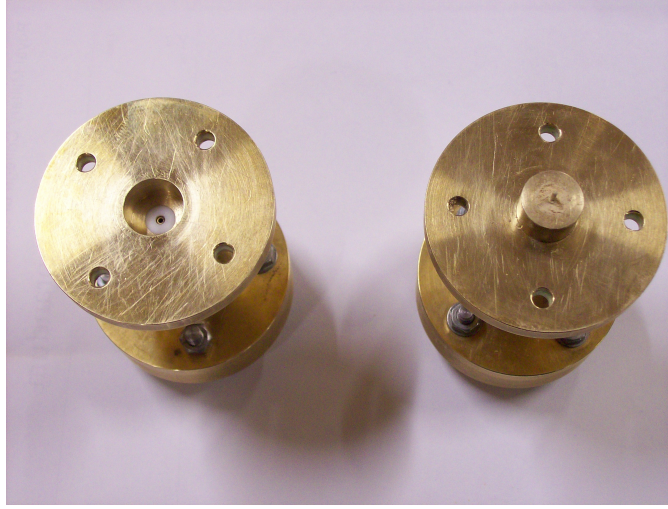


Figure 2.7: Photograph of coaxial waveguide system with sample holder filled with sand.

encounter in a desert area between the early morning hours and noon. Here dew in the early morning hours causes a slightly higher moisture level in the surface area (3%) than around noon (1%).

2.5.3 Monostatic RCS of APMs

One factor that influences the system design is the Radar Cross Section (RCS) of the target. The RCS is a measure of the amount of energy reflected back to the radar antenna by an object versus the amount of energy incident on that object due to the radar. The RCS is measured in m^2 and the RCS for a particular target is physical size of a smooth ball bearing that would give the same return as the target of interest.

The RCS (σ) of a smooth sphere is given by:

$$\sigma = \pi r^2 \quad (2.35)$$

As long as

$$\lambda \ll r \quad (2.36)$$

2. ULTRA-WIDEBAND TECHNIQUE FOR DEMINING SCANNING SYSTEMS

Table 2.3: Measured dielectric properties of sand samples dry and at 10% moisture level.

Soil Type	Freq (GHz)	ϵ_r'	$\pm\epsilon_r'$	ϵ_r''	$\pm\epsilon_r''$	μ_r
sand (dry)	0.4	2.02	0.1	0.11	0.1	1.0
sand (10%)	0.4	4.80	0.1	1.10	0.1	1.0
sand (dry)	2.6	2.80	0.1	0.2	0.1	1.0
sand (10%)	2.6	3.24	0.1	0.81	0.1	1.0
sand (dry)	4.8	2.61	0.1	0.4	0.1	1.0
sand (10%)	4.8	3.35	0.1	0.51	0.1	1.0
sand (dry)	8.2	2.75	0.1	0.20	0.1	1.0
sand (10%)	8.2	2.7	0.1	-0.23	0.1	1.0
sand (dry)	10	3.08	0.1	0.21	0.1	1.0
sand (10%)	10	2.26	0.1	-0.30	0.1	1.0
sand (dry)	12.4	2.45	0.1	-0.22	0.1	1.0
sand (10%)	12.4	2.10	0.1	-0.20	0.1	1.0

and

$$\lambda \ll R \quad (2.37)$$

Where λ is the wavelength of the incident wave, r the radius of the sphere and R the distance to the sphere. Note that the sphere is spatially uniform and has neither a dependency on the orientation relative to the antenna nor the frequency. Next this issue will be examined further by composing the GPR performance for a well-known object (sphere) and comparing this with the measured values. These results are the basis for a quantitative comparison with the RCS-es of the land-mines and clutter objects.

First the RCS of the objects in free space are measured. Free space is imitated by covering the sandbox and putting RAM on the cover. An empty paper cup serves as support for the ball bearing (2.8). The land-mines are placed on the RAM directly. The antenna is mounted 30 cm and 15 cm respectively above the RAM plateau.

For computing the RCS of a ball bearing of 3 mm, over a bandwidth from 0.4 - 4.8 GHz, Knott's efficient Bessel function algorithm was used[17]. The calculated average RCS of the

2. ULTRA-WIDEBAND TECHNIQUE FOR DEMINING SCANNING SYSTEMS

ball bearing is -28,86 dB. From the gathered S-parameter data the average magnitude was computed and converted to dB. The resulting RCS in VV is -44.44 dB and -51.06 dB in VH. This leaves us with a correction value in VV of: $(44.44 - 28.86)dB = +15.58dB$ and $+22.2dB$ for VH respectively.

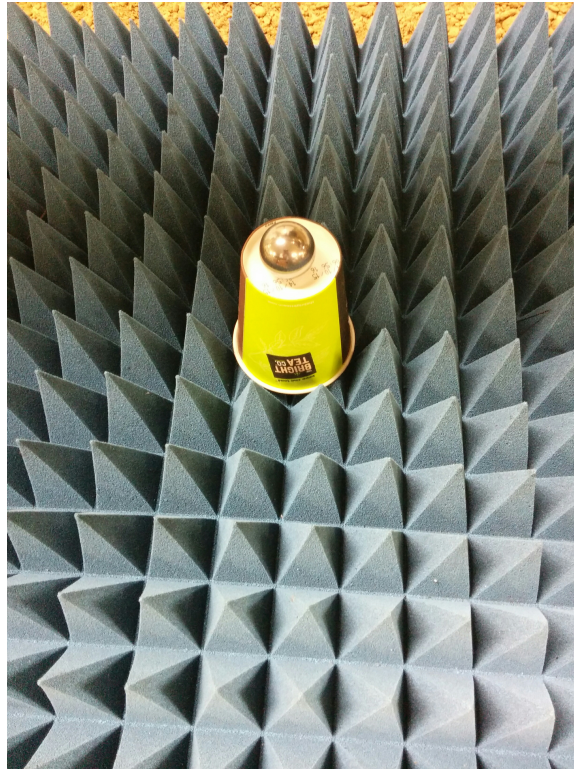


Figure 2.8: Ball bearing (30 mm) on cup used for system calibration measurement.

The calculated RCS-es for the metal sphere were correct. This means the radar range equation for GPR can be applied in free space. Based on that fact we can make an estimation of the RCS of the other objects in this specific configuration, and more importantly direct comparison of the mono-static RCS of a landmine. Given the backscattered power of the land-mines in both polarization it is possible to distinguish each object from one another.

2. ULTRA-WIDEBAND TECHNIQUE FOR DEMINING SCANNING SYSTEMS

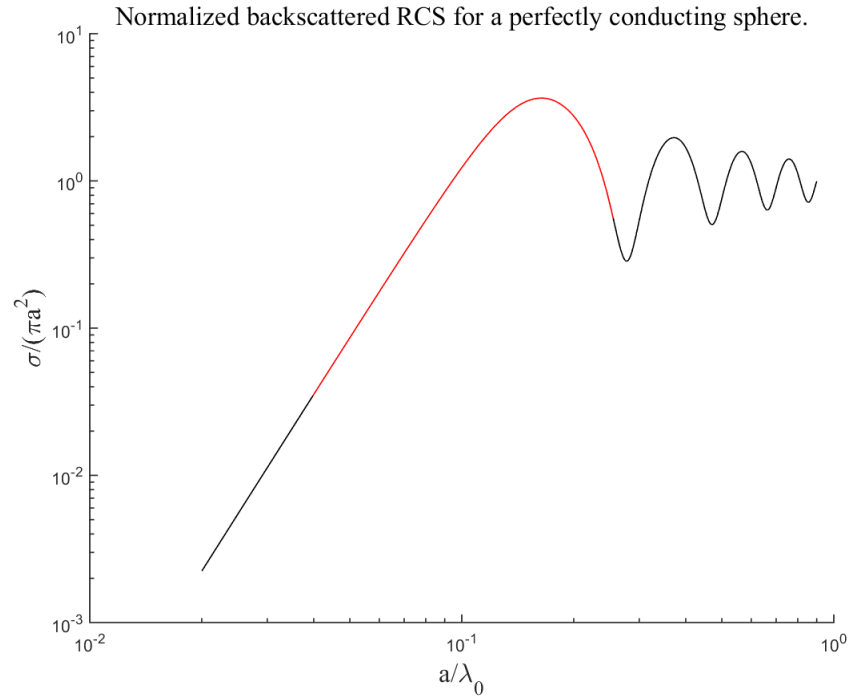


Figure 2.9: Ball bearing (30 mm) on cup used for system calibration measurement.

Table 2.4: Near-field RCS(dB) measured in VV

Object	Average RCS	Peak RCS
Ball bearing (30 mm)	- 28.86*	- 25.85*
L10 Ranger	- 22.76	-16.63
Valmara 59	- 19.86	-13.02
TS - 50	- 30.10	-18.80
PFM-1 (Butterfly)	- 26.04	-19.21
PNM-1	- 22.21	-16.60
Schuhbox (IED)	- 25.73	-19.78
Coca-Cola can	- 21.25	-15.81
Cigarette package	- 25.63	-19.07
Shell case (5.56 × 45 mm)	- 20.50	-15.39

2.6 Summary Comments

This chapter has given a more indepth review of the research issues and challenges both scientific and technical to be tackled in the this thesis. The basic principles of ground penetrating

2. ULTRA-WIDEBAND TECHNIQUE FOR DEMINING SCANNING SYSTEMS

radar have been reviewed with respect to waveform type and resolution. A relatively simple electromagnetic soil modelling was presented and used to analyse signal depth of penetration and resolution. Practical feasibility of deployment and cost were also important system considerations. The results suggest that an UWB bandwidth of 4GHz can provide satisfactory resolution in a range of soil environments to detect small (typically ≤ 1.5 cm) non-metallic objects. However, without aprior knowledge the optimum UWB transmit spectrum may not be known. As UWB GPR transceiver technology that sweeps and processes perhaps up to 20 GHz of bandwidth is both impractical and unnecessary. This thesis proposes a dual UWB waveform of 4.4 GHz bandwidth and centred around 2.6 GHz (0.4-4.8 GHz) and 4.2 GHz centred at 10.3 GHz (8.2-12.4 GHz). This dual band approach provides a range of advantages in terms of low band depth of penetration into very lossy soils and high band resolution. It also admits the possibility of collecting dual and full polarisation data on the subsurface and this promising will be investigated in later chapters. Some preliminary experiment work was conducted to characterise the electrical properties of the soils used in the course of our laboratory experiments and some free space measurements of landmine RCS. The results demonstrate that the dry sandy soil had a relative dielectric permittivity of around 2.8 at a frequency of 2.6 GHz and 3.08 at a frequency of 10 GHz while sandy soil at a moisture level of 10% had a relative dielectric permittivity of 3.24 at a frequency of 2.6 GHz and 2.26 at a frequency of 10 GHz. While the study was helpful in establishing a benchmark permittivity, it can only be considered idealistic and a more rigorous electromagnetic model of soil must include soil texture, humidity, temperature and atmospheric pressure. The RCS measurements of the landmines confirmed the low levels of reflectivity encountered and highlighted the limitation and difficulty of single polarisation GPR to identify landmine. As was mentioned, in order to increase the bandwidth and therefore resolution some drawbacks are built into the system, namely less penetration depth, more increase in hardware cost due to the dual band approach (increased sampling and processing hardware). However, this chapter has highlighted there

2. ULTRA-WIDEBAND TECHNIQUE FOR DEMINING SCANNING SYSTEMS

are a number of algorithms, principally synthetic aperture processing (SAP) in order to increase the range resolution without increasing the pulse bandwidth. SAP and other eigen decomposition techniques, exploiting polarisation, will be developed in later Chapters. A key enabling technology to exploit all of these technologies is the development of next generation GPR antennas and GPR polarimetry array technology. One outcome of this chapter is that with a bandwidth of 4 GHz the majority of buried landmines could be detected (given a thickness of common landmines between 15 and 50 mm). On the one hand, for a portable antenna system it is mandatory to keep the overall size to a minimum. On the other hand, the chosen centre frequency still needs to be able to penetrate the ground soil enough to detect buried landmines. As a trade-off between antenna size and depth penetration in the soil it was thought that the X-band (8.2 - 12.4 GHz) would be most suitable for that purpose. To keep the overall weight of the antenna system low, the possibility of 3D printing antennas from plastic and copper coating these will be addressed in the next chapter.

2. ULTRA-WIDEBAND TECHNIQUE FOR DEMINING SCANNING SYSTEMS

References

- [1] W. Stern, in *Versuch einer elektrodynamischen Dickenmessung von Gletschereis*. Gerl. Beitr. zur Geophysik, 23, 292–333, 1929.
- [2] R. Morey, in *Continuous subsurface profiling by impulse radar*. Proceedings of the Engineering Foundation Conference on Subsurface Exploration for Underground Excavation and Heavy Construction, pp. 213-232, 1974.
- [3] M. J. Hines, A. Piers, K. Du, B. Gonzalez-Valdes, J. . Martínez-Lorenzo, and C. M. Rapaport, “Localization of anti-personnel landmines using multi-bistatic ground-coupled ground penetrating radar,” in *2014 USNC-URSI Radio Science Meeting (Joint with AP-S Symposium)*, 2014, pp. 241–241.
- [4] E. Eide, T. Kießling, and J. Typpö, “Wideband antenna array for step-frequency ground penetrating radar,” in *2012 14th International Conference on Ground Penetrating Radar (GPR)*, 2012, pp. 152–155.
- [5] D. Daniels, *Ground Penetrating Radar - 2nd Edition*. IET, 2004.
- [6] “Ieee standard radar definitions,” *IEEE Std 686-1990*, pp. 1–32, 1990.
- [7] K. K. Williams and R. Greeley, “Radar attenuation by sand: laboratory measurements of radar transmission,” *IEEE Transactions on Geoscience and Remote Sensing*, vol. 39, no. 11, pp. 2521–2526, 2001.
- [8] M. B. C.E Cook, *Radar Signals*. Academic Press, 1967, chapter 1, p. 1.
- [9] M. Jankiraman. Artech House, 2018.
- [10] D. Noon, in *Stepped-Frequency Radar Design and Signal Processing Enhances Ground Penetrating Radar Performance*. The University of Queensland, 1996.

2. ULTRA-WIDEBAND TECHNIQUE FOR DEMINING SCANNING SYSTEMS

- [11] S. B. Thomas and L. P. Roy, “A comparative study on calibration technique for sfew ground penetrating radar,” in *2017 International conference on Microelectronic Devices, Circuits and Systems (ICMDCS)*, 2017, pp. 1–4.
- [12] D. Wehner, in *High-Resolution Radar*. Artech House, 1995.
- [13] F. J. Harris, “On the use of windows for harmonic analysis with the discrete fourier transform,” *Proceedings of the IEEE*, vol. 66, no. 1, pp. 51–83, 1978.
- [14] W. Herijgers, in *System Definition and Set-up of a Stepped Frequency Continuous Wave Ground Penetrating Radar*. TU Delft, 1999.
- [15] W. B. Weir, in *Automatic Measurement of Complex Dielectric Constant and Permeability at Microwave Frequencies*. Proceedings of IEEE, vol. 61, No. 1, January 1974.
- [16] D. L. Mensa, in *Material Measurement: Measuring the dielectric constant of solids with the HP 8510 network analyzer*. HP Corporate Headquarters, USA: Hewlett Packard, August 1, 1985.
- [17] M. T. T. Eugene F. Knott, John F. Schaeffer, in *Radar Cross Section*. SciTech Publishing, 2004.

Chapter 3

Additive Manufactured Antennas for GPR

3.1 Introduction

The scope of this project is to eventually utilise an unmanned aerial vehicle (UAV) with the proper hardware and software to be used for humanitarian demining. One of the key challenges is to develop an antenna that is low cost to manufacture and lightweight enough to be carried by a small UAV and at the same time has ultra-wide band capabilities. In this chapter a broad range of state of the art antennas and antenna technologies is reviewed to give an overview of what technology exists. System requirements will be defined and strengths and weaknesses of the analysed antennas will be outlined. This knowledge will then be used to develop an antenna with suitable properties needed for this project.

Ultra-wide band (UWB) systems are becoming increasingly popular in many applications such as high data rate communications, ground penetrating radar, through-wall imaging, and RF localisation. UWB systems offer very high resolution for radar and localisation applications and high bit rates for communication applications. Antennas are one of the main com-

3. ADDITIVE MANUFACTURED ANTENNAS FOR GPR

ponents in such systems. For radar applications, they are desired to be directive, compact, lightweight, and have uniform radiation characteristics over the band of operation. Furthermore, having dual polarisation is useful in improved target detection and clutter rejection using an appropriate polarimetric technique. Many of the existing dual-polarized antennas do not provide sufficient bandwidth for the aforementioned UWB GPR applications, which leads us to define the design requirements for our research project and then manufacture a bespoke antenna, designed according to these requirements.

3. ADDITIVE MANUFACTURED ANTENNAS FOR GPR

3.2 System Requirements

The desire for an ultra-wide band antenna and the limitations of ground penetration in higher frequency are conflicting and thus a compromise has to be found where antenna functions over a smaller bandwidth of the frequency range between 10 MHz and 5 GHz depending on the desired resolution. Since we require a portable antenna we would usually use an electrically small antenna, which as a result is normally of low gain and broad radiation patterns.

The following requirements have been reviewed for their selection of a feasible antenna design; large fractional bandwidth, low sidelobes and low cross-talk.

1. The antenna must be able to radiate or receive fast electromagnetic transients with a spectrum between 8.2 and 12.4 GHz (X-Band) and a minimum gain of 15 dBi. This bandwidth was chosen as an optimal tradeoff between antenna size and depth penetration in the ground.
2. The antenna may be off-ground, attached to a drone, which means it must have a high directivity.
3. Another implication of the antenna being attached to a drone is small dimensions and weight.
4. Antenna properties must be independent of the ground properties.
5. The antenna must be low cost in production.

Two types of antennas that are feasible for the design of ground-penetrating radar can be divided into two groups, which are dispersive and non-dispersive antennas. Examples of dispersive antennas that have been used in ground-penetrating radar are the exponential spiral,

3. ADDITIVE MANUFACTURED ANTENNAS FOR GPR

the Archimedian spiral, the logarithmic planar antenna, the Vivaldi antenna and the exponential horn. Examples of non-dispersive antennas are the TEM horn, the bicone, the bow-tie, the resistive, lumped element loaded antenna or the resistive, continuously loaded antenna. In the following some design parameters are explained in more detail.

3. ADDITIVE MANUFACTURED ANTENNAS FOR GPR

3.2.1 Efficiency

The antenna efficiency is expressed as a ratio of the power delivered relative to the power radiated from it. A high efficiency antenna has most of the power input radiated away. A low efficiency antenna absorbs most of the power within or consumes it due to impedance mismatch.

The antenna efficiency can be written as the ratio of the radiated power to the input power of the antenna:

$$\epsilon_R = \frac{P_{radiated}}{P_{input}} \quad (3.1)$$

Antenna efficiency is expressed as a number between 0 and 1. However, antenna efficiency can generally be stated as a percentage value, as well; An antenna efficiency of 0.3 is the same as 30%. Antenna efficiency is also frequently quoted in decibels (dB). An efficiency of 0.1 equals (-10 dB) and an efficiency 0.5 equals -3 dB.

3.2.2 Sensitivity Factor

The sensitivity factor relates to the electrical and mechanical tolerances of an antenna and can be used to describe the antenna performance. Sensitivity specifies the "weakest" signal that can be received. Sensitivity is commonly quoted in V/m or Volts per meter. The field strength in V/m can be calculated as follows:

$$E = \frac{\sqrt{30P_t}}{d} \quad (3.2)$$

Where E is field strength in V/m , d is distance in meters and P_t is the power of the transmitter in Watts. It should be noted that this equation assumes 100% energy is transferred from the transmitter to the antenna, and that the antenna has unity gain (a dipole). In practice, there are losses in coupling the signal from transmitter to antenna, and also losses in the antenna itself.

3. ADDITIVE MANUFACTURED ANTENNAS FOR GPR

3.2.3 Ultra Wideband

The term ultra-wideband refers to an electromagnetic signal that has an instantaneous fractional bandwidth greater than 0.25 with respect to a center frequency. There is no accepted standard usage of UWB terms. Percentage bandwidth is also known as proportional bandwidth or fractional bandwidth.[1]

$$\%bandwidth = \frac{2(f_H - f_L)}{f_H + f_L} \quad (3.3)$$

3.3 Antennas for Ground Penetrating Radar

In this section an brief overview of the state of the art in antennas for ground penetrating radar usage is given. The antenna types and parameters are summarised in the appendix.

3.3.1 Spiral Antennas

Romsey [2] proposed the two necessary conditions to remain the frequency-independent characteristic of an equiangular spiral antenna, the "angle principle" and the "truncation principle". The "angle principle" means that the performance of the antenna defined by angle is frequency-independent. The antenna is defined by angles only, so the dimension is infinite. The "truncation principle" means that there is a finite "motivating area" for a certain to radiate energy, the area which isn't in the "motivating area" has little effect on the radiation property, so can be truncated properly.

Karlsson et al. realise a planar spiral antenna with the radius of 7.5 cm to cover a frequency range from 3.1 - 10.6 GHz. Furthermore, they show that using a pair of monofilar spiral antennas in parallel the bandwidth can be extended to 1.79 - 11 GHz at VSWR <2.

Zhao-hui et al. [3] propose a spiral antenna where the Archimedian spiral replaced the outer margin of an equiangular spiral. They found this increased the electrical length of the antenna and the lower frequencies' radiation efficiency increased notably. It was proven that

3. ADDITIVE MANUFACTURED ANTENNAS FOR GPR

the lower frequency characteristics were better than that of an equiangular spiral antenna with the same dimensions while achieving a wider bandwidth. Consequently, this method can be used to minimize an UWB antenna's radiation aperture.

Mao et al. [4] investigate the design of an equiangular antenna where the antenna is fed by an integrated microstrip balun. This way the feed is embedded in one of the spiral arms, which allows a flat design in contrast to a vertically feed in the antenna centre. In contrast to the before presented planar spiral antennas, *Liu et al.*[5] present a cylindrical spiral antenna solely developed for GPR purposes. For the design of the spiral antenna they follow the same approach as *Zhao-hui et al.* To save space, the two arms extend from the end of the planar spiral and are wrapped around the cylinder. The inside of the spiral comprises of the feeding balun and a reflection cavity. In wrapping part of the spiral arms around the cylinder they manage to significantly reduce the diameter of the whole antenna.

3.3.2 Crossed Dipoles

Etching planar antennas on substrate has the great advantage of creating a low profile, being low cost, light-weight and easy to fabricate. *Pan et al.*[6][7] propose two very simple designs for crossed dipole antennas, both designed for 2.4GHz. In one paper the authors present a crossed dipole and analyse the influence of different lengths of the arms. In the other paper the authors present a crossed curve dipole. As it turned out the curved arms have a negative influence on the impedance bandwidth and the gain deviation. Whereas the antenna with the curved arms achieves an impedance bandwidth of 270 MHz (11%) and a gain deviation of 6 dB from 880 to 940 MHz, the antenna without the curved arms achieves an impedance bandwidth of 590 MHz (24%) and a gain deviation of smaller than 4 dB over the full range. *Kumar et al.*[8] introduce a dumbbell shaped cross-dipole antenna. The antenna consists of dipoles with circular patches on both sides of the substrate. On each side of the substrate one dipole is etched, both places orthogonal to each other. Both sides of the substrate can

3. ADDITIVE MANUFACTURED ANTENNAS FOR GPR

be regarded as two separate dipole antennas. The orthogonal position results in the polarisation becoming circular. *Elsherbini et al.*[9] present a UWB antenna based on the coupled sectorial loops antenna (CSLA) concept. The antenna comprises of two single polarization elements that are asymmetrical CSLA with two sectorial loops. Dual-polarization is achieved by placing these two elements orthogonal to each other. The feed is placed at a common point between both loops. In practice the authors reach an isolation level of 20 - 30 dB. By using a back plate directional radiation is ensured. *Bai et al.*[10] present a cavity backed, detached crossed dipole antenna. This configuration is proposed to improve the feed of the antenna in the Ka - Band. The crossed dipoles are backed by a cylindrical cavity to enhance radiation performance.

3.3.3 Vivaldi Antennas

The radiation structure of a vivaldi antenna is usually tapered exponentially, which is done in one, two or three layers. The one layer structure is called tapered slot Vivaldi antenna which offers a small dimension and provides a sufficient reflection coefficient. The two layered structure is called antipodal Vivaldi antenna, which provides minimum distortion. Three layer balanced Vivaldi antipodal antennas reduce the cross polarization. *Elsheakh et al.*[11] provide a guide to optimize Vivaldi antenna performance for ground penetrating radar. Optimized dimensions for a conventional Vivaldi antenna are offered. Thick substrate is used to decrease the overall length and improve the bandwidth. To reduce the resonant frequency without degrading the antenna performance six pairs of regular squared slots are etched on the ground plane of the Vivaldi antenna.

3.3.4 Dielectric Rod Antennas

Artificial dielectric loading has been used with antennas for surface-penetrating radar. However, the finite size of the dielectric can cause problems in that energy becomes trapped in

3. ADDITIVE MANUFACTURED ANTENNAS FOR GPR

the dielectric and has the effect of causing a local resonance. Provided, therefore, that the antenna can be loaded in such a way that the dielectric appears semi-infinite, this problem is reduced.

Dielectric rod antennas have numerous advantages over conventional wave-guide and horn antennas. They have low insertion loss, broadband input match, high mutual decoupling efficiency and low cost manufacturing.

Kazemi et al.[12] present an Vivaldi antenna feed for a dielectric rod antenna. Furthermore various rod antennas of different materials are compared, including a uniform Teflon rod, a two-layer corrugated Teflon rod, a two-layer corrugated rod from Teflon and Ultem, a two-layer straight rod from Teflon and Ultem. It is concluded, that using a multi-layer rod is ideal for imaging applications due to a wider operating frequency range, significantly lower beam squint and less dispersion for narrow pulse transmission and reception. *Kumar et al.*[13] present a configuration method for producing a higher gain with a dielectric rod antenna made of Teflon. *Leib et al.*[14] present a dielectric rod antenna fed by a planar circular slot. The planar structure consists of a circular slot antenna supplied by a dipole. A broadband and low-dispersive antenna performance is achieved. Furthermore, an additional reflector at the backside of the antenna is increases the directivity. One downside of dielectric rod antennas is, that their footprint tends to be small and thus a scanning of a potential mine field might become too time consuming.

3.3.5 Horn Antennas

The horn is widely used as a feed element for satellite dishes. In addition to its utility as a feed for reflectors and lenses, it is a common element of phased arrays and serves as a universal standard for calibration and gain measurements of other high-gain antennas[15].

Strycek et al.[16] propose a tapered slot antenna for use in ground penetrating radar. The antenna works in a frequency range of 0.5 to 3 GHz and has a peak gain of 12 dBi. The

3. ADDITIVE MANUFACTURED ANTENNAS FOR GPR

authors investigate the influence of grid sidewalls on the performance. It was found that exponentially flaring strip ridges and logarithmic alignment of ten wires in the grid sidewalls show the best results for this frequency band by still providing structural stability to the whole antenna.

Jamali et al.[17] introduce the design of a ultra wideband TEM horn for ground penetrating radar purposes. Their horn antenna is designed for a frequency range from 2 to 19 GHz. *Panzer et al.*[18] present a tiny double-ridged horn antenna for subsurface radar applications. The small TEM double-ridged horn antenna for radar applications is designed for a frequency range of 6-20 GHz. The authors focus on miniaturization of the antenna for compact dimensions and portable operations. Different horn antennas have been simulated with tapered walls. The best proposed results have been achieved with the TEM horn, tapered walls and two inserted ridged walls. In the paper it is concluded, that this antenna design is optimal for ground penetrating radar applications.

3.4 Novel Fabrication Techniques

3.4.1 Construction

In addition to the standard antennas and there variations presented here, there are some authors that focus on different techniques to deploy an antenna. Research is done on foldable or flexible antennas. This would be useful in our project to maybe wrap a flexible antenna around a UAV or use an examined origami technique to adapt a proven antenna technology to the shape of a UAV. *Kimionis et al.*[19] introduce a folding origami technique that enables a developer to design and produce an antenna in a planar way and then fold it to its final shape. Their technique has the potential to notably reduce design and manufacturing costs.

3. ADDITIVE MANUFACTURED ANTENNAS FOR GPR

3.4.2 Additive Manufactured Horn Antenna

The paper review on antennas for ground penetrating radar, leads us to the idea of using additive manufacturing techniques for printing a horn antenna and thus meeting our design goals, as previously defined in 3.2. For additive manufacturing three materials are available. There's Acrylonitrile butadiene styrene (ABS), polylactide (PLA) and stereolithography (SLA) for producing objects from plating and metal powders for producing objects from metal (sintering). Since a horn antenna has a high directivity, plastic is relatively lightweight, compared to other materials, and additive manufacturing is low cost this already suffices points two, three and five of our design requirements.

Lopez et al.[20] present a 3D printed Volcano Smoke antenna for UWB applications. Their antenna has an impedance bandwidth from 3.2 to 12.6 GHz. In their paper they proof that it is possible to 3D print even rather complicated structures in steel. The antenna is composed of a cylindrical cone with a sphere inscribed at its top. To enhance the conductivity and solderability the antenna was electroplated with copper. *Farooqui et al.*[21] present a two turn helical antenna that has been integrated to a dielectric lens, using 3D printing ABS technology. As a result the antenna provides a peak gain of 16 dBi at a frequency of 9.4 GHz. Achieving a similar gain without a lens would normally require 20 turns, according to the authors. The antenna has been produced monolithically using metallic ink to print the helical antenna.

Garcia et al.[22] evaluate the effects of surface roughness by comparing the effects of 3D printed horns to a standard commercial horn. They proof that the surface roughness has no measureable effect on the performance of the 3D printed horn antenna. By using conductive ABS material the authors produce a flexible UWB bow-tie antenna that achieves an impedance bandwidth of 24.18% [23]. *Wu et al.*[24] propose 3D printing technology to fabricate inhomogeneous dielectrics. They can be used to achieve one focus on the surface

3. ADDITIVE MANUFACTURED ANTENNAS FOR GPR

and the other focus at infinity. They can also be used to increase the gain and narrow the beamwidth of a horn antenna.

3.5 Design of an additive manufactured X-band horn antenna

We want to design an optimised aperture antenna with similar performance to a standard gain horn antenna in the X-band range (8.2-12.4 GHz). After calculating our design parameters we are going to simulate such a horn with Ansys HFSS and eventually 3D print this antenna and experiment with different coating materials and techniques to achieve best possible antenna characteristics.

3.5.1 Analytic Equations and Results

The design is guided by classical equations for pyramidal horn antennas as given in *Balanis* (see 3.1). However, the design procedure is included, since we incorporate through the specification important but subtle design changes.

The dimensions p_e and p_h of Figure 3.1 are given by the following equations

$$p_h = (b_1 - b) \left[\left(\frac{\rho_e}{b_1} \right) - \frac{1}{4} \right]^{1/2} \quad (3.4)$$

$$p_e = (a_1 - a) \left[\left(\frac{\rho_h}{a_1} \right) - \frac{1}{4} \right]^{1/2} \quad (3.5)$$

$$\left(\sqrt{2\chi} - \frac{b}{\lambda} \right)^2 (2\chi - 1) = \left(\frac{G_0}{2\pi} \sqrt{\frac{3}{2\pi}} \frac{1}{\sqrt{\chi}} - \frac{a}{\lambda} \right)^2 \left(\frac{G_0^2}{6\pi^3} \frac{1}{\chi} - 1 \right) \quad (3.6)$$

where

$$\frac{\rho_e}{\lambda} = \chi \quad (3.7)$$

3. ADDITIVE MANUFACTURED ANTENNAS FOR GPR

$$\frac{\rho_h}{\lambda} = \frac{G_0^2}{8\pi^3} \left(\frac{1}{\chi} \right) \quad (3.8)$$

To design our horn antenna we aim for the same gain as the Narda standard gain horn (15dB). We know the dimensions of our waveguide, which is a WR90. The remaining dimensions to determine that lead to an optimum gain, are a_1 , b_1 , ρ_1 , ρ_2 , P_e , P_h . We want to design our X-band horn (8.2 - 12.4 GHz) to have a gain of 15 dB at $f = 10.3GHz$. The inner dimensions of the WR90 are $a = 0.9$ in (2.286 cm) and $b = 0.4$ in (1.016 cm).

First we convert our G_0 to a dimension less quantity.

$$G_0 = 15 = 10 \log_{10} G_0 \Rightarrow G_0 = 10^{1.5} = 39.8 \quad (3.9)$$

Since $f_c = 10.3GHz$, $\lambda = 2.9126$ cm and the initial value for χ is taken using, as:

$$\chi_1 = \frac{191.97}{2\pi\sqrt{2\pi}} = 2.527 \quad (3.10)$$

Using equations (3.7) and (3.8) we arrive at,

$$\rho_e = 2.527\lambda = 7.36cm \quad (3.11)$$

$$\rho_e = 2.527\lambda = 7.36cm \quad (3.12)$$

The corresponding values for a and b are

$$a_1 = \frac{G_0}{2\pi} \sqrt{\frac{3}{2\pi\chi}} \lambda = 8.02cm \quad (3.13)$$

$$b_1 = \sqrt{2\chi} \lambda = 6.53cm \quad (3.14)$$

The computed radiation patterns for the principal E and H-planes are plotted in Figure 3.3. The radiation patterns are nearly symmetric over the main beamwidth $\pm 25^\circ$ and closely resemble those of the Narda with a nearly identical gain.

3. ADDITIVE MANUFACTURED ANTENNAS FOR GPR

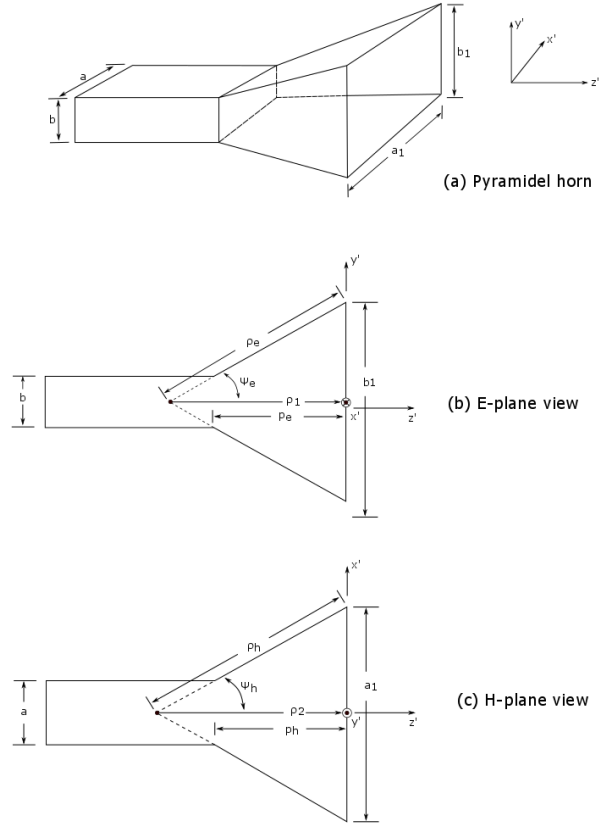


Figure 3.1: Pyramidal horn and coordinate system.

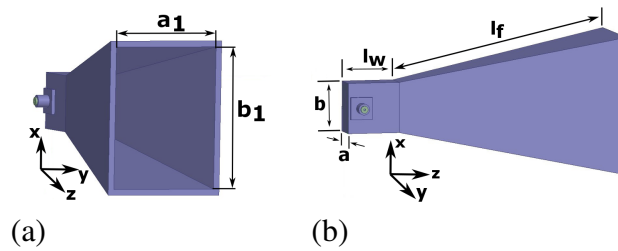


Figure 3.2: Schematic design of the 3D printed Pyramidal horn antenna (a) end view (b) side view.

3. ADDITIVE MANUFACTURED ANTENNAS FOR GPR

Table 3.1: Dimensions of the Pyramidal antenna shown in Figure 3.2 (units in mm).

aperture (a_1, b_1)	(54.5, 73.0)
flare length l_f	133.0
waveguide (a, b)	(10.16, 22.28)
waveguide section length l_w	30.0
wall thickness t	3.0
feed diameter d	7.0

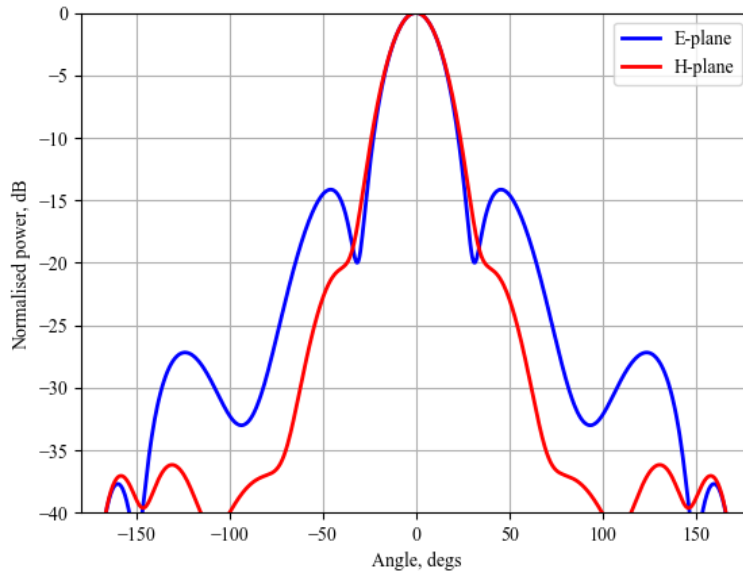


Figure 3.3: Calculated principal E and H radiation patterns for the Pyramidal Horn antenna.

3.5.2 Antenna Simulation

An HFSS [25] model (Figure 3.2) was constructed that included many other features of the horn such as a 40 micron thick copper coating applied to the ABS ($\epsilon_r = 2.7$) plastic form of the antenna and the SMA coaxial launcher and wire probe. Further numerical design iterations were performed to optimise the (ρ_e, ρ_h) dimensions (the lengths from the horn aperture to the imaginary apex of the horn in E and H planes, see [26]) and (i) provide identical 3dB beamwidth in both E and H-planes and (ii) reduce cross-polarised levels below

3. ADDITIVE MANUFACTURED ANTENNAS FOR GPR

30 dB or more. The final dimensions are given in Table 3.1 and resulted in a flare length of 5.5λ and simulated gain of 16.6 dBi at 10 GHz.

Another important parameter w.r.t. the horn antenna is determination of the phase center. The knowledge or design of an antenna's phase center is important in many different applications. Full consideration but care must be taken to define the phase center appropriately when used since its definition has subjective qualities *.

The phase center is a point where a single spherical wave emitter can be placed, equivalent to the antenna system under consideration with respect to the phase of the E and H-field radiated. The center of this sphere is the true origin of the antenna co-ordinate system for measuring radiation patterns, processing synthetic apertures down ranges profiles and the focal point for any external lens structure attached to the antenna as performed in Chapter 4.

For antennas with a phase center and a multi-lobe field pattern with distinct nulls between them, the field phase in adjacent lobes differs by 180° . In this case, the phase center is considered within the limited angles of the -3dB main lobe of the radiation pattern i.e $+/- 15^\circ$. In practice the position of the phase center depends on the frequency of the signal used and we consider 8.0, 10 and 12.4GHz, the direction of radiation and polarization alignment with simulated complex far-field E_y component.

The computation of radiated fields is performed and from inspection of the phase front versus angle at 10GHz the origin of the wave is observed to lie behind the horn aperture. A brute-force parametric optimization task was setup in HFSS iteratively stepping and plotting the phase field patterns in range 0-100 mm into (behind) the antenna aperture along the aperture central (z) axis. The HFSS function peak-to-peak calculated the change in complex angle for the far-field E_y component in the range -15 to $+15$ degrees.

*When using high-frequency reflecting or focusing systems, the problem of searching for the antenna phase center always arises, since proper operation of a mirror or lens is possible only if the focus is on an antenna phase wave front in the form of a sphere and the center of this sphere is in the focus of the antenna. With any deviations, both the shape of the phase front from the sphere, and the efficiency of the focussing system falls, because its radiation pattern is distorted.

3. ADDITIVE MANUFACTURED ANTENNAS FOR GPR

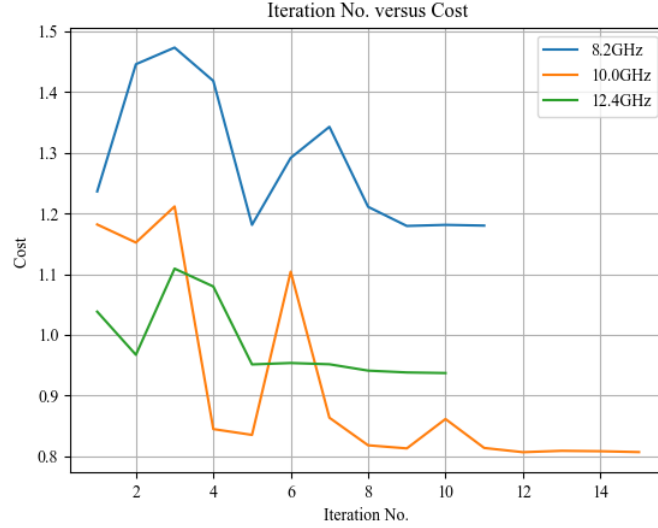


Figure 3.4: HFSS simulation of antenna phase centre for the Pyramidal horn antenna.

The calculation is performed fairly quickly, because the far-field data are related to post-processing and do not require re-solving of the model. Figure 3.4 plots the cost function (difference in peak complex phase across the E_y field component) as a function of frequency. It can be seen that the cost function is at a first minimum at the fifth iteration for all frequencies. The small difference in relative cost function levels is due to the relative differences in phase field shape. The fifth iteration on phase center range corresponds to the phase centre 55.1 mm inside (behind) the horn aperture.

The simulated results for the radiation patterns and input reflection coefficients are compared with measurements in the Results Section 3.5.3.4.

3.5.3 Antenna Manufacture

3.5.3.1 Antenna Additive Manufacture

The HFSS Pyramidal horn antenna design was exported as an HDL5 file to Solidworks where layout modifications such as material type definitions and waveguide wall thickness were increased to 3 mm.

3. ADDITIVE MANUFACTURED ANTENNAS FOR GPR

The print material was non-conducting white coloured Acrylonitrile Butadiene Styrene (ABS) with an $\epsilon_r=2.72$ and $\tan \delta=0.02$. Products manufactured from ABS possess good mechanically strength, chemical inertness and can tolerate environments temperatures changes between -20 and 80 °C.

At a temperature of 210° the ABS filament becomes molten and is extruded from the CNC printer nozzle with a diameter of 0.4 mm and layer thickness 0.1 mm using machine standard parameters for ABS materials. The support structure is then dissolved using a Stratasys SCA-1200 (support cleaning apparatus) and WaterWorks P400SC solution which contains a weak concentration of Sodium Hydroxide.

3.5.3.2 Coating and Electroplating Experiments

Conductive coatings were then applied to four 3D printed Pyramidal horn antennas. The skin depth of copper at 12 GHz is 10 μm thus a coating of 40 μm was considered adequate to support electromagnetic fields inside the horn antenna and contain skin depth penetration. Prior to application of conductive finishes both interior and exterior printed part surfaces were polished using P150 grade silicon carbide papers.

Zinc and Copper spray paints were applied to two printed horns. Both are solvent based and take an hour or two to dry out and have a surface resistivity of 0.7 Ω/sq and 20 Ω/sq , respectively for a 50 μm thick coating. A third 3D printed horn had 50 μm thick copper tape cut to shape and fixed to the inner surfaces of the horn and waveguide. Finally, a fourth test piece was commercially copper electroplated[27]. with a 40 μm copper coating applied. Figure 3.5 shows the four horn antenna apertures with the different conductive finishes applied.

The quality of surface finish varied a lot dependent upon the surface treatment. While Zinc and Copper spray was relatively easy to apply in spray form it did not spread evenly over the ABS part. In particular, the Zinc spray finish brittle as it dried and eventually cured with significant surface resistance. In contrast the Copper spray adhered well and provided

3. ADDITIVE MANUFACTURED ANTENNAS FOR GPR

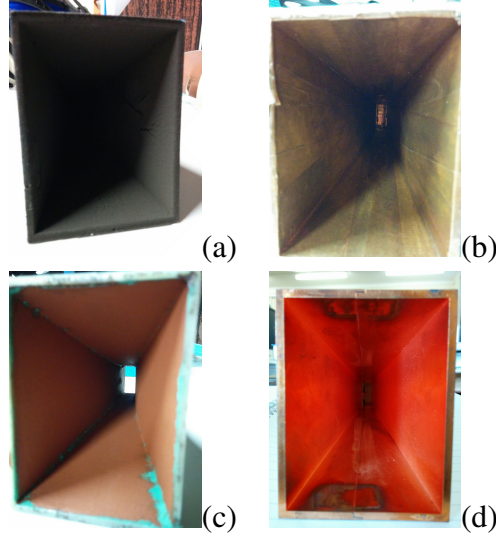


Figure 3.5: Horn antenna apertures showing different conductive surface finishes applied (a) Zinc, (b) Copper tape, (c) Copper spray and (d) Copper electroplating.

a fairly even coat over flat surfaces. However, internal corners proved problematic to obtain even surface finishes. The Copper tape adhered well to the ABS parts but was difficult to polish internal electrically bonded seams and corners. Copper electroplating the 3D printed part provided an even coverage and required little surface polishing.

3.5.3.3 Impedance Match and Coating Performance

An SMA coaxial probe with interference fit tolerance was inserted into the waveguide aperture to excite the TE_{01} mode. The probe was located $\lambda/4$ from the back wall of the waveguide and the probe length determined to provide the optimum impedance match. Figure 3.6 shows the simulated and measured reflection coefficient for the probe length $L_p = 9.6 \pm 0.2$ mm. The quality of the match while ≤ -10 dB does not display the resonance behaviour of the simulation suggesting the probe length in practice may need to be adjusted. The final 3D printed and copper electroplated horn antenna is shown in Figure 3.8.

The performance of the different coatings on the 3D printed antennas was qualitatively

3. ADDITIVE MANUFACTURED ANTENNAS FOR GPR

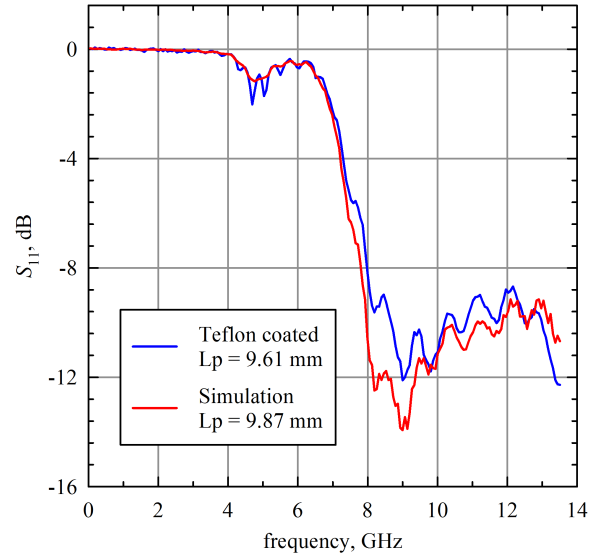


Figure 3.6: Simulated and measured optimum feed length.

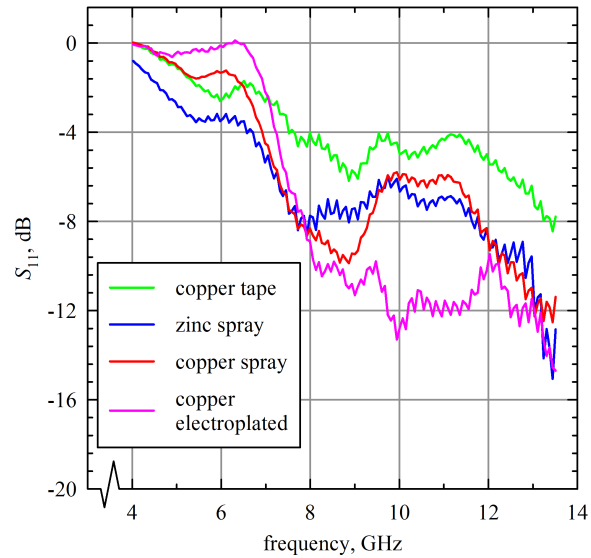


Figure 3.7: Measured reflection coefficient responses S_{11} for the Pyramidal horn for different metal coating applied.

3. ADDITIVE MANUFACTURED ANTENNAS FOR GPR



Figure 3.8: Additive manufactured and copper electroplated horn antenna.

3. ADDITIVE MANUFACTURED ANTENNAS FOR GPR

assessed by measuring the S_{11} reflection coefficient for the horn antennas. It was thought this would give a measure of the uniformity and surface resistance of the coatings. The optimum matched probe length was used for all antennas and Figure 3.7 shows the results. It is evident that the copper electroplating provided the best match and most uniform coating.

3.5.3.4 Radiation Patterns Performance

The measured and simulated E-plane and H-plane radiation patterns for the fabricated horn prototype antenna are presented in Figure 3.9 for different frequencies of operation. The radiation patterns show good correspondence between the measured and simulated co-polarised patterns in both planes. The plots show measured cross-polar field levels are below 30 dB, while simulated levels were below 40 dB. The average half power beamwidth for the E-plane and H-plane co-polar patterns were 28° and 30° , respectively with a peak measured gain of 15 dBi and 16.6 dBi calculated at 10 GHz. The simulated radiation efficiency was calculated around 96%.

The measured gain is calculated using equation (3.15) [26] which assumes antennas are polarisation matched and symbols have their usual meaning. Frequency dependent cable losses and the quality of individual antenna impedance matches are taken into account.

$$P_r = P_t \left(\frac{\lambda}{4\pi R^2} \right)^2 G^2 L_{cable} (1 - |\Gamma_t|^2)(1 - |\Gamma_r|^2) \hat{\mathbf{a}}_t \cdot \hat{\mathbf{a}}_r \quad (3.15)$$

The measured and simulated gain versus frequency as well as the measured and simulated reflection coefficient of the horn antenna are illustrated in Figure 3.10. The plot shows a gain response of over 15.1 dBi for frequencies above 8.2 GHz with a peak gain of 17 dBi at 12.4 GHz. The measured gain is in good agreement with the HFSS simulated result. The reflection coefficient is well under 10 dB for the 8.2 - 12.4 GHz bandwidth.

3. ADDITIVE MANUFACTURED ANTENNAS FOR GPR

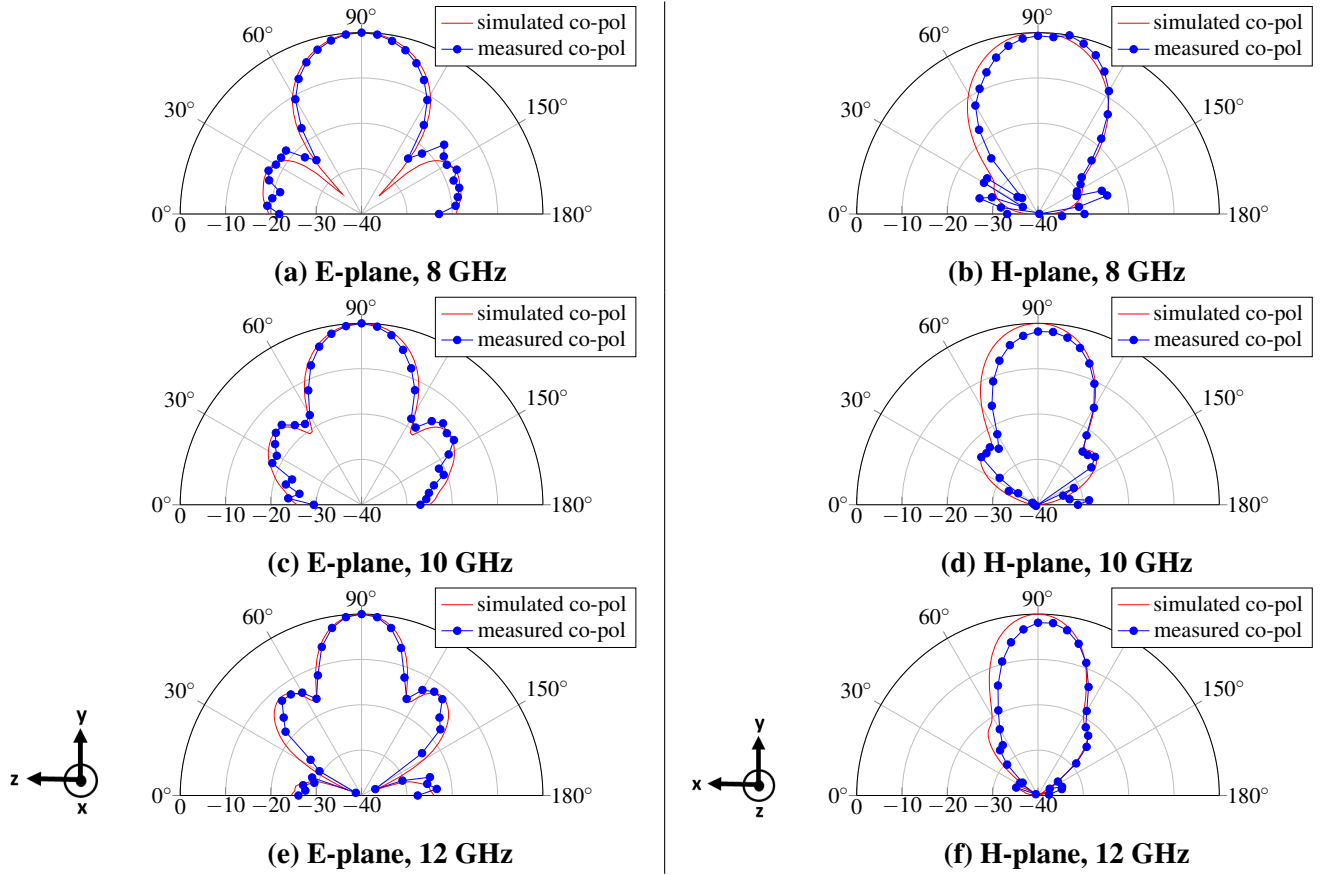


Figure 3.9: Simulated and measured radiation patterns of the manufactured pyramidal horn antenna in the E-plane and H-plane over the 8-12 GHz frequency range (measured data only covers 0-180°).

3. ADDITIVE MANUFACTURED ANTENNAS FOR GPR

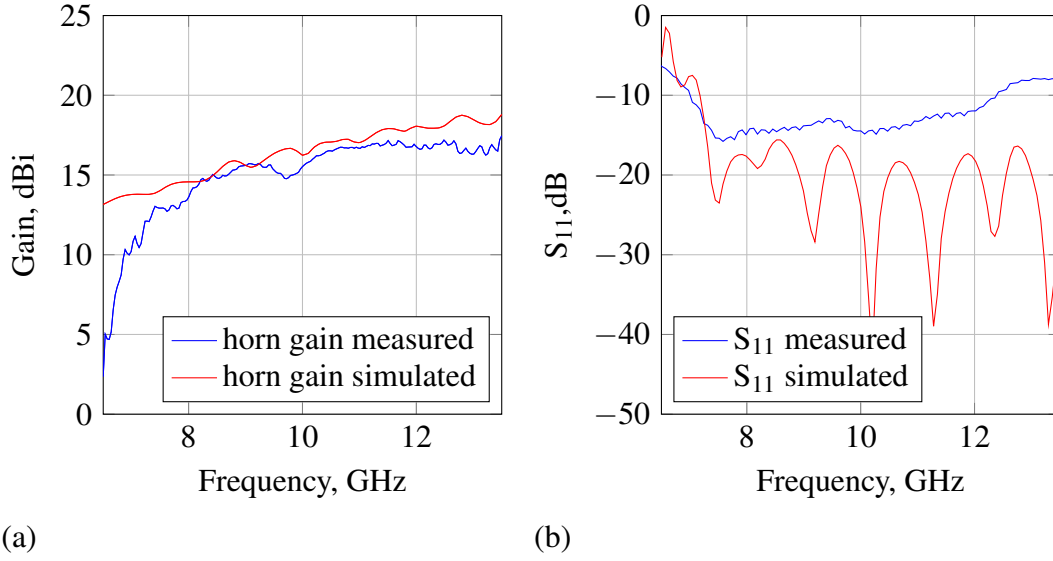


Figure 3.10: (a) Measured and simulated antenna gain, (b) Measured and simulated reflection coefficient.

3.6 Horn Antenna Array

For gathering full polarimetric data of a scene, an antenna mount, incorporating four antennas, has been designed. The antenna mount incorporates two 3D printed, copper-electroplated horn antennas and two Narda standard gain horns. The readily assembled mount is shown in Figure 3.11 where the inset depicts the orientation of the horn apertures, when looking directly at the array, the numbers identify individual antennas.

The space between the antenna apertures was chosen to be 0.5λ to reduce antenna cross-talk so that the system cross-talk (between polarisations) is dominated by antenna cross-talk. Figure ?? demonstrates the measured S_{11} response for all the antennas in the array are well matched. Figure 3.12 shows the measured co-polar mutual coupling in E- and H-planes of the polarimetry array are less than -35 dB and the cross-polar mutual coupling in E- and H-planes is less than -60 dB.

3. ADDITIVE MANUFACTURED ANTENNAS FOR GPR

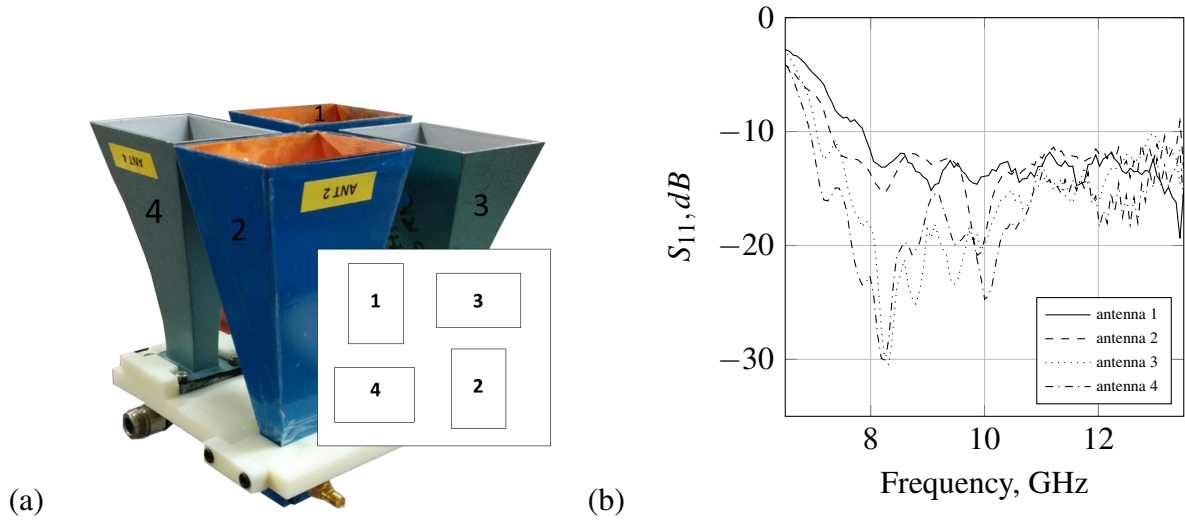


Figure 3.11: (a) Polarimetry array incorporating two 3D printed horn antennas (1, 2) and two commercial horns (3, 4) (b) S_{11} measured at the terminals of the horns.

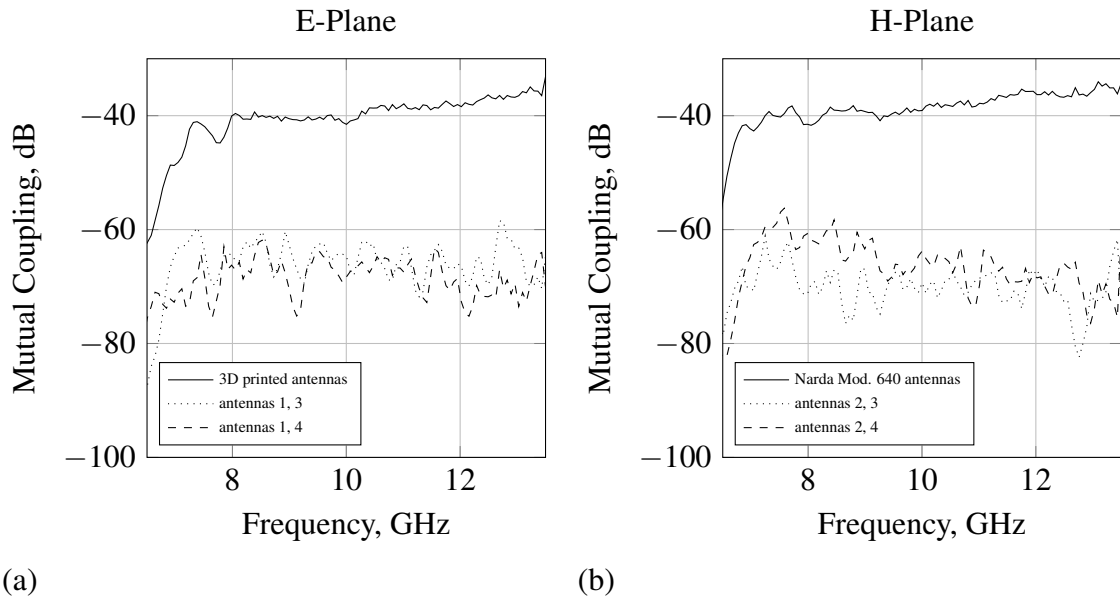


Figure 3.12: (a) Co- and cross-polar mutual antenna coupling in E-plane, (b) Co- and cross-polar mutual antenna coupling in E-plane.

3. ADDITIVE MANUFACTURED ANTENNAS FOR GPR

3.7 Summary Comments

A comprehensive and detailed review of state-of-the-art in GPR antenna design and analysis was performed. This high-lighted several new antenna types and new design and manufacture techniques. In the context of this thesis it was decided to 3D print a horn antenna, lightweight enough to suffice our design requirements. The simulation and manufacturing work for a printed horn antenna has been outlined.

Initial work on the antenna design methodology has focused on 3D printing a conventional horn. Experiments with conventional metallic paints indicated that while the antenna was weakly radiating the losses were also too high. Copper electroplating provided the most uniform metal coating and simulations predicted a less than 15 dB impedance match. The measured antenna gain results showed good correlation with simulation and the measured cross-polar power levels were all less than -25 dB. The resultant antenna is lightweight (60% lighter than an equivalent metal cast antenna), low cost and feasible to manufacture. For taking full polarimetry measurements of a scene an antenna array has been designed to incorporate four X-band horn antennas, two commercial and two additive manufactured. Measurement of the co-polar mutual coupling in E- and H-planes of the polarimetry array are less than -35dB and the cross-polar mutual coupling in E- and H-planes less than -60dB.

3. ADDITIVE MANUFACTURED ANTENNAS FOR GPR

References

- [1] J. D. Taylor, in *Introduction to Ultra-Wideband Radars Systems*. CRC Press, 1995, ch. 1, p. 2.
- [2] B. Cheo, V. Rumsey, and W. Welch, “A solution to the frequency-independent antenna problem,” *IRE Transactions on Antennas and Propagation*, vol. 9, no. 6, pp. 527–534, November 1961.
- [3] Song Zhao-hui, Qiu Jing-hui, and Li Hong-mei, “Novel planar complex spiral ultra-wideband antenna,” in *ICMMT 4th International Conference on, Proceedings Microwave and Millimeter Wave Technology, 2004.*, Aug 2004, pp. 35–38.
- [4] S.-G. Mao, J.-C. Yeh, and S.-L. Chen, “Ultrawideband circularly polarized spiral antenna using integrated balun with application to time-domain target detection,” *Antennas and Propagation, IEEE Transactions on*, vol. 57, no. 7, pp. 1914–1920, July 2009.
- [5] Na Liu, Pengfei Yang, and Weijiang Wang, “Design of a miniaturized ultra-wideband compound spiral antenna,” in *2013 IEEE INTERNATIONAL CONFERENCE ON MICROWAVE TECHNOLOGY COMPUTATIONAL ELECTROMAGNETICS*, Aug 2013, pp. 255–258.
- [6] G. Pan, Y. Li, Z. Zhang, and Z. Feng, “An isotropic-radiated planar antenna using two crossed dipoles,” in *Microwave and Millimeter Wave Technology (ICMMT), 2012 International Conference on*, vol. 3, May 2012, pp. 1–4.
- [7] G. Pan, Y. Li, Z. Zhang, and Z. Feng, “Isotropic radiation from a compact planar antenna using two crossed dipoles,” *IEEE Antennas and Wireless Propagation Letters*, vol. 11, pp. 1338–1341, 2012.

3. ADDITIVE MANUFACTURED ANTENNAS FOR GPR

- [8] R. Kumar, B. Huyart, J. Cousin, and K. Mabrouk, “Dual-circular polarized dumbbell-shaped crossed-dipole planar antenna for uwb application,” in *Antennas and Propagation (EuCAP), 2013 7th European Conference on*, April 2013, pp. 1474–1478.
- [9] A. Elsherbini and K. Sarabandi, “Dual-polarized coupled sectorial loop antennas for uwb applications,” *Antennas and Wireless Propagation Letters, IEEE*, vol. 10, pp. 75–78, 2011.
- [10] X. Bai, S.-W. Qu, and R.-L. Xia, “Ka-band cavity-backed detached crossed dipoles for circular polarization,” *Antennas and Propagation, IEEE Transactions on*, vol. 62, no. 12, pp. 5944–5950, Dec 2014.
- [11] D. M. Elsheakh and E. A. Abdallah, “Novel shape of vivaldi antenna for water detection using gpr,” in *Antennas and Propagation (MECAP), 2012 Middle East Conference on*, Dec 2012, pp. 1–4.
- [12] R. Kazemi and A. Fathy, “Dielectric rod antenna with substrate integrated waveguide planar feed for wide band applications,” in *Antennas and Propagation Society International Symposium (APSURSI), 2012 IEEE*, July 2012, pp. 1–2.
- [13] C. Kumar, V. V. Srinivasan, V. K. Lakshmeesha, and S. Pal, “Design of short axial length high gain dielectric rod antenna,” *IEEE Transactions on Antennas and Propagation*, vol. 58, no. 12, pp. 4066–4069, Dec 2010.
- [14] M. Leib, A. Vollmer, and W. Menzel, “An ultra-wideband dielectric rod antenna fed by a planar circular slot,” *IEEE Transactions on Microwave Theory and Techniques*, vol. 59, no. 4, pp. 1082–1089, April 2011.
- [15] C. A. Balanis, “Horn antennas,” in *Antenna Theory - Analysis and Design*, J. Fagerberg, D. C. Mowery, and R. R. Nelson, Eds. John Wiley and Sons, 1982, ch. 13, p. 739.

3. ADDITIVE MANUFACTURED ANTENNAS FOR GPR

- [16] M. Strycek, I. Hertl, R. Pavlik, and V. Polacek, “Tapered slot antennas for ground penetrating radar,” in *Ground Penetrating Radar (GPR), 2010 13th International Conference on*, June 2010, pp. 1–4.
- [17] A. A. Jamali and R. Marklein, “Design and optimization of ultra-wideband tem horn antennas for gpr applications,” in *General Assembly and Scientific Symposium, 2011 XXXth URSI*, Aug 2011, pp. 1–4.
- [18] B. Panzner, A. Jöstingmeier, and A. Omar, “A tiny double-ridged horn antenna for sub-surface radar applications,” in *Antennas and Propagation (EuCAP), 2013 7th European Conference on*, April 2013, pp. 1322–1325.
- [19] J. Kimionis, M. Isakov, B. Koh, A. Georgiadis, and M. Tentzeris, “3d-printed origami packaging with inkjet-printed antennas for rf harvesting sensors,” *Microwave Theory and Techniques, IEEE Transactions on*, vol. 63, no. 12, pp. 4521–4532, Dec 2015.
- [20] A. Garcia Lopez, E. Lopez C, R. Chandra, and A. Johansson, “Optimization and fabrication by 3d printing of a volcano smoke antenna for uwb applications,” in *Antennas and Propagation (EuCAP), 2013 7th European Conference on*, April 2013, pp. 1471–1473.
- [21] M. Farooqui and A. Shamim, “A 3d printed helical antenna with integrated lens,” in *Antennas and Propagation USNC/URSI National Radio Science Meeting, 2015 IEEE International Symposium on*, July 2015, pp. 324–325.
- [22] C. Garcia, R. Rumpf, H. Tsang, and J. Barton, “Effects of extreme surface roughness on 3d printed horn antenna,” *Electronics Letters*, vol. 49, no. 12, pp. 734–736, June 2013.
- [23] M. Mirzaee, S. Noghianian, L. Wiest, and I. Chang, “Developing flexible 3d printed antenna using conductive abs materials,” in *Antennas and Propagation USNC/URSI*

3. ADDITIVE MANUFACTURED ANTENNAS FOR GPR

National Radio Science Meeting, 2015 IEEE International Symposium on, July 2015, pp. 1308–1309.

- [24] J. Wu, X. Yu, M. Liang, and H. Xin, “Antenna radiation pattern control through 3d printed inhomogeneous dielectrics,” in *Radio Science Meeting (Joint with AP-S Symposium), 2015 USNC-URSI*, July 2015, pp. 353–353.
- [25] Ansys:HFSSv18.1. (2016) Getting started with HFSS: Begineers guide. [Online]. Available: <http://www.ansoft.com>
- [26] C. Balanis, in *Antenna theory, analysis and design*. Hoboken, New Jersey: John Wiley and Sons, 2005.
- [27] Protolabs:Online. (2020) Welcome to protolabs: Digital manufacture. [Online]. Available: <https://www.protolabs.co.uk/>

Chapter 4

Additive Manufactured Lenses for GPR

In this chapter the insertion of a constant thickness lens into the antenna aperture is described. To be able to move the antenna array over a measurement scene in the near-field, it is necessary to convert the spherical waves of the antennas to planar waves. For doing so, it was decided to deploy lenses, which would also let us benefit from focusing capabilities. This means a flat lens, designed as a block, is physically attached to the antenna aperture and the antenna/lens-integration can thus be used as one piece for scanning the subsurface. The lens is designed from solid ABS material of a permittivity of $\epsilon_r = 2.72$ and then, towards the outside, rings with stepped down permittivity values. This is done by vertically introducing a different amount of cylinders of air (which here is called inclusion: $\epsilon_i = 1.0004$), depending on the desired permittivity for each ring of the lens. In total, the lens is comprised of six rings with a different dielectric value, with the outer ring having a permittivity of 1.3. This is due to the fact, that the manufacturing capabilities bear a certain constraint on how thin a wall thickness can be printed and a ring with 1.3 in permittivity was found to be the limit. Four lenses are manufactured and attached to the antenna array, which was presented in the previous chapter. One contribution of this chapter is that an antenna/lens integration was evaluated and put into practice of subsurface scanning for the first time.

4. ADDITIVE MANUFACTURED LENSES FOR GPR

4.1 Lenses For Millimeter Wave Applications

This section is meant to give a brief overview of the recent research that has been conducted on different materials and shapes for designing lenses for millimeter wave applications. *Teggatz et al.*[1] have designed a biconvex dielectric lens made of artificial wood and experimentally investigated its use for ground penetrating radar applications. A 20 dB standard gain horn antenna has been used as a feed, with a distance between the horn and the lens being 15 cm, while the distance to the surface of the ground is 16 cm. It is shown that the resolution of GPR can be enhanced significantly by using a dielectric lens and can further be improved by using background subtraction. In contrast to the artificial wooden lens, early research has been conducted in introducing a variation of cylindric holes in a flat Perspex plate to achieve a lens-like behaviour of varied permittivities as presented by *Goatley et al.*[2]. In more recent research, *Zhang et al.*[3] have presented a 3D printed lens, manufactured from polylactide (PLA), for microwave applications. Their lens is comprised of several concentric dielectric rings with relative permittivities for transforming spherical waves into plane waves. Usually the lens is located some distance in front of the antenna at the near-field/far-field boundary. A variety of design approaches and 3D printing techniques have been recently reported. Hyperbolic profile lenses have been transformed to equivalent flat lens designs. The refractive index may be made to vary by fabricating the lenses as a series of sub-wavelength unit cells with tailored dielectric value. Recent efforts [4], [5] have investigated 3D printing metal particles and dielectrics. These artificial dielectrics are reported to have larger dielectric value permitting construction of thinner lenses. Alternatively, metamaterial surfaces based on slots cut in cascaded dielectrics have been proposed [6] at millimeter wave frequencies. This rapidly converts near-field spherical wavefronts emerging from the antenna phase center into planar phase fronts with enhanced directivity in the desired direction [7].

4. ADDITIVE MANUFACTURED LENSES FOR GPR

4.1.1 Analytic Equations and Results

For designing the flat lens, it is firstly important to determine the lens' focal point. The focal point here equates the phase centre of the horn antenna, which in chapter 3 was experimentally determined to be 55.1 mm behind the antenna aperture, which equated to the length F in Figure 4.1.

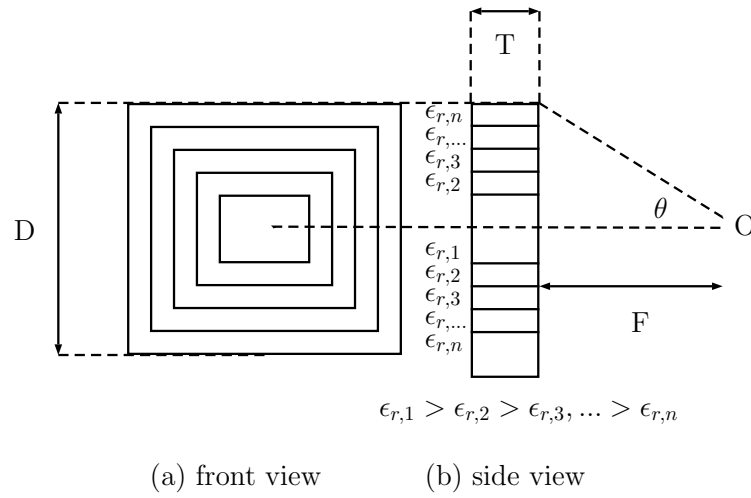


Figure 4.1: Sketch showing the constant thickness lens composed of annular rectangular ring of decreasing dielectric constant material.

Figure 4.1 shows a constant thickness, T , rectangular shaped dielectric lens[†] composed of variable refractive index medium ($n = \sqrt{\epsilon_r}$) and with focal point F located on its axis of symmetry. The refractive index decreases linearly from a maximum at the centre of the lens to a value of 1.3 at the perimeter. Each ring was chosen to be 10 mm wide. One feasible 3D printing technique that would approximate this variation is incremental stepping of the refractive index. This permits fabrication as a series of annular rectangular sections of increasing size and decreasing permittivity towards the lens perimeter. The relationship between the radially varying ϵ_r and angle of incidence θ can be shown to be [8],

[†]generated by rotation about the principal axis.

4. ADDITIVE MANUFACTURED LENSES FOR GPR

$$T \left(\epsilon_r - \frac{2}{3} \sin^2(\theta) \right) = \sqrt{\epsilon_r - \sin^2(\theta)} \times \left[\sqrt{\epsilon_m T} - (\sec(\theta) - 1) \right] \quad (4.1)$$

where T is the lens thickness, ϵ_m the maximum permittivity of the lens at the centre and ϵ_r is the relative permittivity of a particular annular section at θ degrees to the focal point. Equation (4.1) is the basic design equation for the planar graded refractive index (GRIN) lens and is solved by the root bisection method in Table 4.1 to determine discrete values of T for θ . An initial estimation of the lens proportions may be made knowing the maximum value of $\theta = 55^\circ$ is determined by the diameter of the lens and the focal length is fixed at $F = 50$ mm. One practical method is to exploit dielectric mixing principles and introduce shaped air voids into the base material. The mixing theory for determining the ratio of ABS and air inclusions used here is the Maxwell-Garnett mixing theory, with Rayleigh approximation may be solved to determine the effective dielectric constant of the mixture [9] as:

$$\epsilon_{eff} = \epsilon_m \frac{2\delta_i(\epsilon_i - \epsilon_m) + \epsilon_i + 2\epsilon_m}{2\epsilon_m + \epsilon_i + \delta_i(\epsilon_m - \epsilon_i)} \quad (4.2)$$

The base material for manufacturing the lens is ABS with permittivity $\epsilon_m = 2.72$ and the air inclusion permittivity $\epsilon_i = 1.0004$, where δ_i is the volume fraction of the inclusion. The effectiveness of the Maxwell Mixing theory was compared to measuring different ABS samples from [3] and a simple linear volume mixing relationship. The result is shown in Fig 4.2. It can be shown, that the effective permittivity follows a nearly linear relationship. Equation (4.1) was solved subject to the constraints imposed on practical realisation of effective dielectric value and a fixed focus length. The computed results are summarised in Table 4.1. It can be seen that the ideal lens thickness is between 47 – 51 mm and a trade-off value of 50 mm thickness for the lens design was chosen.

4. ADDITIVE MANUFACTURED LENSES FOR GPR

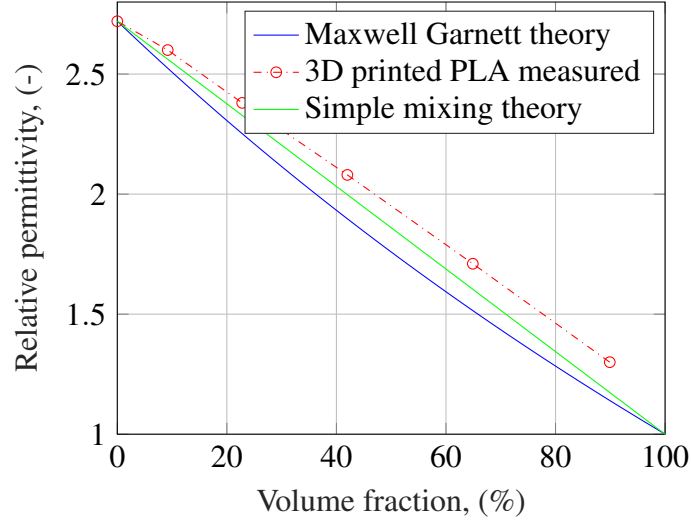


Figure 4.2: Comparison of effective permittivity model prediction and measured permittivity for PLA and air over a range of volume fractions.

Table 4.1: Summary design data on the GRIN lens. Tabulated values of lens thickness versus annular rectangular section radius, effective dielectric constant and PLA/air volume fractions for the seven annular sections (the * value indicates a suspect T value)

Ring No.	R (mm)	θ (deg)	T (mm)	ϵ_{eff}	$\delta_i\%$
1	10	5.0	49.69	2.72	100
2	20	15.0	48.49	2.60	90.8
3	30	25.0	45.96	2.38	77.1
4	40	35.0	45.02	2.08	58.0
5	50	45.0	43.70*	1.71	35.1
6	60	55.0	47.85	1.30	10.1
7	70	65.0	47.31	1.20	9.89

4. ADDITIVE MANUFACTURED LENSES FOR GPR

4.1.2 Lens Manufacture

In the next step the lens is manufactured using a Stratasys uPrint SE printer. The lens is comprised of six concentric rectangular sections, each with an annular width of 10 mm. A fabrication constraint is also imposed on the minimum value of ϵ_r which can be printed and maintain the lenses structural strength. A feasible approach is to synthesis “artificial” dielectric values between 1.3 - 2.7. Two approaches were taken to 3D printing the dielectric lens; the first was to 3D print the lens as a single whole piece and the second involved 3D printing each annulus separately and carefully push fitting together to form one whole lens. The latter approach was adopted since it allowed flexibility in modifying individual rings without reprinting the whole structure. The completed 3D printed GRIN lens is shown in Figure 4.3.

4. ADDITIVE MANUFACTURED LENSES FOR GPR

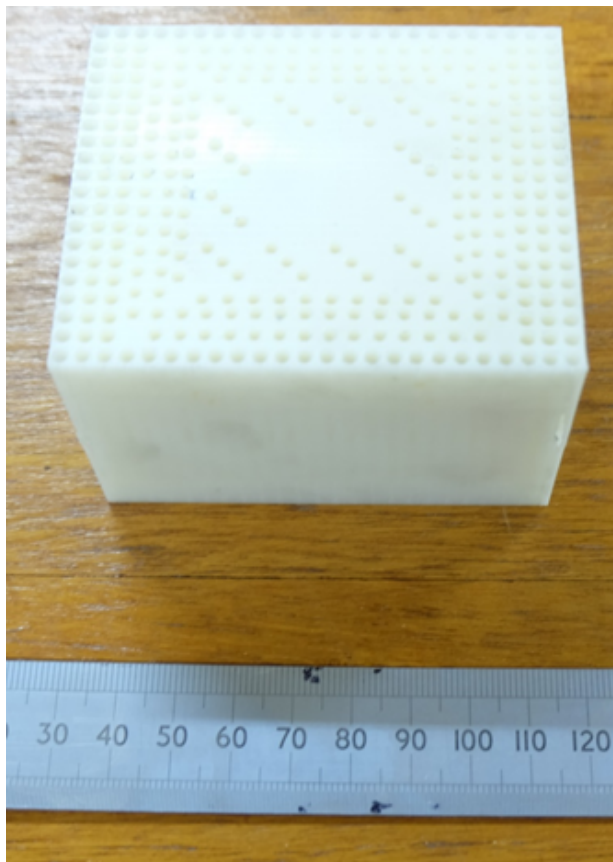


Figure 4.3: Photograph of the rectangular printed flat GRIN lens.

4. ADDITIVE MANUFACTURED LENSES FOR GPR

4.2 Results of Antenna and Lens Integration

The manufactured lens was then attached to the a horn antenna and S_{11} and gain measurements were performed and then compared to the simulation results. Figure 4.4 shows the reflection coefficient for the 3D printed horn antenna with and without the lens attached to the antenna aperture. It is observed that the near-field lens has not affected the impedance match and appears to have improved it at higher frequencies. This implies that the introduction of any impedance matching layer is not required. Figure 4.5 shows the measured and simulated gain are also in good agreement, the near-field lens has increased the antenna gain by 2.4 - 3.0 dB across the 8.2 - 12.4 GHz bandwidth and introduced a perturbation in the gain. In the next step four lenses were attached to all antennas in our antenna array and the S_{11} and cross-talk was evalutated for all four antennas and compared to the same measurements with lenses off. As can be seen from Figure 4.6 all the antennas are well matched over the 8.2 - 12.4 GHz operation frequency. Figure 4.7 shows the measured co-polar mutual coupling in E- and H-planes of the polarimetry array are less than -50 dB and the cross-polar mutual coupling in E- and H-planes is less that -60 dB.

4. ADDITIVE MANUFACTURED LENSES FOR GPR

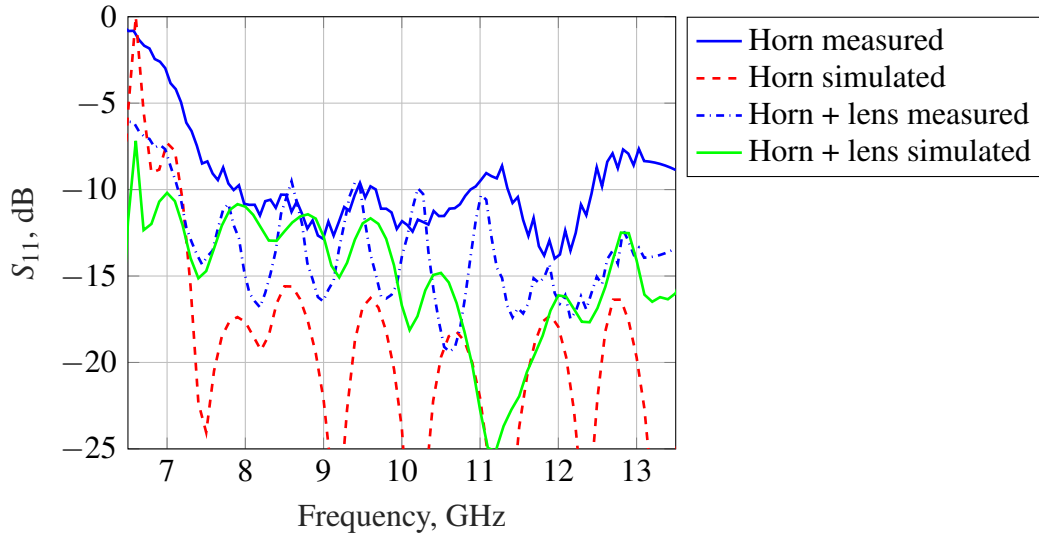


Figure 4.4: Measured and simulated reflection coefficient of 3D printed horn antenna with and without near-field lens.

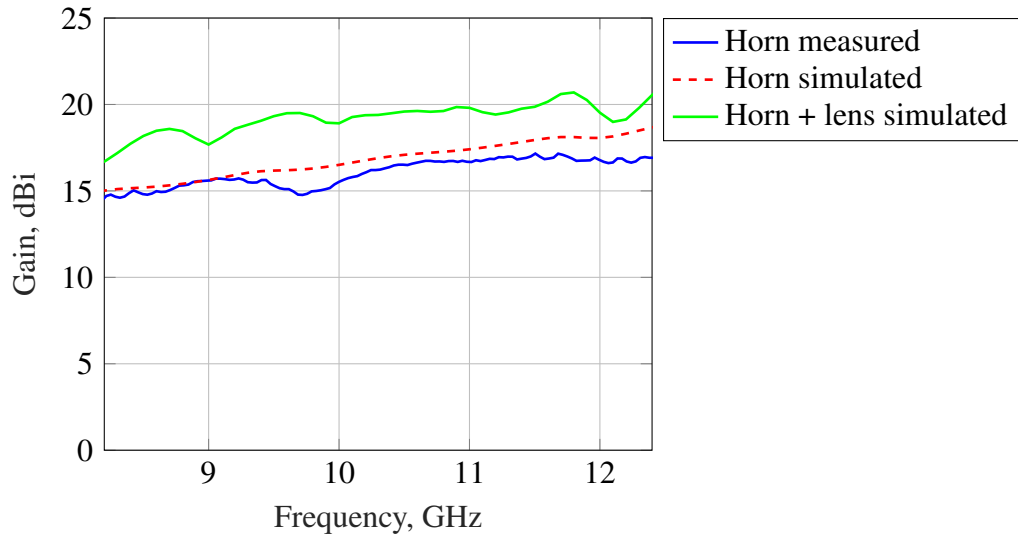


Figure 4.5: Measured and simulated gain of 3D printed horn antenna with and without near-field lens.

4. ADDITIVE MANUFACTURED LENSES FOR GPR

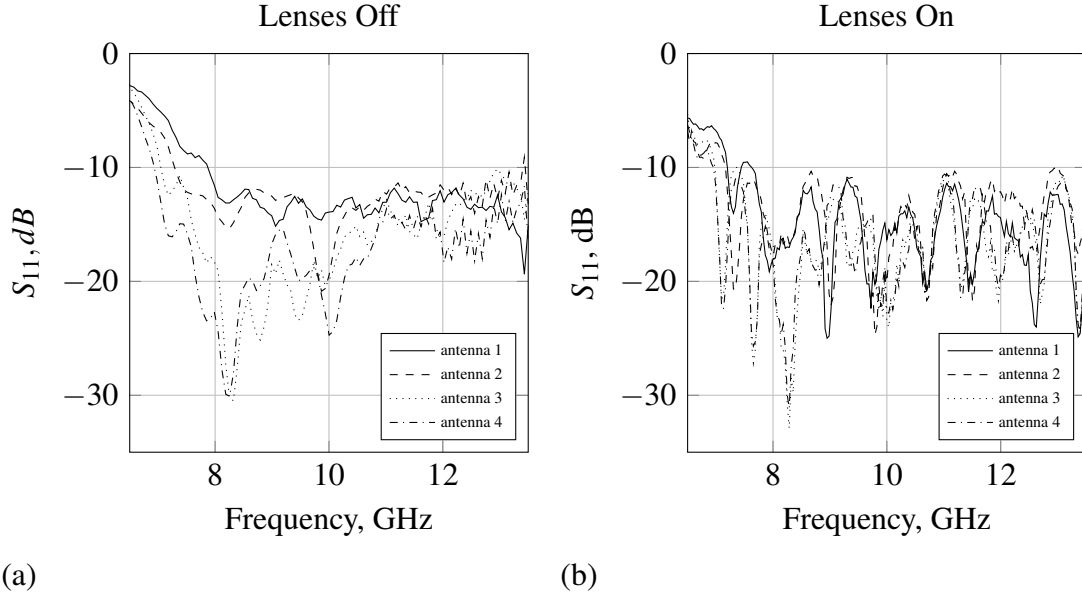


Figure 4.6: (a) S_{11} measurement of all four antennas in the array without lenses attached to antenna apertures, (b) S_{11} measurement of all four antennas in the array with lenses attached to antenna apertures.

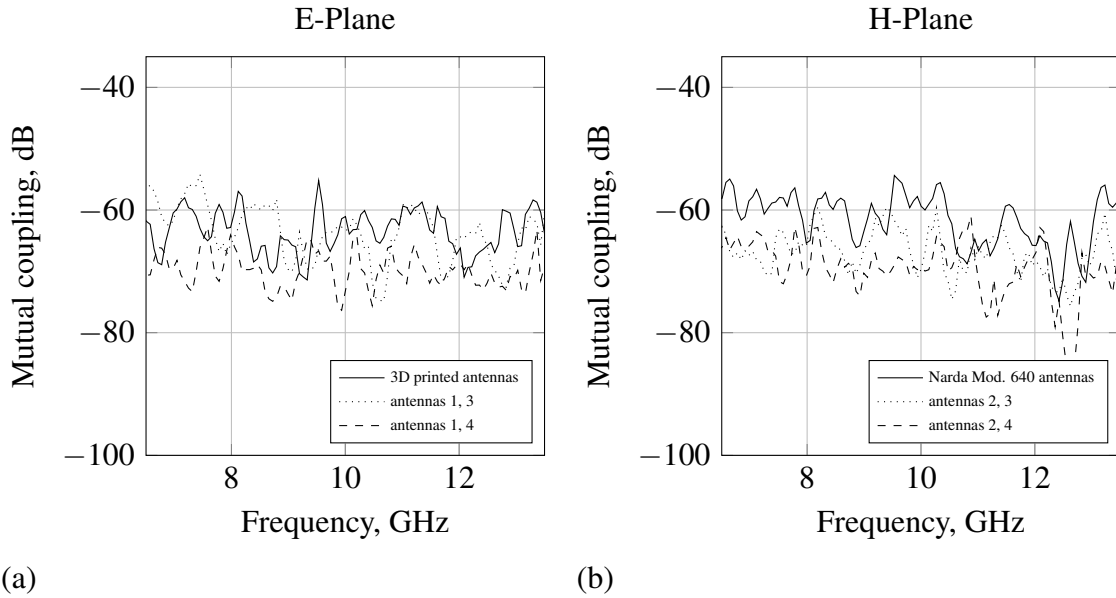


Figure 4.7: (a) Co- and cross-polar mutual antenna coupling in E-plane, measured with lenses attached to antenna apertures, (b) Co- and cross-polar mutual antenna coupling in E-plane, measured with lenses attached to antenna apertures.

4. ADDITIVE MANUFACTURED LENSES FOR GPR

4.3 Polarimetric Near-field SAR and First Results

For testing the focusing capabilities of the antenna array with attached lenses versus lenses not attached the usual testing environment was used to perform sub-surface scans. The transmitter power is 0 dBm and the GPR system is configured to sequentially measure the scattering parameter S_{21} across the X-band (8.2-12.4 GHz) frequency spectrum in all possible combinations available from the H- and V-antennas. Then the full scattering matrix (HH, HV, VH, HH) data for a given position can be collected. The antenna array is horizontally scanned from a height of 58 cm above the ground surface. In the preliminary experiments conducted, to determine the performance of the lenses, polarimetric imagery was acquired over a laboratory test lane consisting of a sand ($3.0 \times 1.2 \times 0.8$) m in square area and depth and shown in Figure 4.9. Located in the scene is a buried PMN-1 anti-personnel landmine (position D) as well as several calibration targets. These include a 40 mm metal sphere (position A), a 70 mm dihedral (position B) rotated 22.5° to its horizontal seam to provide equal co- and cross-polar returns and buried trihedral to provide a strong co-polar response. The calibrated polarimetry SAR scan imaging results for the antenna array without lenses are shown in Figure 4.10. It is evident that all the objects are present in VV and HH polarisations. The dihedral, as would be anticipated, is also present with an equally strong signal power in cross-polarisations, HV and VH. The sphere and trihedral have no cross-polar return as would be expected. The PMN-1 landmine backscatter response is a little stronger in VV than HH polarisation while absent in both HV and VH polarisation. This experiment demonstrates how polarimetry can be used to effectively discriminate buried objects. The calibrated polarimetry SAR scan imaging results for the antenna array with lenses attached are shown in Figure 4.11. All calibration objects and buried targets are again present and shifted down range a few centimeters, however they are more localised than those processed without the lenses attached, which is due to the enhanced gain of the lensed array.

4. ADDITIVE MANUFACTURED LENSES FOR GPR

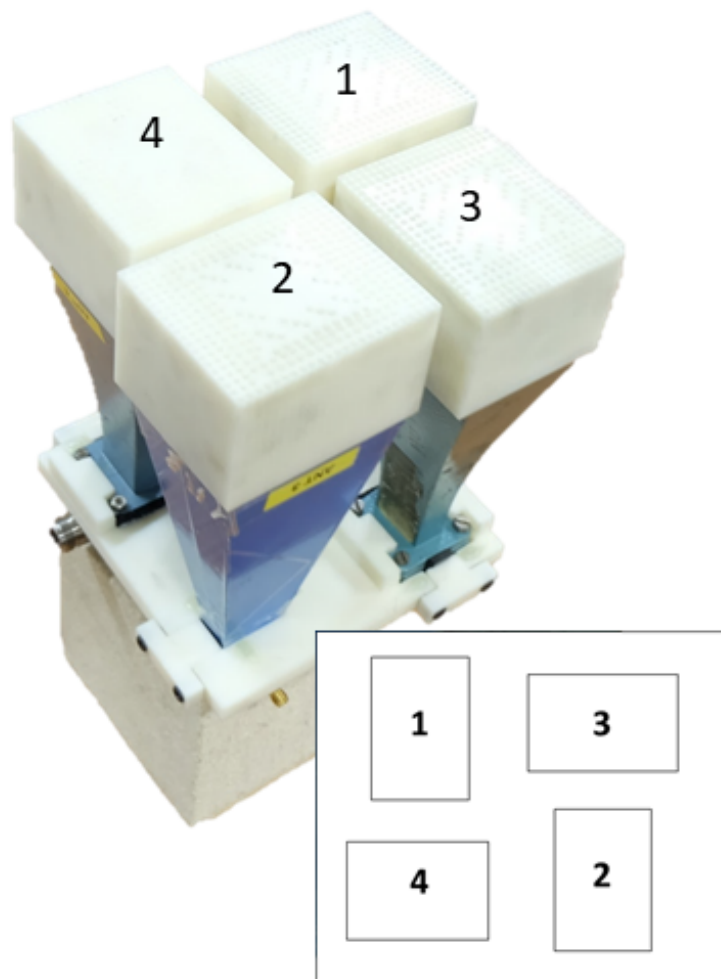


Figure 4.8: Polarimetry array incorporating two 3D printed horn antennas (1, 2) and two commercial horns (3, 4).

4. ADDITIVE MANUFACTURED LENSES FOR GPR

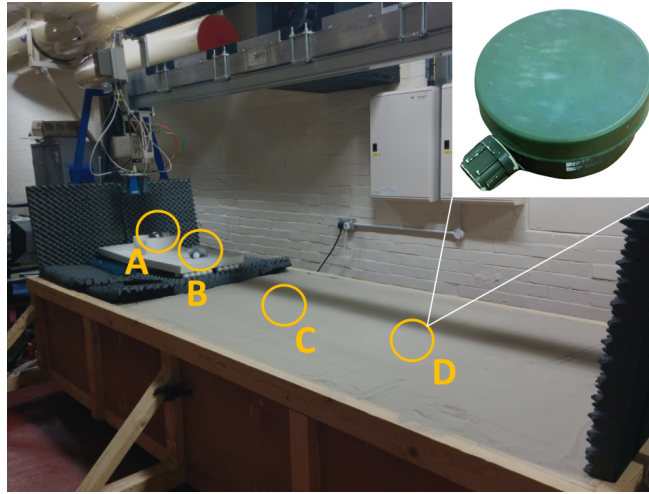


Figure 4.9: Laboratory sand bay with several calibration objects(A = sphere, B = dihemispherical, C = trihedral) and a PMN-1 landmine (D).

4.4 Summary Comments

Because experimental measurements with this GPR system will be performed in the near-field a lens was designed to fit onto the horn antenna aperture. The lens is designed as a GRIN lens that transforms spherical waves into planar waves and also offers focusing capabilities. The lens provides an enhanced gain of 2.4-3.0 dB over that of the horn antenna without lens attached. The antenna array was then arranged with four lenses attached and measurements show that the antenna cross-talk levels are below -50 dB. An experimental set-up for performing full-polarimetry measurements has then been described and initial microwave measurements for different surface laid and buried targets and reference objects were taken. The results show, that the lenses attached to the horn antennas indeed supply focusing capabilities.

For just investigating the polarimetry array and lens performance and showing the isolated targets the background data was subtracted from the target data. In a real world environment, e.g. mine field, it is likely impossible to take a background scan of the scene, which arises in cluttered data and makes it difficult to identify buried targets when the data is plotted.

4. ADDITIVE MANUFACTURED LENSES FOR GPR

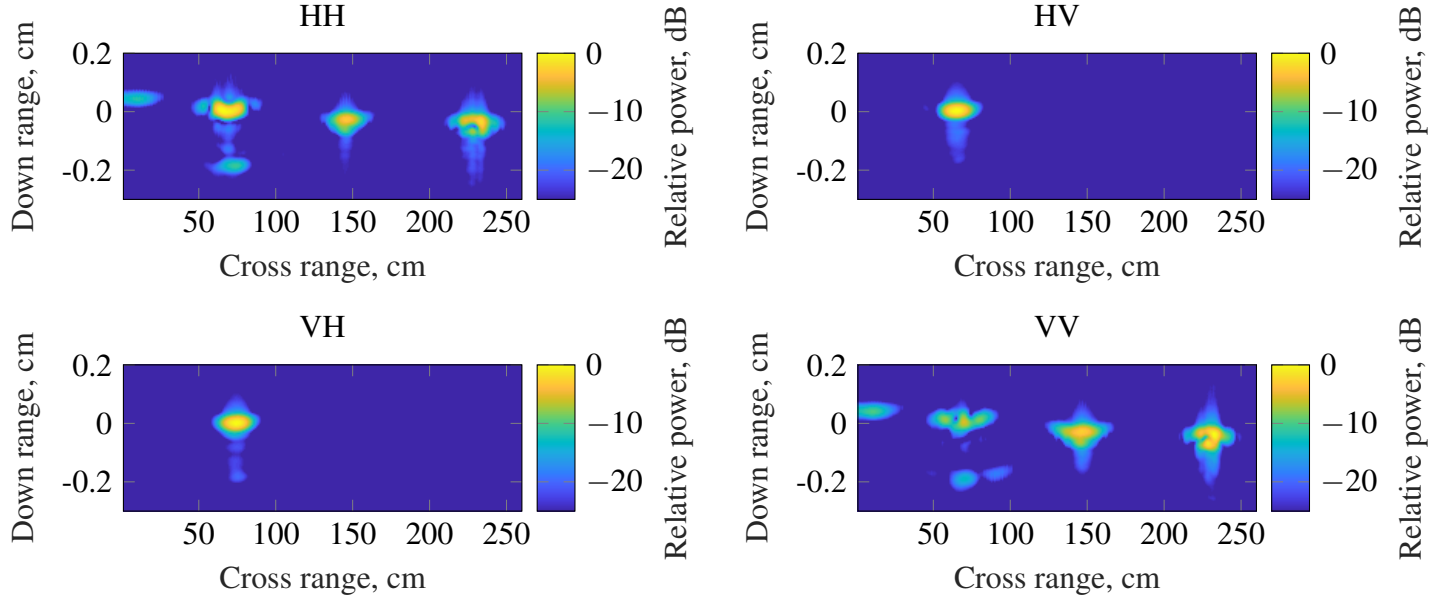


Figure 4.10: B-scans without lenses attached.

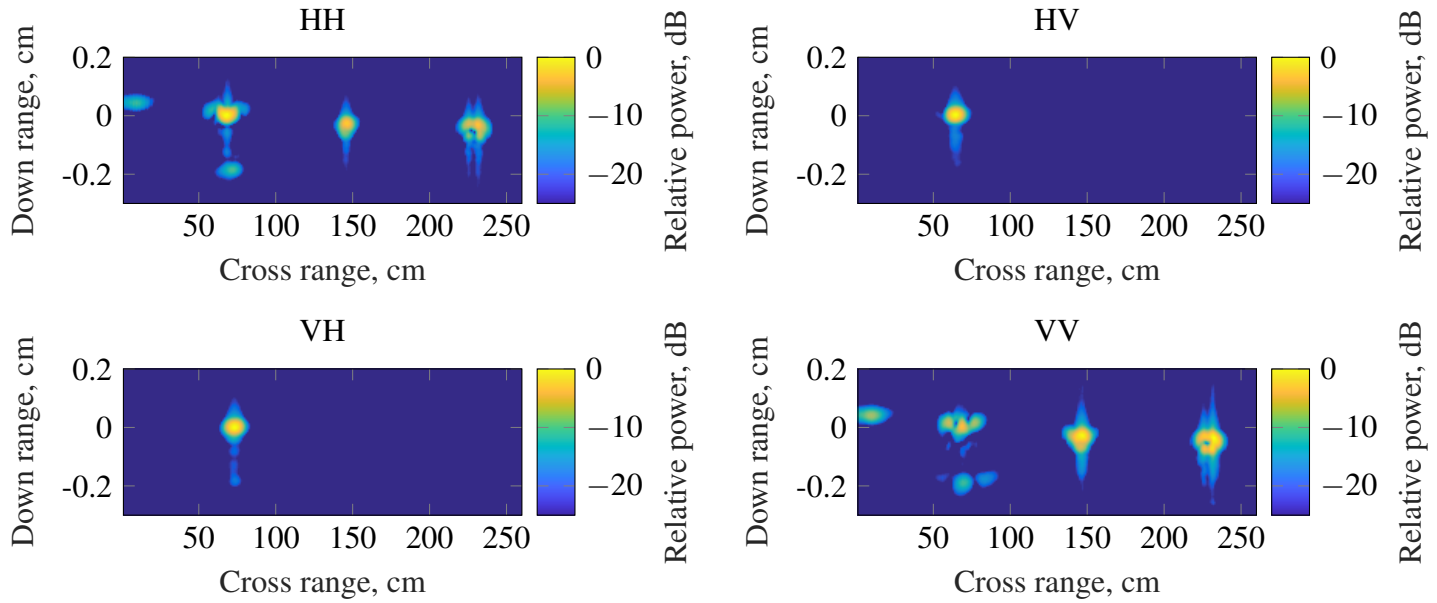


Figure 4.11: B-scans with lenses attached.

In the next chapter we will look into applying classic clutter reduction and clutter removal algorithms and will investigate enhanced differential interferometry techniques applied to the collected B-scan data.

4. ADDITIVE MANUFACTURED LENSES FOR GPR

References

- [1] A. Teggatz, A. Jostingmeier, and A. S. Omar, “Application of a dielectric lens for focusing of a gpr,” in *Antennas and Propagation Society International Symposium, 2007 IEEE*, June 2007, pp. 1461–1464.
- [2] C. Goatley and C. Parker, “Symmetrical microwave lenses,” in *1958 IRE International Convention Record*, vol. 3, 1955, pp. 13–19.
- [3] S. Zhang, Y. Vardaxoglou, W. Whittow, and R. Mittra, “3d-printed graded index lens for rf applications,” in *2016 International Symposium on Antennas and Propagation (ISAP)*, Oct 2016, pp. 90–91.
- [4] S. Zhang, W. Whittow, and J. C. Vardaxoglou, “Additively manufactured artificial materials with metallic meta-atoms,” *IET Microwaves, Antennas Propagation*, vol. 11, no. 14, pp. 1955–1961, 2017.
- [5] P. Petrov, A. Radkovskaya, C. J. Stevens, and E. Shamonina, “Superdirectivity for coupled dimers of meta-atoms at mhz,” in *2017 11th International Congress on Engineered Materials Platforms for Novel Wave Phenomena (Metamaterials)*, Aug 2017, pp. 265–267.
- [6] M. Al-Nuaimi, “Compact size high gain lens corrected pyramidal horn antenna for 71-76 ghz band.” *Third Asia Pacific Conference on Antennas and Propagation*, pp. 23-26, (2014).
- [7] T. Ding, J. Yi, and H. Li, “3d field-shaping lens using all-dielectric gradient refractive index materials.” *Scientific Reports* 7.782, DOI:10.1038/s41598-017-00681-z, (2017).
- [8] H. Jasik, in *Antenna Engineering Handbook*, ch. chapter. 16.

4. ADDITIVE MANUFACTURED LENSES FOR GPR

- [9] A. H. Sihvola and J. A. Kong, “Effective permittivity of dielectric mixtures,” *IEEE Transactions on Geoscience and Remote Sensing*, vol. 26, no. 4, pp. 420–429, July 1988.

Chapter 5

Advanced Polarimetry for Subsurface Imaging

5.1 Introduction

In the previous chapters antenna setups to probe the subsurface have been developed and preliminary experiments proved their capability of imaging the subsurface and resolving buried targets. One of the evident problems that arises from the focus of the research towards humanitarian demining is, that in most cases it will not be possible to take imaging data of an empty scene for background subtraction, since the landmines have usually been in place for decades. The research question of this chapter to answer is to find suitable imaging processes to discriminate subsurface targets, while at the same time suppress any clutter from the scene, this might be antenna ringing, the air-ground interface or subsurface clutter. For this reason the full polarimetry data acquisition of the Jones scattering matrix is begun to be exploited to provide power level clutter suppression. The mathematical formalism for the underlying physics of the scattering matrix is described and a null scattering matrix derived in a procedure similar to Yamaguchi to yield co-polar and cross-polar clutter filtered B-scan

5. ADVANCED POLARIMETRY FOR SUBSURFACE IMAGING

subsurface imagery. Techniques to evolve other clutter suppressed image products are investigated including Stokes and Pauli eigenvalue decompositions. The suitability of techniques will be assessed on collected data from both previously introduced, low- and high-band, antenna systems. Some novel results with significant suppression of clutter power levels are described. Ultimately the aim of this chapter is to provide surface and subsurface clutter suppression techniques which can directly be applied to gathered subsurface data without the need for subtracting a background scan, as well as, providing algorithms to isolate desired subsurface targets (e.g. landmines) from their surrounding clutter.

5.2 Polarised Wave

An EM signal is described by seven real quantities:

- direction of wave vector (two angles ϕ and θ)
- magnitude of wave vector (and angular frequency)
- two complex fields E_{0x} and E_{0y} (Jones vector)

5.2.1 Jones Vectors

All different polarisation states of a wave can be entirely described by their Jones vector. A Jones vector contains the complete information of the amplitudes and phases of the electric field vector's x and y components of a wave travelling in direction z. When an EM wave is traveling in z-direction the superposition of two plane waves travelling in x- and y-direction with the frequency ω is expressed as:

$$E(z, t) = \begin{bmatrix} E_{x,0} e^{i(\omega t - k_z z + \delta_x)} \\ E_{y,0} e^{i(\omega t - k_z z + \delta_y)} \end{bmatrix} = e^{i(\omega t - k_z z)} \begin{bmatrix} E_{x,0} e^{i\delta_x} \\ E_{y,0} e^{i\delta_y} \end{bmatrix} \quad (5.1)$$

5. ADVANCED POLARIMETRY FOR SUBSURFACE IMAGING

When the term $e^{i(\omega t - k_z z)}$ is dropped

$$E(z, t) = \begin{bmatrix} E_x \\ E_y \end{bmatrix} \quad (5.2)$$

E_x and E_y can be written as the product of the amplitude and phase of the electric field along the x- and y-axis,

$$E_x = |E_x| e^{i(\delta_x)} \quad (5.3)$$

$$E_y = |E_y| e^{i(\delta_y)} \quad (5.4)$$

The electric field components can be rewritten in function of the phase difference as

$$E_x = |E_x| e^{i(\delta_x) - \delta_y} \quad (5.5)$$

$$E_y = |E_y| \quad (5.6)$$

and the total field intensity is given by

$$I = I_x + I_y = E_{x,0}^2 + E_{y,0}^2 = |E_x|^2 + |E_y|^2 = E_x E_x^* + E_y E_y^* \quad (5.7)$$

With the intensity normalised to $I = 1$ we can write the linear polarisation states along the x- and y-axis as

$$E_{lin,x} = \begin{pmatrix} 1 \\ 0 \end{pmatrix} \quad (5.8)$$

$$E_{lin,y} = \begin{pmatrix} 0 \\ 1 \end{pmatrix} \quad (5.9)$$

Given the phase difference between E_x and E_y is $\pi/2$ the circular polarisation states can

5. ADVANCED POLARIMETRY FOR SUBSURFACE IMAGING

be written as

$$E_{circ,right} = \frac{1}{\sqrt{2}} \begin{pmatrix} 1 \\ i \end{pmatrix} \quad (5.10)$$

$$E_{circ,left} = \frac{1}{\sqrt{2}} \begin{pmatrix} i \\ 1 \end{pmatrix} \quad (5.11)$$

5.2.2 Scattering Matrix

Assuming the Back Scatter Alignment convention (BSA) and a Cartesian coordinate frame then the incident and scattered waves are characterized by two linear polarisations H-horizontal and V-vertical (w.r.t electric field) and are defined according to [1]. Then the polarisation scattering process at the target can be represented by a scattering matrix $[S]$ for both the monostatic and bistatic case in terms of their Jones vector,

$$\begin{bmatrix} E_H^s \\ E_V^s \end{bmatrix} = \frac{e^{jkr}}{r} \begin{bmatrix} S_{HH} & S_{HV} \\ S_{VH} & S_{VV} \end{bmatrix} \cdot \begin{bmatrix} E_H^i \\ E_V^i \end{bmatrix} \quad (5.12)$$

where E^i is the incident electric field and E^s is the scattered electric field and matrix $[S]$ is the scattering matrix and the complex scattering coefficients are a function of bistatic angle. Since the diagonal elements relate the same polarisation of incident and scattered fields, they are known as the co-polar terms, while the off-diagonal elements are known as cross-polar terms, as they relate the orthogonal polarisation of the incident and scattered fields. In the case of a monostatic system, the reciprocity theorem results in equal cross-polar terms i.e. $S_{HV} = S_{VH}$. The e^{jkr}/r term takes into account the propagation effects, both in amplitude and phase and holds only in the far-field zone.

5. ADVANCED POLARIMETRY FOR SUBSURFACE IMAGING

5.2.3 Stokes Parameters

The polarisation of a wave can be displayed on a Poincare Sphere, where the poles represent circularly polarised waves and the equator linearly polarised waves. Every other point, either on the surface or inside the sphere, correspond to elliptical polarised light [2].

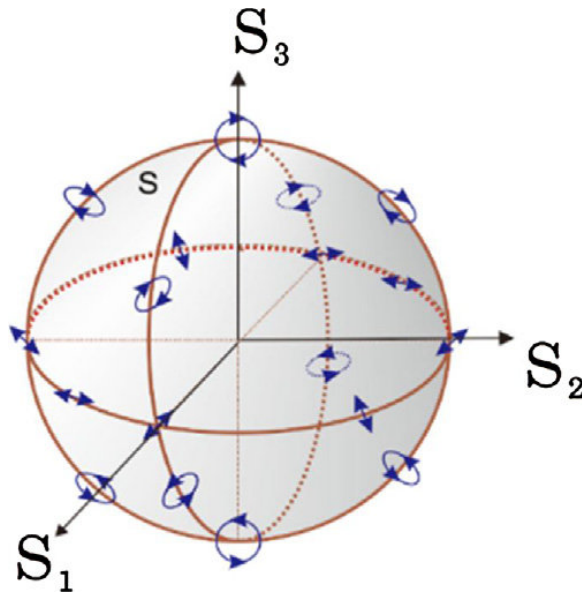


Figure 5.1: Poincare Sphere. [2]

Each point on the sphere corresponds to one polarisation state which is expressed as a Stokes parameter. The polarisation of a signal can be represented by a polarisation ellipse, having two geometric parameters. The ellipticity ε and the angle τ . The polarisation state of a plane wave can be characterised by the Stokes parameters. One can think of the antenna array from chapter 3 as a polarisation filter. In the incident wave a certain polarisation (e.g. vertical or horizontal) is produced and the reflective wave is then received by an antenna array with certain polarisations, as well. This way it can be determined to what respect the target changed the polarisation characteristics and thus certain target properties can be deduced.

Only three of these Stokes parameters are independent, they are related by the complex

5. ADVANCED POLARIMETRY FOR SUBSURFACE IMAGING

field vectors as

$$I_0^2 = Q^2 + U^2 + V^2 \quad (5.13)$$

This relation only holds true if the wave is fully polarised and can thus be used as an indicator of the quality of polarisation in our experiments.

$$I_0 = S_0 = E_V E_V^* + E_H E_H^* \quad (5.14)$$

$$Q = S_1 = E_V E_V^* - E_H E_H^* \quad (5.15)$$

$$U = S_2 = E_V E_H^* + E_H E_V^* \quad (5.16)$$

$$V = S_3 = j(E_V E_H^* - E_H E_V^*) \quad (5.17)$$

The Stokes vector representation I_0 and Q can also be used to display the individual intensities of the horizontal and vertical polarisation:

$$I_v = |E_v|^2 = (I_0 + Q)/2 \quad (5.18)$$

$$I_h = |E_h|^2 = (I_0 - Q)/2 \quad (5.19)$$

I_0 represents the total intensity of a wave, Q represents the difference between vertically and horizontally polarised intensities and U and V represent jointly the phase difference between the vertically and horizontally polarised components of the wave. All four Stokes parameters have been computed to study if they can be used as means of clutter suppression. The summation of horizontal and vertical intensities (I_0) and the difference between horizontal and vertical intensities (Q), as well as the individual intensities of vertical (I_v) and horizontal (I_h) polarisations.

5. ADVANCED POLARIMETRY FOR SUBSURFACE IMAGING

5.3 Pauli Decomposition Parameters

Coherent Pauli decomposition parameters that take account of polarisation [3] were also investigated for subsurface clutter reduction. These include Pauli a , b and c parameters which decompose the $[S]$ matrix into various scattering mechanisms. Where the a scattering matrix corresponds single scattering of a plane surface (single or odd bounce scattering). The b scattering is from a corner surface oriented at 0° (double- or even-bounce scattering) since the polarisation of the returned wave is mirrored in respect to the one of the incident wave. The c matrix scattering is from corners oriented at 45° (double- or even-bounce scattering). The decomposition parameters can be related to the $S[HV]$ basis and the Jones vector for plane polarised electromagnetic waves as,

(5.20)

$$a = \frac{(S_{HH} + S_{VV})}{\sqrt{2}} \quad (5.21)$$

$$b = \frac{(S_{HH} - S_{VV})}{\sqrt{2}} \quad (5.22)$$

$$c = \frac{(S_{HV} + S_{VH})}{\sqrt{2}} \quad (5.23)$$

5.4 Yamaguchi Polarimetry Decomposition

In [4], [5], [6] and [7] Yamaguchi, Moriyama and Boerner demonstrate that it is possible to synthesis a radar channel at any polarisation state from the scattering matrix. If E_t is the transmitted wave and E_s the scattered wave from the target then E_t can be defined by the

5. ADVANCED POLARIMETRY FOR SUBSURFACE IMAGING

Jones matrix as,

$$E_t = \frac{1}{\sqrt{1+\rho\rho^*}} \begin{bmatrix} 1 \\ \rho \end{bmatrix}. \quad (5.24)$$

where ρ is the polarisation ratio. The scattered wave is related to the transmitted wave via the scattering matrix where $S[HV]$ represents the targets polarimetric scattering characteristics in the HV basis. The co-polar powers can then be obtained from,

$$P_{co-polar} = |E_t^T \cdot S_{HH} \cdot E_t|^2 \quad (5.25)$$

where T denotes the transpose polarisation. The full expression is given as follows,

$$\begin{aligned} P_{co-polar} &= |E_t^T \cdot S_{HH} \cdot E_t|^2 \\ &= \left| \frac{[1 \ \rho]}{\sqrt{1+\rho\rho^*}} \cdot \begin{bmatrix} HH & HV \\ VH & VV \end{bmatrix} \cdot \frac{1}{\sqrt{1+\rho\rho^*}} \begin{bmatrix} 1 \\ \rho \end{bmatrix} \right|^2 \\ &= \left| \frac{[1 \ \rho]}{1+\rho\rho^*} \cdot \begin{bmatrix} HH & HV \\ VH & VV \end{bmatrix} \cdot \begin{bmatrix} 1 \\ \rho \end{bmatrix} \right|^2 \\ &= \left| \frac{HH + 2 \cdot HV\rho + VV \cdot \rho^2}{1+\rho\rho^*} \right|^2 \quad (if HV = VH) \end{aligned}$$

This leaves us with a single fraction to calculate the co-polar power.

The complex null polarisation value is calculated from the appropriate polarimetric co-polar power expression by setting it to zero and solving for the roots of the matrix as given

5. ADVANCED POLARIMETRY FOR SUBSURFACE IMAGING

by [5],

$$\rho_{co,null} = \frac{S_{HV} \pm \sqrt{S_{HV}^2 - S_{HH} \cdot S_{VV}}}{S_{VV}} \quad (5.26)$$

In the case of cross-polar power, the transmitted wave E_t is again defined by the Jones scattering matrix as,

$$E_{\perp,t} = \frac{1}{\sqrt{1 + \rho\rho^*}} \begin{bmatrix} \rho^* \\ -1 \end{bmatrix} \quad (5.27)$$

where T denotes the transpose, the subscript \perp denotes the orthogonal wave. The cross-polar power is deduced as follows,

$$\begin{aligned} P_{x-polar} &= |E_{\perp,t}^T \cdot S_{HH} \cdot E_t|^2 \\ &= \left| \frac{[\rho^* \quad -1]}{\sqrt{1 + \rho\rho^*}} \cdot \begin{bmatrix} S_{HH} & S_{HV} \\ S_{VH} & S_{VV} \end{bmatrix} \cdot \frac{1}{\sqrt{1 + \rho\rho^*}} \begin{bmatrix} 1 \\ \rho \end{bmatrix} \right|^2 \\ &= \left| \frac{[\rho^* \quad -1]}{1 + \rho\rho^*} \cdot \begin{bmatrix} S_{HH} & S_{HV} \\ S_{VH} & S_{VV} \end{bmatrix} \cdot \begin{bmatrix} 1 \\ \rho \end{bmatrix} \right|^2 \\ &= \left| \frac{S_{HH}\rho^* + S_{HV}(\rho\rho^* - 1) - S_{VV}\rho}{1 + \rho\rho^*} \right|^2 \end{aligned} \quad (5.28)$$

The roots are again found by setting equation (5.26) to zero

$$\rho_{x,null} = \frac{-B \pm \sqrt{B^2 - 4AC}}{2A} \quad (5.29)$$

5. ADVANCED POLARIMETRY FOR SUBSURFACE IMAGING

where,

$$A = S_{HH}^* S_{HV} + S_{HV}^* S_{VV} \quad (5.30)$$

$$B = |S_{HH}|^2 - |S_{VV}|^2 \quad (5.31)$$

$$C = -A^* \quad (5.32)$$

The polarimetric clutter matrix, is agnostic in the sense that it does not know the type of clutter we wish filtering e.g. it could be antenna coupling, or as here, subsurface clutter in the sand. Once the clutter region is selected the polarimetric pixels are extracted to form the clutter matrix, S_{sand} .

$$S_{sand} = \begin{bmatrix} 1.430 + 1.437j & 0.150 - 0.150j \\ 0.150 - 0.150j & 1.352 - 0.661j \end{bmatrix} \cdot 10^{-2} \quad (5.33)$$

There are two possible roots to equation (5.26) for the sand co-polar scattering matrix polarisation given below,

$$\rho_{co,1} = -1.6028 \cdot 10^{-2} + 0.8719j \quad (5.34)$$

$$\rho_{co,2} = 1.0609 \cdot 10^{-2} - 1.0372j \quad (5.35)$$

Taking the ρ value from equation (5.34) the co-polar channel power can be calculated.

For the cross-polar case, the two possible results for equation (5.29) are given below as,

$$\rho_{x,1} = 0.0417 \cdot 10^{-2} + 0.1217j \quad (5.36)$$

$$\rho_{x,2} = -2.1862 \cdot 10^{-2} - 6.9021j \quad (5.37)$$

Taken the ρ value of equation (5.36) the cross-polar power can be calculated.

5. ADVANCED POLARIMETRY FOR SUBSURFACE IMAGING

5.5 The Experiments

The aforementioned mechanisms have been applied to two sets of data, gathered from a low-band experimental setup at 0.4-4.8 GHz (Experiment 5 A) and a high-band experimental setup at 8.2-12.4 GHz (Experiment 5 B). Both experimental setups are described separately in that the different antenna systems, the experimental environment and the initial B-scans from the collected datasets are explained.

5.5.1 Experiment 5 A - Low Band Configuration

5.5.1.1 System and Antennas

The stepped frequency radar is built around a Rhode & Schwarz ZVA 10675E vector network analyser that acts as the coherent transmitter-receiver unit. The other parts of the system are the transmitting and the receiving antenna and the computer to perform the signal processing. The experimental setup is shown in Figure 5.2. The presented GPR system uses a linear polarised TEM horn as transmit antenna and two near-field probes (loop) antennas, arranged orthogonally and in front of the TEM horn, to collect the co- and cross-polar response. The loop antennas are placed just outside the near-field of the TEM horn at 12 cm in front of the aperture at 400 MHz.

5.5.1.2 Experimental Setup

The experiments have been conducted on an indoors soil facility which consists of one soil bay (2.4Lx1.2Wx0.8H meters) filled with sand; and one bay (1.2Lx1.2Wx0.8H meters) filled with RAM for placing calibration targets, such as a 40 mm sphere for co-polar calibration and a brass rod, placed in an 22.5° angle perpendicular to the direction of antenna movement, for cross-polar calibration. The soil is maintained within a 1-3% moisture content, which reflects a moisture level one would encounter in a desert area between the early morning hours and noon. Here dew in the early morning hours causes a slightly higher moisture level

5. ADVANCED POLARIMETRY FOR SUBSURFACE IMAGING

in the surface area (3%) than around noon (1%). Due to the ventilation system setup in the laboratory area all experiments were conducted at a constant temperature of 25°C . A Near-Field Measurement System (NFMS) has been erected over the two bays with a 3 m long linear automated positioner. The antenna array acquires the scattering parameter S_{21} across the 0.4-4.8 GHz frequency spectrum and takes measurements at 1 cm intervals along the horizontal x-axis. Figure 5.2 a) shows the dual polarised near-field antenna configuration. The setup uses a linear polarised TEM (Scientific Atlanta) horn that illuminates the ground scene in vertical (V) polarisation. The local back-scattered electromagnetic field is collected by two loop antennas arranged orthogonally and in front of the TEM antenna to acquire VV and VH (vertical-horizontal) co- and cross-polarised data. The loop antennas are 40 cm above the soil surface. The antenna height is typical of a stand-off GPR. This height is a trade-off between such factors as the energy attenuation, decreasing the antenna-soil coupling, avoiding possible obstacles of the ground surface, and forming sufficient antenna footprint for future SAR processing. To make orthogonal polarisation measurements, i.e. HH and HV, the antenna array is rotated clockwise by 90° and data taken.

5. ADVANCED POLARIMETRY FOR SUBSURFACE IMAGING

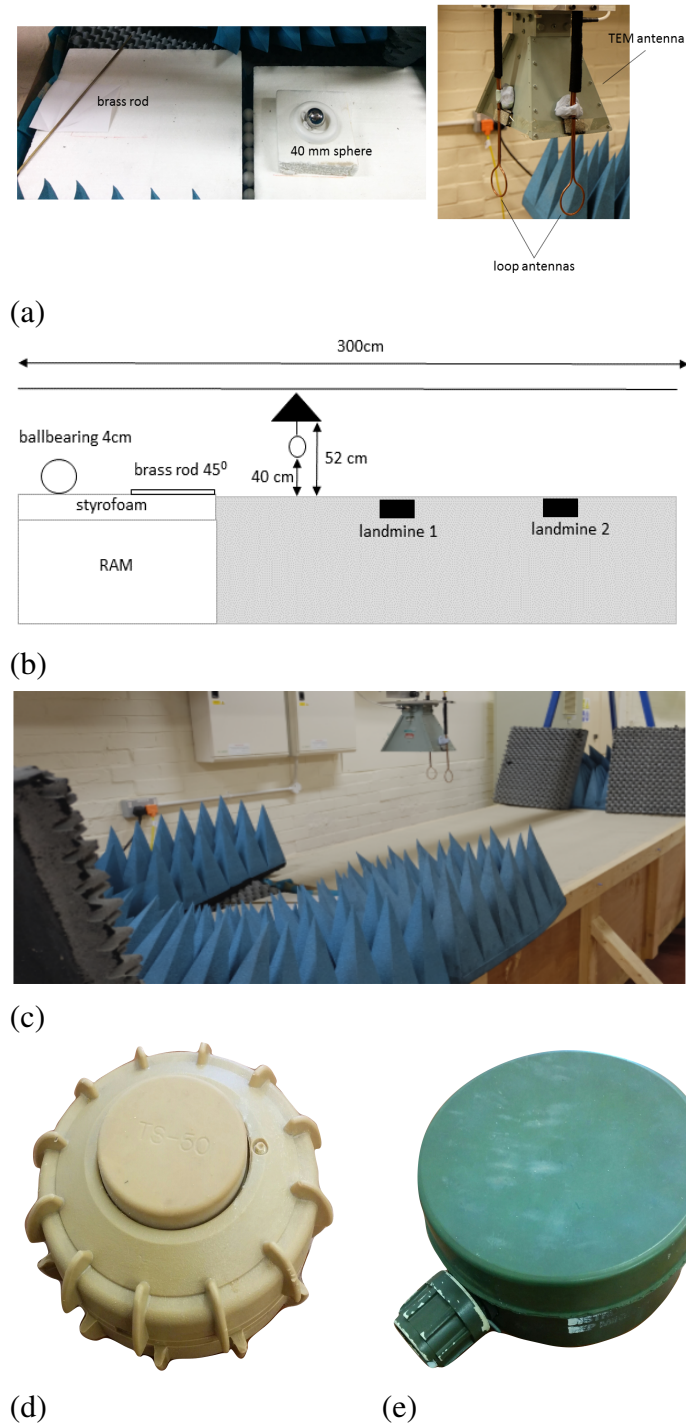


Figure 5.2: (a) Calibration targets and antenna head, (b) Sketch of measurement setup, (c) Laboratory scene (d) Landmine 1 is an Italian TS-50 landmine, (e) Landmine 2 is a Russian PMN-1 landmine.

5. ADVANCED POLARIMETRY FOR SUBSURFACE IMAGING

5.5.1.3 Channel Calibration

Since, receive and transmit antennas are different, the system is bistatic. Although, the radar polarimetry is derived from the monostatic case and the antennas are located very close to each other, calibration of the system is crucial [4]. The scattering matrix $S_{bistatic}$, equation (5.38), obtained by the measurement system is different from the one of the monostatic case. To accomodate and calibrate the phase to mimic the monostatic system response, we used an extrapolation method. Figure 5.3 shows the calibration scheme, viewed from the top of the antennas. The calibration object, in this case the rod, stays static at one position, as does the transmit antenna, and the receive antenna is moved N positions away from the rod. Measurements are taken in 1cm increments. In this case we moved the antenna head $N = 20$ positions. The plots for difference in phase and difference in amplitude for each polarisation at each position are shown in Figure 5.4. Calculation of the correction factor $\overline{\psi_{nm}}$ is shown in equations (5.39) and (5.40). The phase and amplitude, at each position $N > 1$ is subtracted from the phase or amplitude at position $N=1$ and the result plotted. The phases and amplitudes are extrapolated to position zero (i.e. ideal monostatic positions) and averaged. This is done for each polarisation and polarisation matrix is formed. Each pixel in each polarisation B-scan is multiplied with this correction factor.

$$S_{bistatic} = \begin{bmatrix} S_{VV} & S_{VH} \\ S_{HV} & S_{HH} \end{bmatrix} \quad (5.38)$$

$$\psi_{nm} = A_c(\cos(\Phi_c) + j\sin(\Phi_c)) \quad (5.39)$$

$$\overline{\psi_{nm}} = \left(\sum_{n=1}^N \psi_{nm} \right) / N \quad (5.40)$$

$$S_{monostatic} = \begin{bmatrix} S_{VV}\overline{\psi_{VV}} & S_{VH}\overline{\psi_{VH}} \\ S_{HV}\overline{\psi_{HV}} & S_{HH}\overline{\psi_{HH}} \end{bmatrix} \quad (5.41)$$

5. ADVANCED POLARIMETRY FOR SUBSURFACE IMAGING

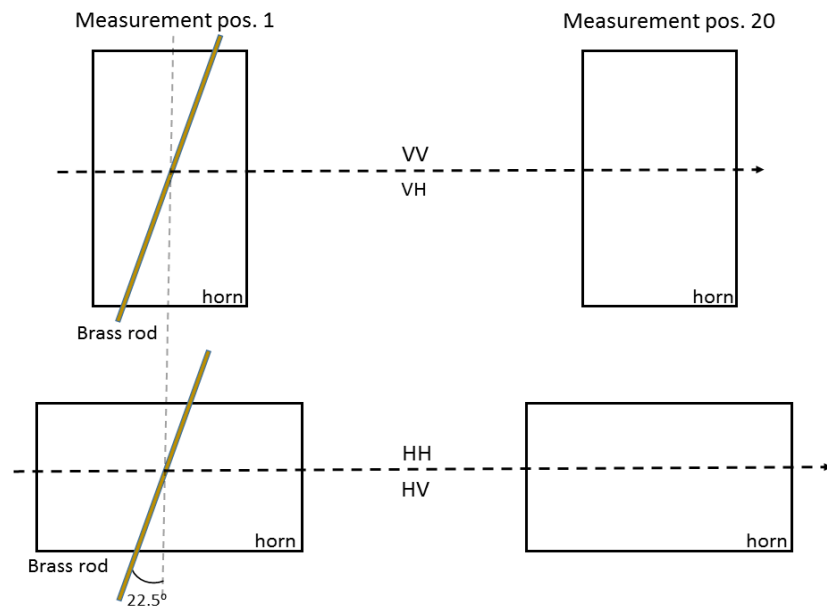


Figure 5.3: Schematic diagram illustrating the polarimetric correction calibration procedure, using a brass rod inclined on the horizontal at 22.5° .

The arrangement of these objects allows the system precise calibration to range. The resultant calibrated B-scans of the scene are shown in Figure 5.5 with the surface laid and subsurface targets indicated,

5. ADVANCED POLARIMETRY FOR SUBSURFACE IMAGING

Table 5.1: Polarimetric response of objects in the radar scene.

Type	Object	Response
Calibration	Sphere (40 mm)	Co-polar calibration target HH, VV provides equal response HV, VH provides no response
Calibration	Rod inclined on the horizontal at 22.5°	Cross-polar calibration target HH, VV provides no response HV, VH provides some response
Reference	Trihedral	Will return equally in both cross and co-polar
Target	PMN-2	Will provide some unknown response
Reference	Sphere	As for calibration sphere but use for reference

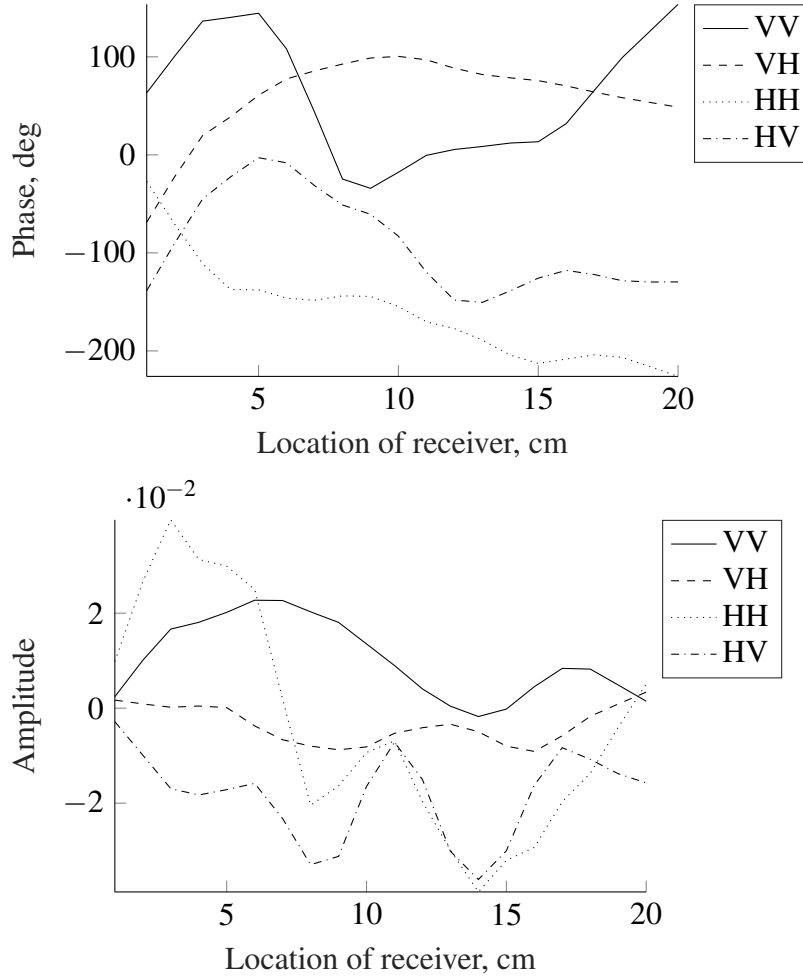


Figure 5.4: Difference in phase Φ_c and amplitude A_c of 20 increments away from calibration target

5. ADVANCED POLARIMETRY FOR SUBSURFACE IMAGING

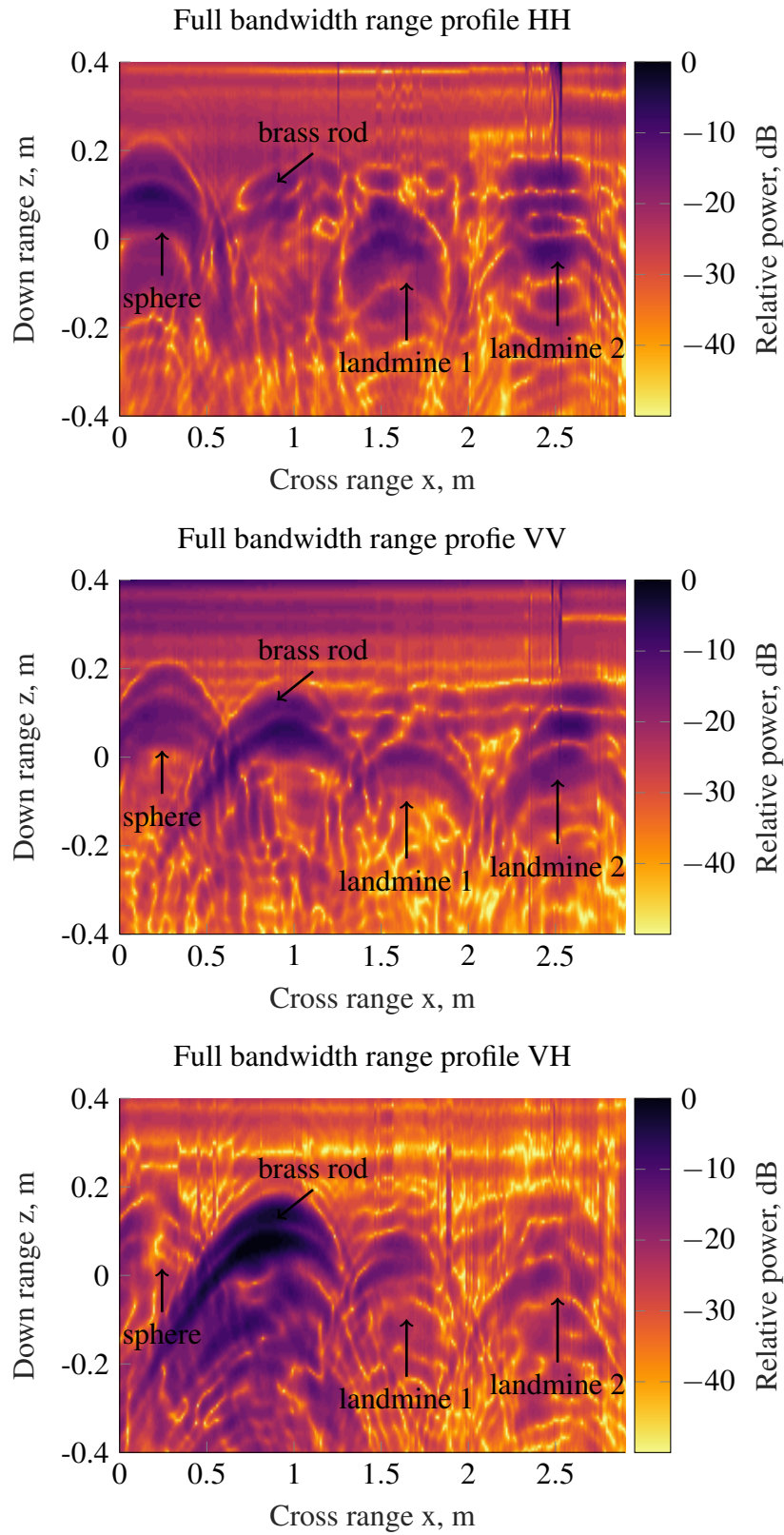


Figure 5.5: Calibrated low band B-scans, indicating a sphere (40 mm) and a brass rod as calibration targets as well as two landmines where landmine 1 is an Italian TS-50 landmine and landmine 2 is a Russian PMN-1 landmine.

5. ADVANCED POLARIMETRY FOR SUBSURFACE IMAGING

5.5.2 Experiment 5 B - High Band Configuration

5.5.2.1 System and Antennas

The stepped frequency radar system used in this is the same as in experiment A, except that here for the scans the antenna array with incorporated lenses, as designed in chapter 3 and 4, is deployed. The antenna array shown in Figure 5.6 implements two pairs of horizontally and vertically polarised antennas to achieve polarisation diversity and the figure inset depicts the antenna aperture orientation. The radar system is configured to sequentially measure the scattering parameter S_{21} across the X-band (8.2-12.4 GHz) frequency spectrum in all possible combinations available from the H- and V-antennas, i.e. H-transmitting and H-receiving and so forth). Then the FP scattering matrix (HH, HV, VH, HH) for a resolution element may be determined. The array is mounted 58 cm above the soil surface and acquires the scattering matrix in 1.0 cm measurement intervals. The measured S_{11} response for all the antennas in the array is $\leq -12\text{dB}$ and the measured co- and cross-polar mutual coupling in E- and H-planes is $\leq -35\text{dB}$ and $\leq -60\text{dB}$, respectively.

5.5.2.2 Experimental Setup

Experiments have been conducted on an indoor soil facility, shown in Figure 5.6, which consists of one soil bay (2.4Lx1.2Wx0.8H meters) filled with sand and an adjacent bay (1.2Lx1.2Wx0.8H meters) lined with RAM on which calibration targets can be placed. The soil is maintained within a 1-3% moisture content, which reflects a moisture level one would encounter in a desert area between the early morning hours and noon. Here dew in the early morning hours causes a slightly higher moisture level in the surface area (3%) than around noon (1%). Due to the ventilation system setup in the laboratory area all experiments were conducted at a constant temperature of 25°C . A Near-Field Measurement System (NFMS) has been erected over the two bays with a 3 m long linear automated positioner. As previ-

5. ADVANCED POLARIMETRY FOR SUBSURFACE IMAGING

ously mentioned in one soil bay several reference targets were placed above the surface of the sand resting on a 40 mm thick block of polystyrene foam and a bed of radar absorbent material (RAM). The foam layer permits more precise localisation of the reference targets scattered response. These included a 40 mm metal sphere for co-polar calibration and two 70 mm square sided dihedral reflectors with their seam rotated at an 22.5° angle perpendicular to the direction of antenna movement, for cross-polar calibration. In a second region two (70Lx70Wx9D cm) Perspex trays were laid on top of the sand and completely filled with sand. Under one Perspex tray another trihedral, 70 mm square sided, was buried at a depth of 230 mm from the surface of the filled tray. Under the second Perspex tray a TS-50 landmine diameter 60 mm and thickness 40 mm was buried at a depth of 160 mm from the surface of the filled tray to the top of the landmine. The sphere, the dihedrals and trihedral allow for GPR channel amplitude and phase correction.

5. ADVANCED POLARIMETRY FOR SUBSURFACE IMAGING

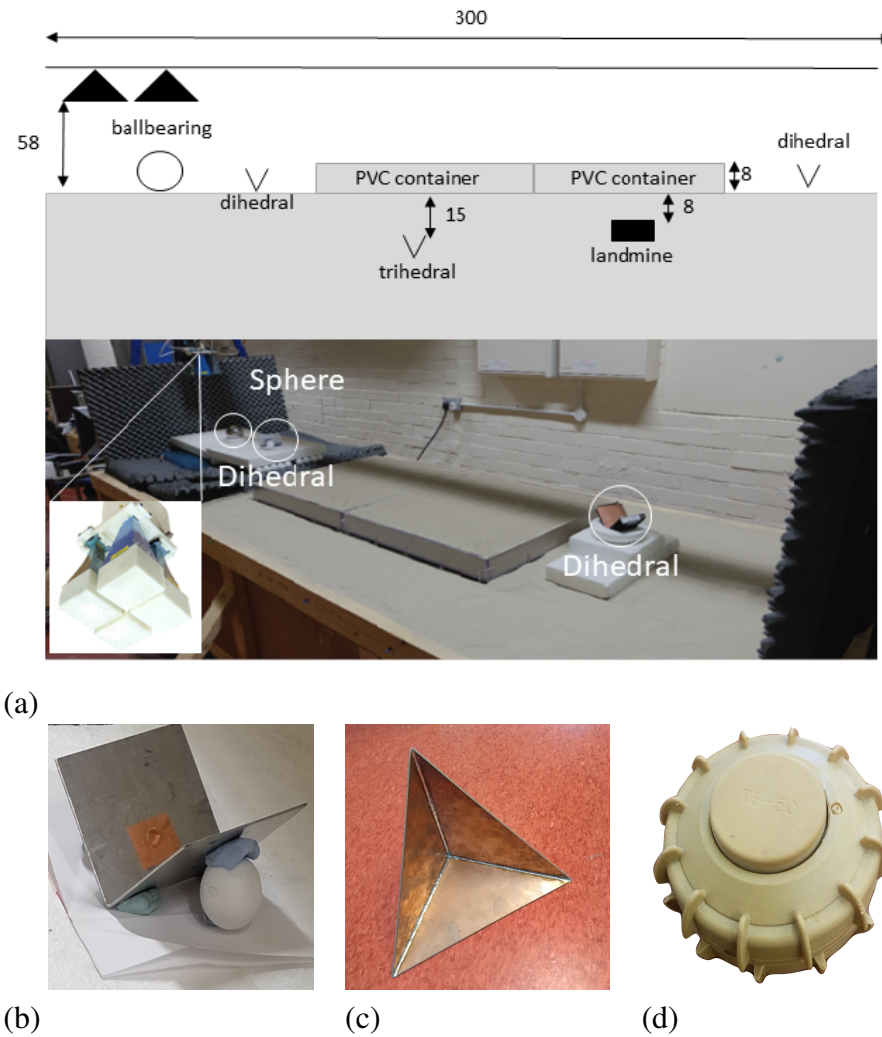


Figure 5.6: (a) Sketch of high band experimental setup and scene with calibration targets indicated, (b) Dihedral used in the scene, (c) Trihedral used in the scene, (d) TS-50 landmine used in the scene.

5. ADVANCED POLARIMETRY FOR SUBSURFACE IMAGING

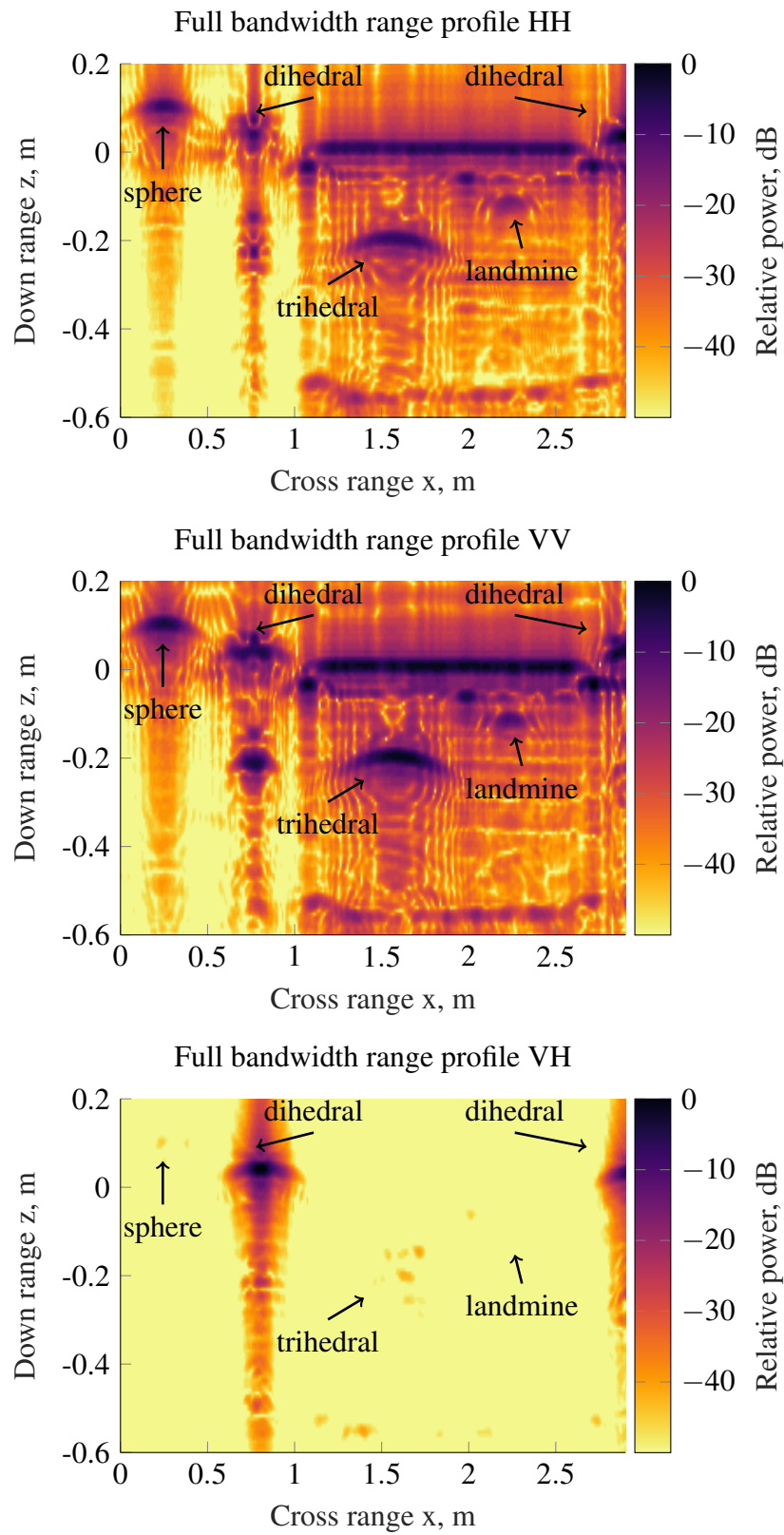


Figure 5.7: Calibrated high band B-scans.

5. ADVANCED POLARIMETRY FOR SUBSURFACE IMAGING

5.6 Discussion

In this section the results of the aforementioned mechanisms, namely Stokes parameters, Pauli decomposition and Yamaguchi decomposition, applied to the data gathered in Experiment 5 A (0.4-4.8 GHz) and Experiment 5 B (8.2-12.4 GHz) will be discussed. Due to the fact that we look for subsurface targets which might have different scattering parameters and might be made from different materials, it is deemed necessary to always apply multiple imaging algorithms on one set of data to reveal all targets in the scene.

5. ADVANCED POLARIMETRY FOR SUBSURFACE IMAGING

5.6.1 Experiment 5 A - Low Band Configuration

5.6.1.1 Stokes Parameters

When applying the Stokes parameters technique to the low-band data, the air-ground interface and subsurface clutter can be sufficiently suppressed in the co- and cross-polar case, as can be seen in Figure 5.8. All targets are focused in their place, although the brass rod is only resolved in the I_h case. It was found that this is due to the fact, that the styrofoam bed, the brass rod was placed on was slightly tilted and not aligned perpendicular to the antenna beam.

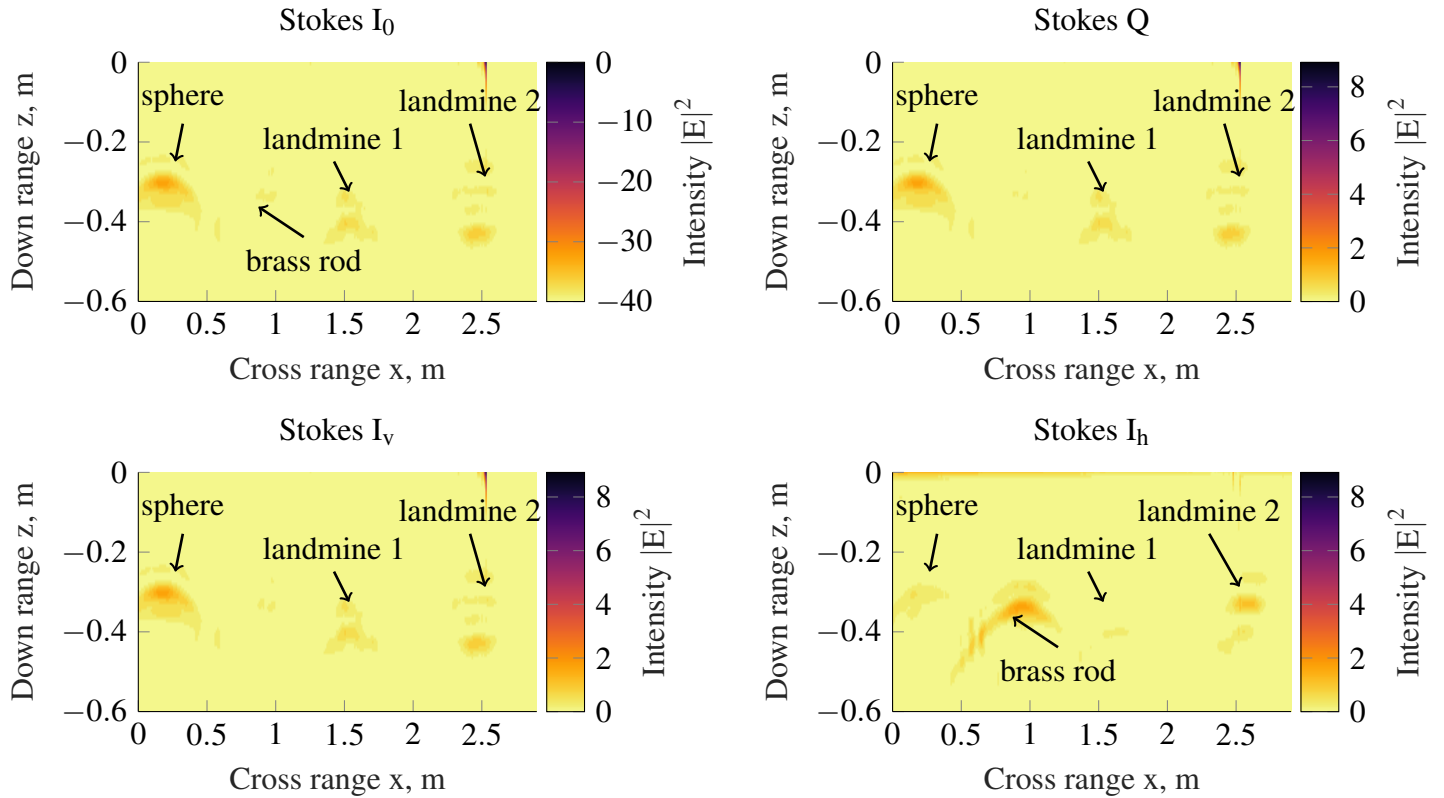


Figure 5.8: Top: Stokes parameters I_0 and Q , Bottom: I_v and I_h .

5. ADVANCED POLARIMETRY FOR SUBSURFACE IMAGING

5.6.1.2 Pauli Decomposition

In contrast to the Stokes parameters, in Figure 5.9 it can be seen, that applying the Pauli decomposition technique to the low-band does only slightly suppress the air-ground interface and subsurface clutter, but the antenna clutter remain in the resulted images. Nevertheless, the targets are pulled together in their place, but can not be resolved sufficiently.

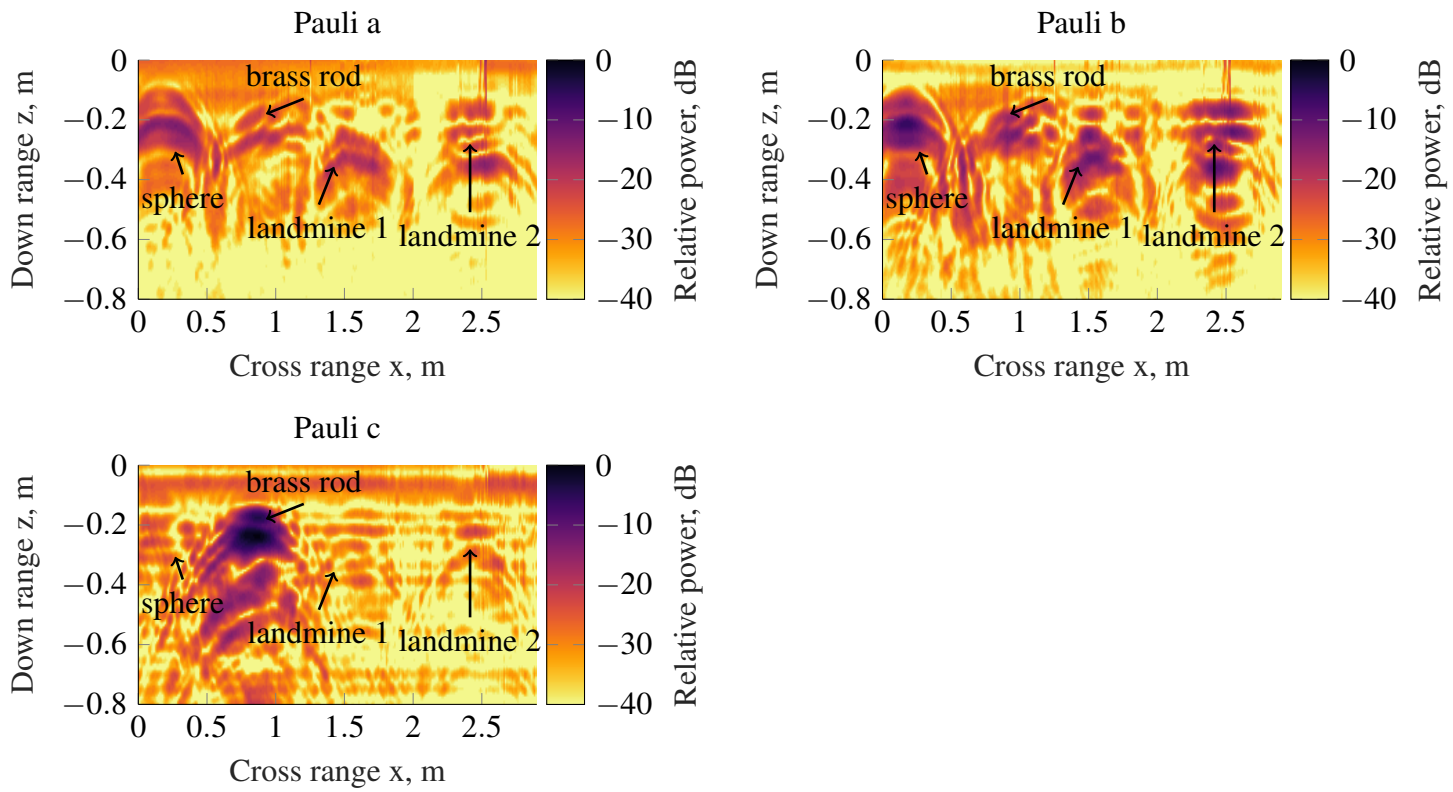


Figure 5.9: (a) Pauli a, (b) Pauli b, (e) Pauli c.

5. ADVANCED POLARIMETRY FOR SUBSURFACE IMAGING

5.6.1.3 Yamaguchi Decomposition

The Yamaguchi decomposition applied to the low-band data, as in Figure 5.10 sufficiently suppresses antenna clutter, air-ground interface and subsurface clutter in the co- and cross-polar case. All targets are pulled together in their place and can sufficiently be discriminated from each other.

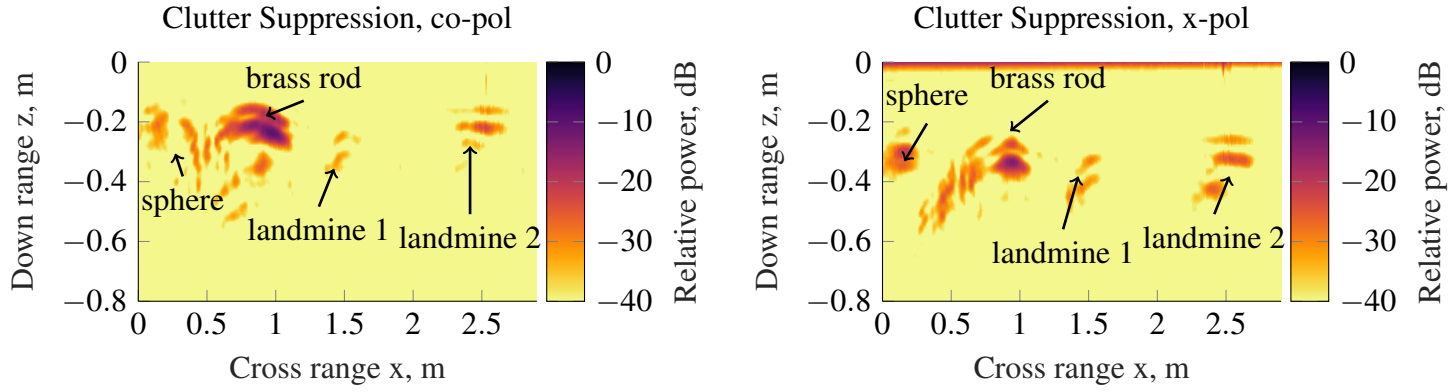


Figure 5.10: Co- and cross-polar polarimetric clutter suppression.

5. ADVANCED POLARIMETRY FOR SUBSURFACE IMAGING

5.6.2 Experiment 5 B - High Band Configuration

5.6.2.1 Stokes Parameters

When applying the Stokes parameters technique on the high-band data, it can be seen in Figure 5.11, that the air-ground interface, as well as, antenna and are almost completely suppressed, but the air-ground interface remains in the scene in the I_0 . Nothing of the scene remains in the I_Q . Here the buried landmine has a stronger response in the I_h case and is not resolved in the I_v case, at all.

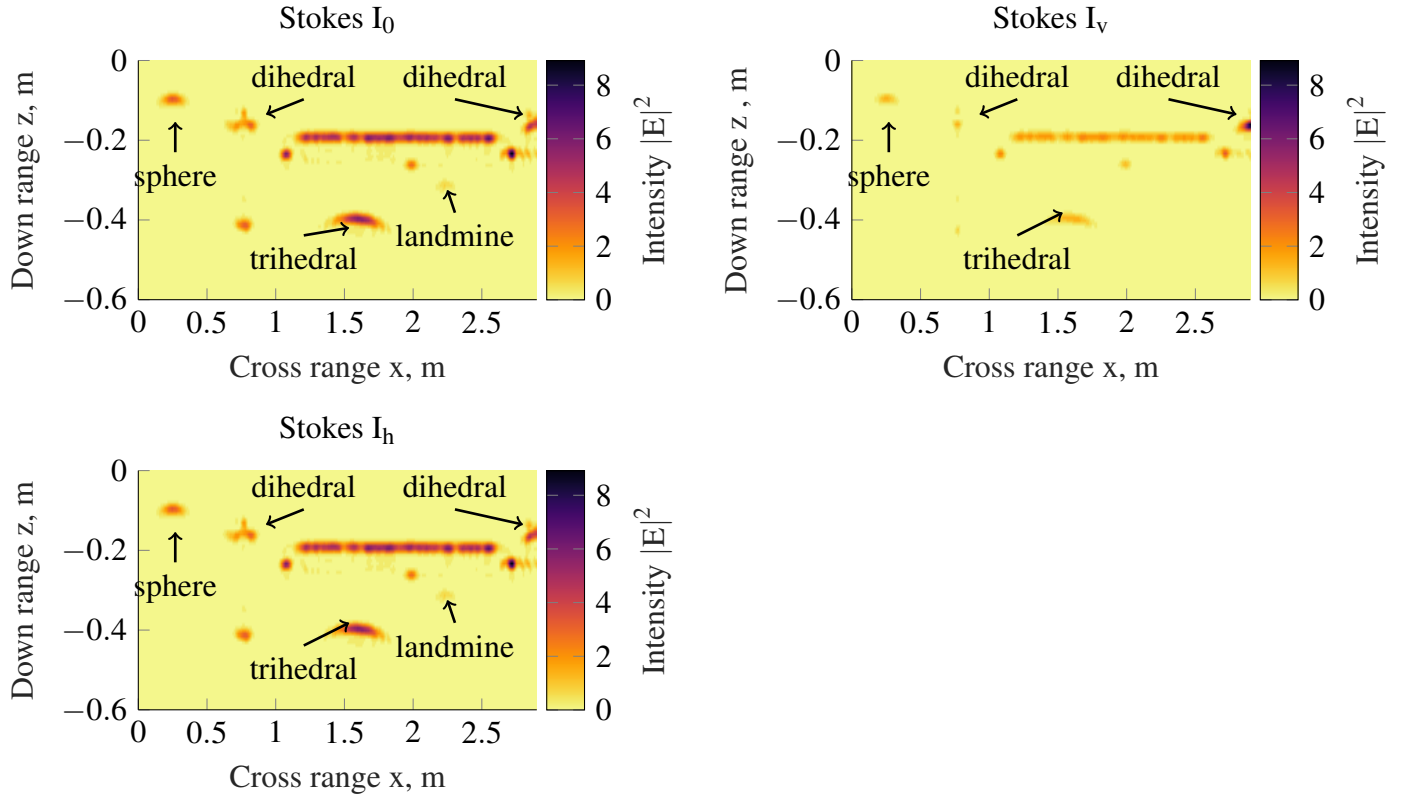


Figure 5.11: Top: Stokes parameters I_0 and Q , Bottom: I_v and I_h .

5. ADVANCED POLARIMETRY FOR SUBSURFACE IMAGING

5.6.2.2 Pauli Decomposition

Applying the Pauli decomposition technique to the high-band data, as in Figure 5.12, does slightly suppress the subsurface clutter, when compared to the initial raw B-scans, but does not suppress the air-ground interface. Nevertheless, targets are pulled together in their place for the Pauli a and Pauli b cases but except for the dihedrals in the scene, no other targets are visible in the Pauli c case.

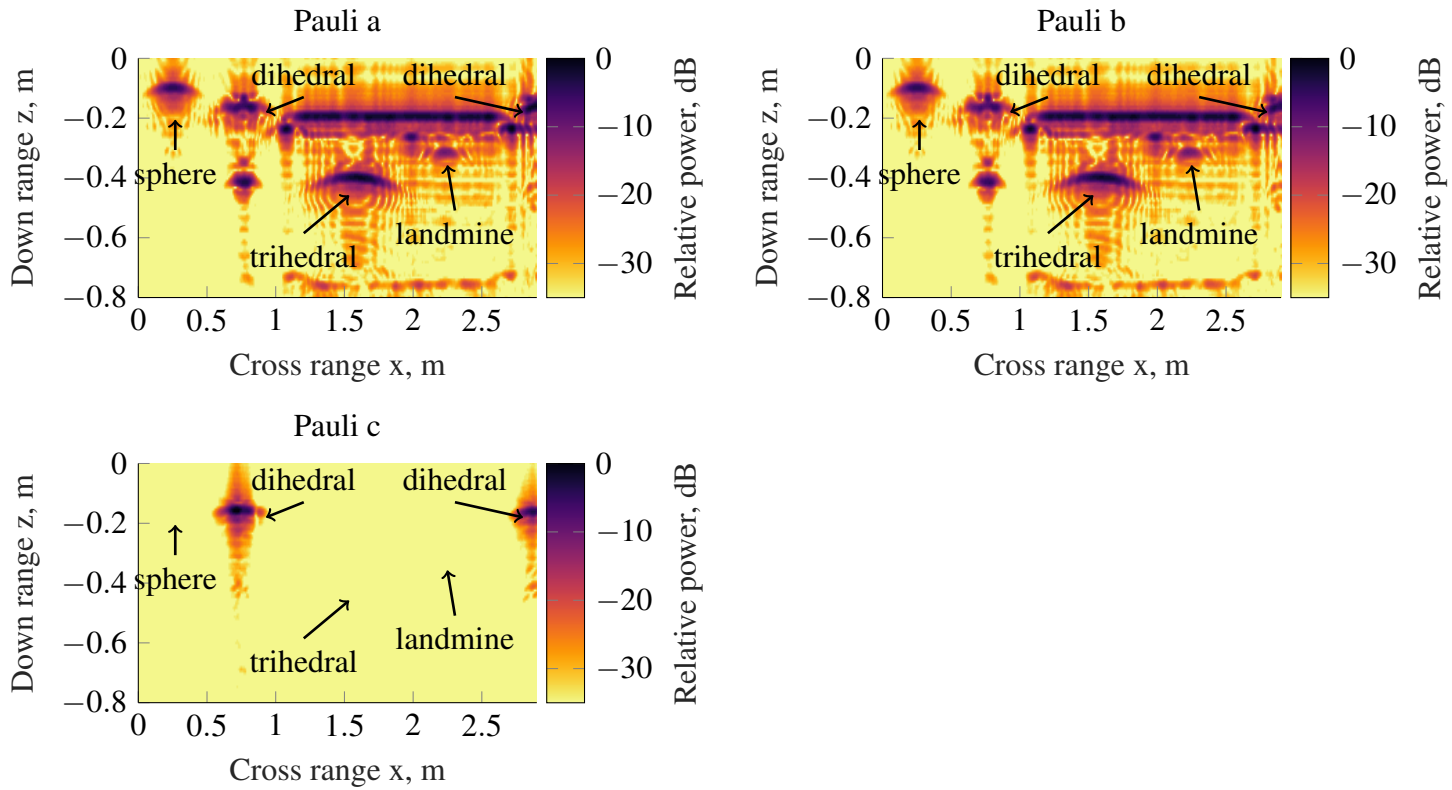


Figure 5.12: (a) Pauli a, (b) Pauli b, (e) Pauli c.

5. ADVANCED POLARIMETRY FOR SUBSURFACE IMAGING

5.6.2.3 Yamaguchi Decomposition

Applying the Yamaguchi decomposition technique to the high-band data, as seen in Figure 5.13, it can be shown, that the air-ground interface is not sufficiently suppressed for the cross-polar case and completely remains in the co-polar case. The targets are still pulled together in their place. The subsurface targets can can sufficiently be identified in the co-polar case but in the cross-polar case only be discriminated from surrounding subsurface clutter in hindsight.

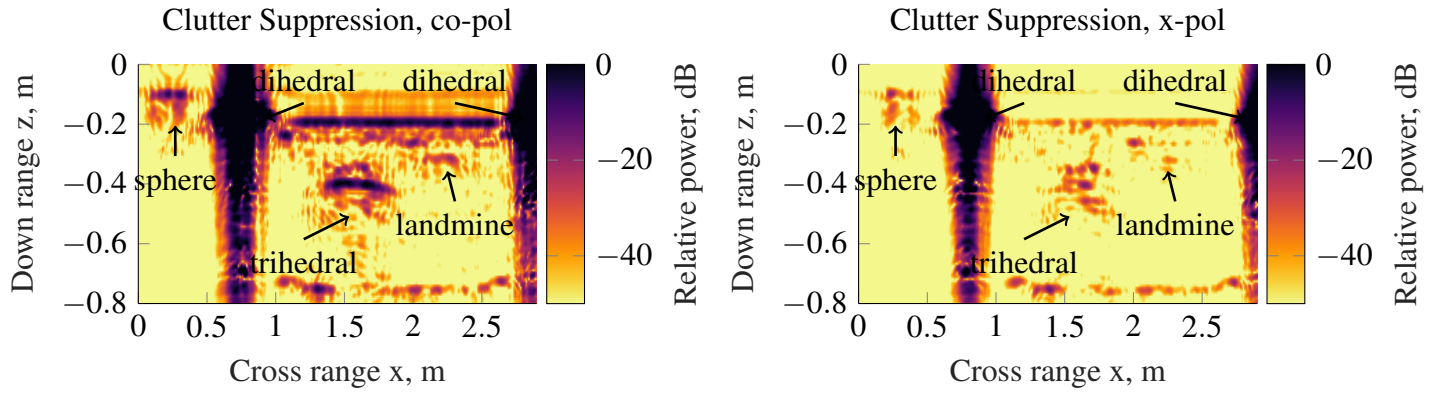


Figure 5.13: Co- and cross-polar polarimetric clutter suppression.

5. ADVANCED POLARIMETRY FOR SUBSURFACE IMAGING

5.7 Summary Comments

The full polarimetry data acquisition of the Jones scattering matrix has been exploited to provide power level clutter suppression. The mathematical formalism for the underlying physics of the scattering matrix was described and Stokes and Pauli formalisms introduced. The Yamaguchi decomposition was laid out to yield co-polar and cross-polar clutter filtered B-scan subsurface imagery. Two experimental set-ups for performing GPR measurements for low- and high-band and test signal-processing and imaging algorithms have been developed. This experimental set-ups compose one sand bay to bury targets and one bay filled with RAM to place calibration targets. Land-mines from different shapes and materials have been measured and channel balancing and novel bistatic calibration has been performed on the measured dataset. Various Stokes, Pauli and Yamaguchi polarimetric decompositions were performed and investigated on their capabilities to provide clutter suppression. It was shown, that the air-ground interface, as well as surface clutter, were most sufficiently suppressed in low-band using Stokes parameters and Yamaguchi decomposition. Whereas, using Pauli decomposition on the low-band data left the scene clutter without being able to properly distinguish subsurface targets. For the high-band data, none of the introduced imaging formalisms suppressed the air-ground interface, but in all cases the subsurface clutter was significantly reduced. For the high-band data the best target discrimination capabilities were provided by using the Pauli decomposition. The results of this chapter, make it clear, that it is necessary to always apply multiple imaging algorithms on one set of data to reveal all targets in the scene. The contribution of this chapter is, that for the first time these imaging formalisms have been applied to subsurface datasets of different bandwidths and their performance compared. The differing results in suppression capabilities for different bandwidths show that it is paramount to analyse gathered subsurface data with different imaging formalisms to make sure all targets can be resolved and no subsurface target is overlooked.

5. ADVANCED POLARIMETRY FOR SUBSURFACE IMAGING

References

- [1] F. T. Ulaby, in *Radar Polarimetry for Geoscience Applications*. Artec House, 1990, ch. chapter. 5.
- [2] B. Qian, T. Zeng, Z. Chen, and J. Ding, “Generation of vector beams using a wollaston prism and a spatial light modulator,” *Optik - International Journal for Light and Electron Optics*, vol. 148, 09 2017.
- [3] R. A. S. Rosa, D. Fernandes, T. L. M. Barreto, C. Wimmer, and J. B. Nogueira, “Change detection under the forest in multitemporal full-polarimetric p-band sar images using pauli decomposition,” in *2016 IEEE International Geoscience and Remote Sensing Symposium (IGARSS)*, 2016, pp. 6213–6216.
- [4] Y. Yamaguchi, T. Nishikawa, M. Sengoku, and W.-M. Boerner, “Fundamental study on synthetic aperture fm-cw radar polarimetry,” *IEICE Transactions on Communications*, vol. E77-B, no. 1, Jan 1994.
- [5] T. Moriyama, H. Kasahara, Y. Yamaguchi, and H. Yamada, “Advanced polarimetric subsurface fm-cw radar,” *IEEE Transactions on Geoscience and Remote Sensing*, vol. 36, no. 3, pp. 725–731, 1998.
- [6] Y. Yamaguchi, T. Moriyama, M. Ishido, and H. Yamada, “Four-component scattering model for polarimetric sar image decomposition,” *IEEE Transactions on Geoscience and Remote Sensing*, vol. 43, no. 8, pp. 1699–1706, 2005.
- [7] W. . Boerner, M. El-Arini, Chung-Yee Chan, and P. Mastoris, “Polarization dependence in electromagnetic inverse problems,” *IEEE Transactions on Antennas and Propagation*, vol. 29, no. 2, pp. 262–271, 1981.

Chapter 6

Temporal Imaging for Ground Penetrating Radar

6.1 Introduction

In the previous chapters a high-resolution ground penetrating radar system for subsurface imaging has been designed and its capabilities proven in practice. In general, ground penetrating radar systems require particular knowledge of the monostatic, bistatic or multi-static antenna properties and geometric set-up to spatially isolate vertically the backscattered signals from the surface and subsurface. One way to improve the cross range resolution is to use synthetic aperture processing (SAR)[1], which again requires *a priori* knowledge of the measurement setup. This chapter presents a novel microwave imaging technique that offers alternative subsurface imaging capabilities. The advantage of the presented technique is, that it does not rely upon a knowledge of the measurement setup or deploying clutter suppression techniques [2]. The principle mechanism exploits naturally occurring changes in soil moisture level to affect a change in the dielectric properties of the subsurface medium. Isolating changes in electrical phase of subsurface features, from those that do not, presents the possi-

6. TEMPORAL IMAGING FOR GROUND PENETRATING RADAR

bility to effectively separate buried targets from the background scene. A disadvantage of the scheme is the requirement for repeated measurement over relatively long periods of time.

The measurement of soil moisture levels with radar has previously been examined by *Benedetto et al.* [3, 4, 5] as has the determination of the relative permittivity of soil-water mixtures at microwaves frequencies by *Hallikainen et al.* [6]. More recently, *Edwards-Smith et al.* have reported the use of soil moisture change to provide virtual bandwidth synthetic aperture radar imagery [7]. Underpinning these techniques is the need for a soil model that adequately predicts the changes in complex relative permittivity and observed effects at frequencies from 1.4-20 GHz.

The chapter shows a study of the polarimetric spatial changes measured in multi-temporal data. The highly accurate Dobson soil model is adapted to precisely predict the complex dielectric changes taking place in the soil as the soil moisture changes. Two sets of experimental data is used to cumulatively observe and plot these microwave electrical phase changes taking place as the soil moisture level change around a buried landmine. The Dobson model confirms the phase changes and a novel sub-wavelength cumulative phase change imaging product is derived that proves to be very effective at reducing the surface and sub-surface clutter levels. Further to that a novel differential interferometric polarimetry technique is presented. This DinPol technique utilises phase changes between two polarimetry states and its capabilities to discriminate objects in the subsurface are examined. The two techniques compare favourably with the results obtained in Chapter 5 and provides a complementary imaging tool to examine the subsurface.

6. TEMPORAL IMAGING FOR GROUND PENETRATING RADAR

6.2 The Dobson Four Component model

In assessing the soils and soil mixtures used in the following experiments we make use of the Dobson [6] dielectric mixing model to make reliable prediction of the dielectric behaviour of wet soil. A four component dielectric mixing model treats the soil-water system as a host medium of dry soil containing randomly distributed disc shaped inclusions of bound water, bulk water and air. The relative permittivity of the mixture ϵ_m can be written [6].

$$\epsilon_m = \frac{3\epsilon_s + 2V_{fw}(\epsilon_{fw} - \epsilon_s) + 2V_{bw}(\epsilon_{bw} - \epsilon_s) + 2V_a(\epsilon_a - \epsilon_s)}{3 + V_{fw}(\epsilon_s/\epsilon_{fw} - 1) + V_{bw}(\epsilon_s/\epsilon_{bw} - 1) + V_a(\epsilon_s/\epsilon_a - 1)} \quad (6.1)$$

where the subscripts bw , fw , a , and s refer to bound water, free water, air and soil. Volume fractions for each component are calculated for each soil at a given volume water content and bulk density of the soil; $\epsilon_a = 1.0004$ and ϵ_s is determined from the empirical fit to the measured data presented in [8]. ϵ_{fw} is derived from a Debye type relaxation that accounts for ionic conductivity losses as,

$$\epsilon'_{fw} = \epsilon_{w\infty} + \frac{\epsilon_{w0} - \epsilon_{w\infty}}{1 + (2\pi f \tau_w)^2} \quad (6.2)$$

and

$$\epsilon''_{fw} = \frac{2\pi f \tau_w (\epsilon_{w0} - \epsilon_{w\infty})}{1 + (2\pi f \tau_w)^2} + \frac{\sigma_{m_v}}{2\pi \epsilon_0 f}. \quad (6.3)$$

ϵ_{w0} is the static dielectric constant of water, $\epsilon_{w\infty} = 4.49$ is the high frequency limit and ϵ_0 has its normal value. σ_{m_v} is the effective conductivity of the volume of bound water and τ_w is the relaxation time of pure water and given by,

$$\begin{aligned} 2\pi \tau_w(T) = & 1.1109 \times 10^{-10} - 3.824 \times 10^{-12}T \\ & + 6.938 \times 10^{-14}T^2 - 5.096 \times 10^{-16}T^3 \end{aligned} \quad (6.4)$$

where T is in $^{\circ}\text{C}$. This expression was determined by Stogryn [9] via polynomial fit to experimental data. An equivalent term cited is the relaxation frequency $f_o = (2\pi \tau_w)^{-1}$, which

6. TEMPORAL IMAGING FOR GROUND PENETRATING RADAR

for water in the microwave region $f_0(0^\circ C) \approx 8.9$ GHz and $f_0(20^\circ C) \approx 16.7$ GHz.

In Figure 6.1 the complex relative permittivity, ϵ_m , is calculated using (6.1)-(6.4) over the 1.4-20GHz range of validity for the model. It is apparent that for a given frequency and temperature the complex dielectric constant value change with moisture is due principally to the real part.

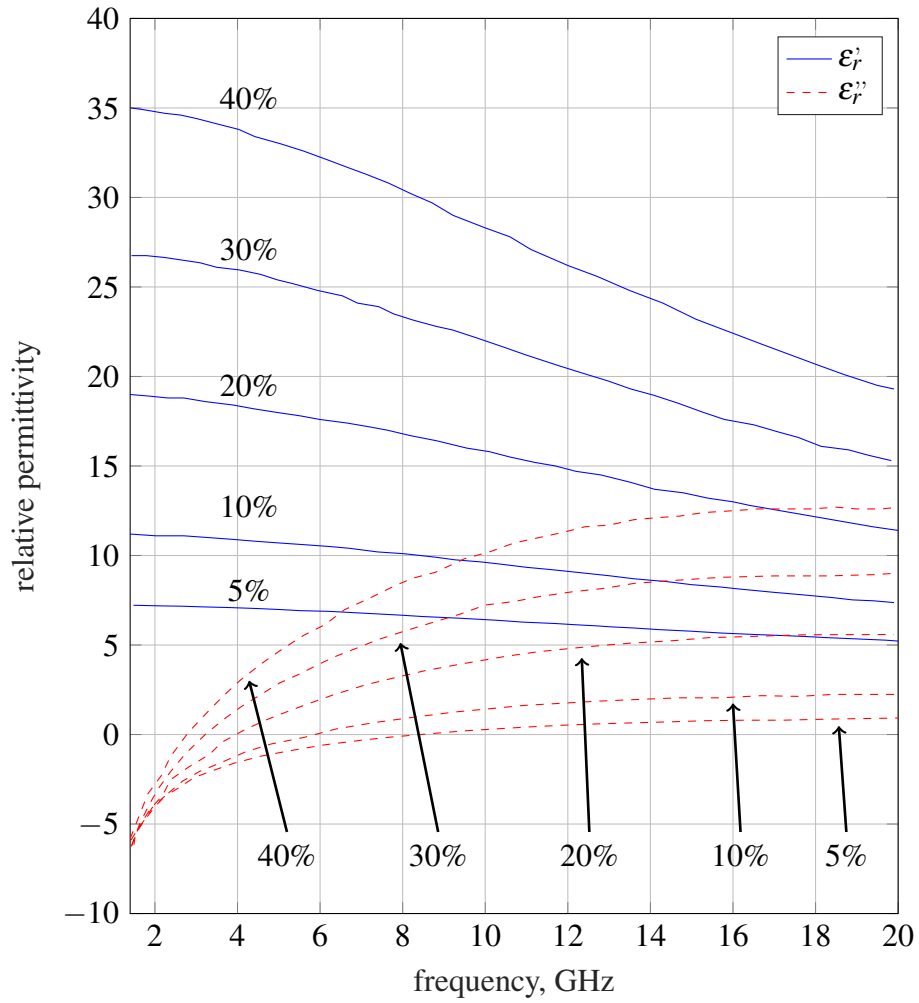


Figure 6.1: Computed complex dielectric constant for a range of moisture levels for sandy soil (% by volume water at 21.5°C).

6. TEMPORAL IMAGING FOR GROUND PENETRATING RADAR

6.3 Experiment 6 C - High Band Moisture Change Detection

6.3.0.1 System and Antennas

The stepped frequency radar system used in this is the same as in experiment 5 B. The antenna array shown in Figure 6.2 implements two pairs of horizontally and vertically polarised antennas to achieve polarisation diversity and the figure inset depicts the antenna aperture orientation. The radar system is configured to sequentially measure the scattering parameter S_{21} across the X-band (8.2-12.4GHz) frequency spectrum in all possible combinations available from the H- and V-antennas, i.e. H-transmitting and H-receiving and so forth). Then the FP scattering matrix (HH, HV, VH, HH) for a resolution element may be determined. The array is mounted 58 cm above the soil surface and acquires the scattering matrix in 1.0cm measurement intervals. The measured S_{11} response for all the antennas in the array is $\leq -12\text{dB}$ and the measured co- and cross-polar mutual coupling in E- and H-planes is $\leq -35\text{dB}$ and $\leq -60\text{dB}$, respectively.

6.3.1 Experimental Setup

The microwave measurement facility consisted of a sand bay 3 m (l) x 1.2 m (w) x 0.8 m (d). A 3.0 m linear actuator was located centrally along the length of the bay and used to scan four pyramidal horn antennas arranged in a polarimetry array. The antenna array is mounted 0.58 m above the soil surface and a Vector Network Analyser (VNA) used to collect X-Band (8.0-12.0 GHz) S-parameter measurements. Measurements are collected in 1.0 cm increments along the length of the scan and both actuator and VNA are under computer control. Measurements of VV, VH, HH, HV polarisations are made, using a bandwidth of 4.0 GHz. Figure 6.2 shows a view of the measurement setup. The sand bay was filled with kiln dried 100% by volume sand and the surface was levelled. To control and monitor the sand wetting procedure two Perspex trays with the inner dimensions 0.7 m (l) x 0.7 m (w)

6. TEMPORAL IMAGING FOR GROUND PENETRATING RADAR

x 0.07 m (h) were constructed and placed on the surface of the sand bay. The moisture was restricted to the trays alone.

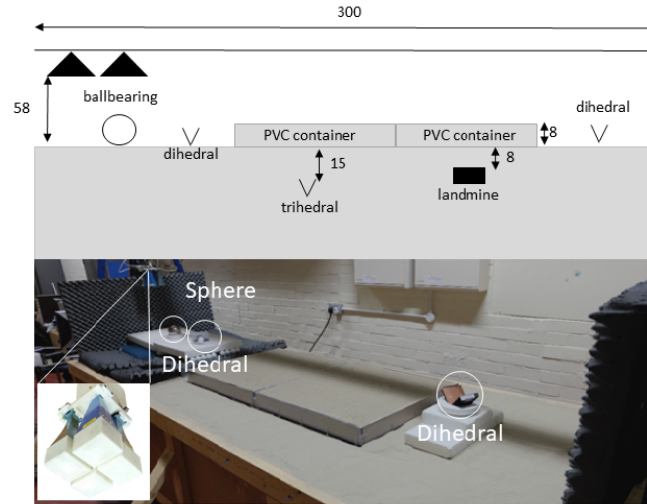


Figure 6.2: Schematic diagram and photo showing a view of the experimental radar scene (units in cm).

Several reference targets were placed above the surface of the sand on a bed of radar absorbent material (RAM) or support on polystyrene foam. These include a 40 mm metal sphere and two 70 mm square sided dihedral reflectors. Under the first Perspex tray a trihedral of 70 mm square sided was buried at a depth of 230 mm from the surface of the filled tray. Under the second Perspex tray a TS-50 landmine of diameter of 60 mm and thickness 40 mm was buried at a depth of 160 mm from the surface of the filled tray to the top of the landmine. The Perspex has a thickness of 10 mm, thus the outer depth of the tray is 80 mm. The sphere, dihedral and trihedral allow for GPR channel amplitude and phase correction.

6. TEMPORAL IMAGING FOR GROUND PENETRATING RADAR

6.3.2 Methodology

An initial control microwave scan and B-scan image was carried out with the soil dry.

The wetting phase:

- Deionised water in 3% by volume of the tray (or equivalently 0.35L) was incrementally added to the Perspex tray.
- Three titrations were applied in one hour intervals.
- A Delta moisture meter was used to take reading of moisture after each titration.
- A measurement B-scan was then taken of the radar scene.

Following immediately on the drying phase:

- Every three hours a microwave B-scan measurement was made of the radar scene.
- Everyday a Delta moisture meter was used to take a reading of moisture level and the temperature was recorded.
- Microwave measurements were continued for 5-days and a total of 53 scans were acquired.

When soil moisture levels in the Perspex trays had fallen to near zero the experiment was stopped. This collected data formed the basis of the analysis.

6. TEMPORAL IMAGING FOR GROUND PENETRATING RADAR

6.4 Analysis

6.4.1 Data Collection

The gathered range profiles were collected into a data cube as shown in Figure 6.3. The cube holds the down-range (z), the cross range scan position (x) and the number of time lapsed rescans ($nscan$) for one polarisation. A total of four data cubes are required to represent all the polarisations measured. A typical B-scan image contained in the data cube is shown in Figure 6.4. The surface laid and buried targets are all clearly visible.

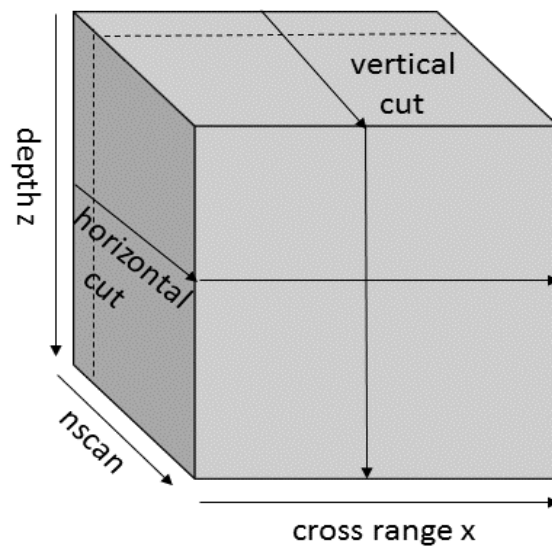


Figure 6.3: Structure of data stored in each polarimetry data cube.

6. TEMPORAL IMAGING FOR GROUND PENETRATING RADAR

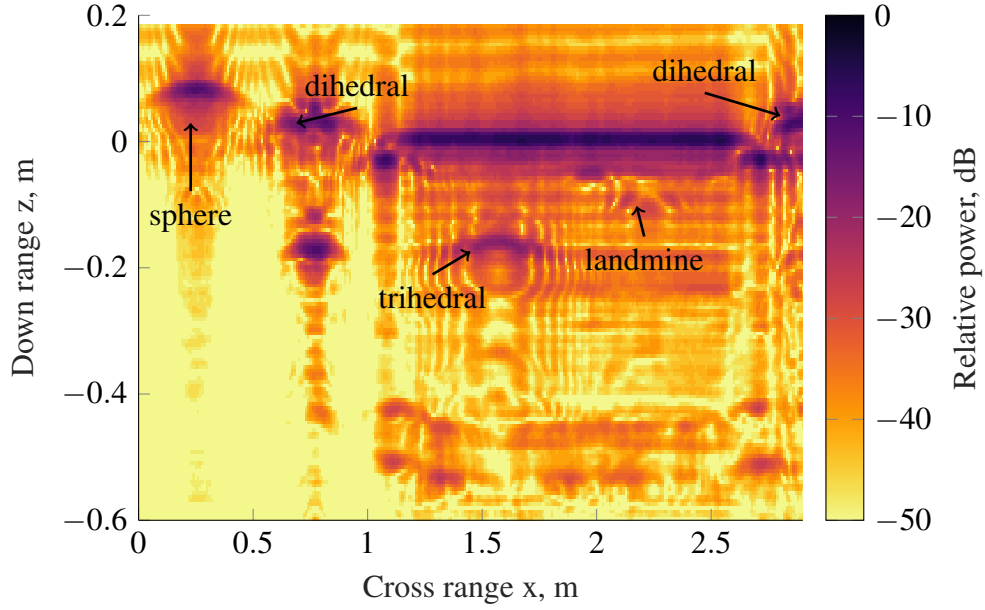


Figure 6.4: B-scan image of the radar scene, indicating a sphere (40 mm), two dihedrals (70 mm), a trihedral and a TS-50 landmine.

6.4.2 Moisture Change Detection

A simple expression for predicting of the total phase change due to the change in relative permittivity ϵ over the time lapsed series of collected B-scans images may be given as.

$$\Delta\Phi = \frac{4\pi}{\lambda} D (\sqrt{|\epsilon_m(wet)|} - \sqrt{|\epsilon_m(dry)|}) \quad (6.5)$$

with D being the depth of the target, $\epsilon_m(wet)$ the (“wet”) relative dielectric constant and $\epsilon_m(dry)$ the (“dry”) dielectric constant. Substituting the values calculated from the Dobson model at 10.0 GHz, plotted in Figure 6.1, corresponds to a predicted phase change of 383.75° electrical degrees. Since the moisture level was not allowed to rise above 3%, the Dobson model’s dataset only allows a quantitative prediction of the absolute phase change with frequency. If the moisture level is allowed to rise above 3%, up to a maximum of 60%, then the Dobson model would allow prediction of phase change over a range of permittivities at a fixed frequency. It is remarked that in initial experiments it was found, that a moisture level of

6. TEMPORAL IMAGING FOR GROUND PENETRATING RADAR

around 10% causes percolation and the water cannot be distributed evenly over the surface. The maximum of 3% moisture level was chosen, as this is the realistic moisture level one might find in a desert environment during early morning hours, due to dew.

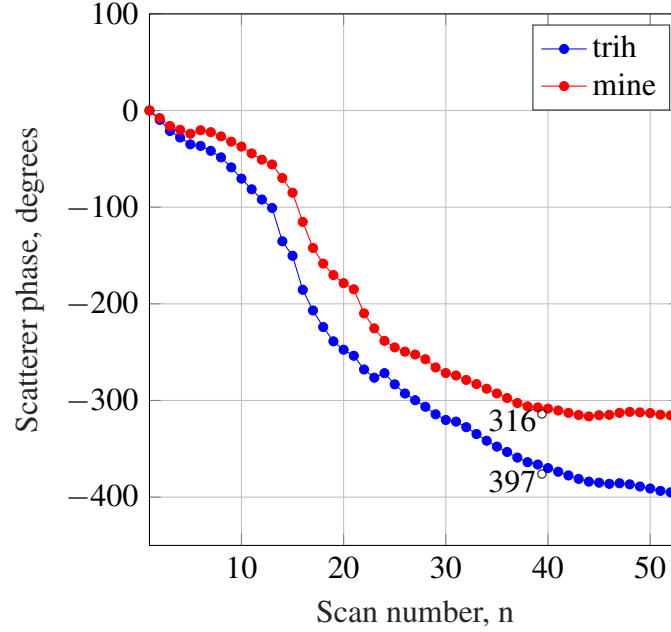


Figure 6.5: Observed experimental phase change of the trihedral and TS-50 landmine over all time lapsed scans.

Experimentally, the phase change can be extracted from the datacube by monitoring the electrical phase in the B-scan at the pixel cells for the trihedral and TS-50 land-mine. Figure 6.5 plots the phase history of these pixels over all the time lapsed scans. A measured phase change of 397° over the trihedral and 316° over the TS-50 land-mine was observed and these results are in close agreement with our soil model prediction of 383.75° . If we take a Fast Fourier transform in the vertical or horizontal cut of the data cube, depicted in Figure 6.3, at the location of either the trihedral or the TS-50 landmine the resulting range profile demonstrates that the objects appear shifted down range by one range bin and is due to the relative permittivity change in the medium.

6. TEMPORAL IMAGING FOR GROUND PENETRATING RADAR

6.4.3 Phase Weighted Imagery

It is evident from Figure 6.4 that significant clutter is present in the subsurface radar scene. A novel technique was postulated to provide image clutter suppression. It was observed from plots of B-scan phase imagery that the phase changed only around buried objects as the soil dried and this was anticipated. An image based algorithm was formulated around this hypothesis and is given as;

$$P(x,y) = \sum_{n=1}^{nscan} \Delta\phi(x,y)_n \cdot |p(x,y)_n|^\alpha \quad (6.6)$$

where,

$$\Delta\phi(x,y)_n = \angle \left(\frac{p(x,y)_{n+1}}{|p(x,y)_{n+1}|} \right) \cdot \frac{|p(x,y)_n|}{p(x,y)_n} \quad (6.7)$$

where the summed $P(x,y)$ pixel is the magnitude weighted differential phase contrast of the complex valued $p(x,y)$ pixel at position (x,y) of the individual B-scan that compose the n scans. The exponent α is either 1 for magnitude or 2 for intensity of the electric field, depending on the image format required.

The resultant image is shown in Figure 6.6 and it can be seen that stationary phase artefacts are mostly removed from the scene and those that change phase in a constant direction and have a scatterer present are retained. Hence the air-surface interface is almost completely suppressed and mostly only the buried targets, the trihedral and TS-50 landmine, are retained in the image.

6. TEMPORAL IMAGING FOR GROUND PENETRATING RADAR

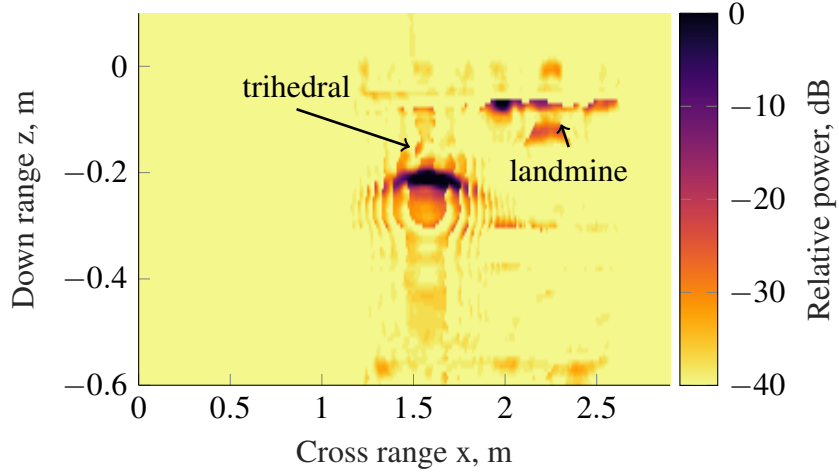


Figure 6.6: Summed magnitude weighted differential phase contrast B-scan ($\alpha = 1$).

6.5 Differential Interferometric Polarimetry

Differential Interferometric Polarimetry (DinPol) is a different imaging technique derived from the temporal imaging capabilities of the aforementioned derived moisture change detection. It takes advantage of phase changes between two polarimetry states in this case HH and VV. Equations (6.8) and (6.9) illustrate the technique.

$$P(x, y) = \sum_{n=1}^{pol_{state}} \Delta\phi(x, y)_n \cdot |p(x, y)_n| \quad (6.8)$$

where,

$$\Delta\phi(x, y)_n = \angle \left(\frac{p(x, y)_{n+1}}{|p(x, y)_{n+1}|} \cdot \frac{|p(x, y)_n|}{p(x, y)_n} \right) \quad (6.9)$$

where the summed $P(x, y)$ pixel is the magnitude weighted differential phase contrast of the complex valued $p(x, y)$ pixel at position (x, y) of the individual B-scans that compose either co- or cross-polar images.

The resultant images are shown in Figure 6.7 for co-polar (VV, HH) and cross-polar (VH, HV) DinPol. Compared to the results from chapter 5, the images retain all the polarimetric scattering mechanism while suppressing random clutter. Hence the DinPol co-polar almost

6. TEMPORAL IMAGING FOR GROUND PENETRATING RADAR

completely suppressed the air-ground interface and retains targets with single or odd bounce scattering features; on the other hand, the DinPol cross-polar retains only objects with diplane scattering with relative orientation of 45° . It was anticipated that no subsurface objects would be present, however, a partial scatter from the brass rod calibration object is present. This was found experimentally to originate from a slight dip on the brass rod in the horizontal plane.

6. TEMPORAL IMAGING FOR GROUND PENETRATING RADAR

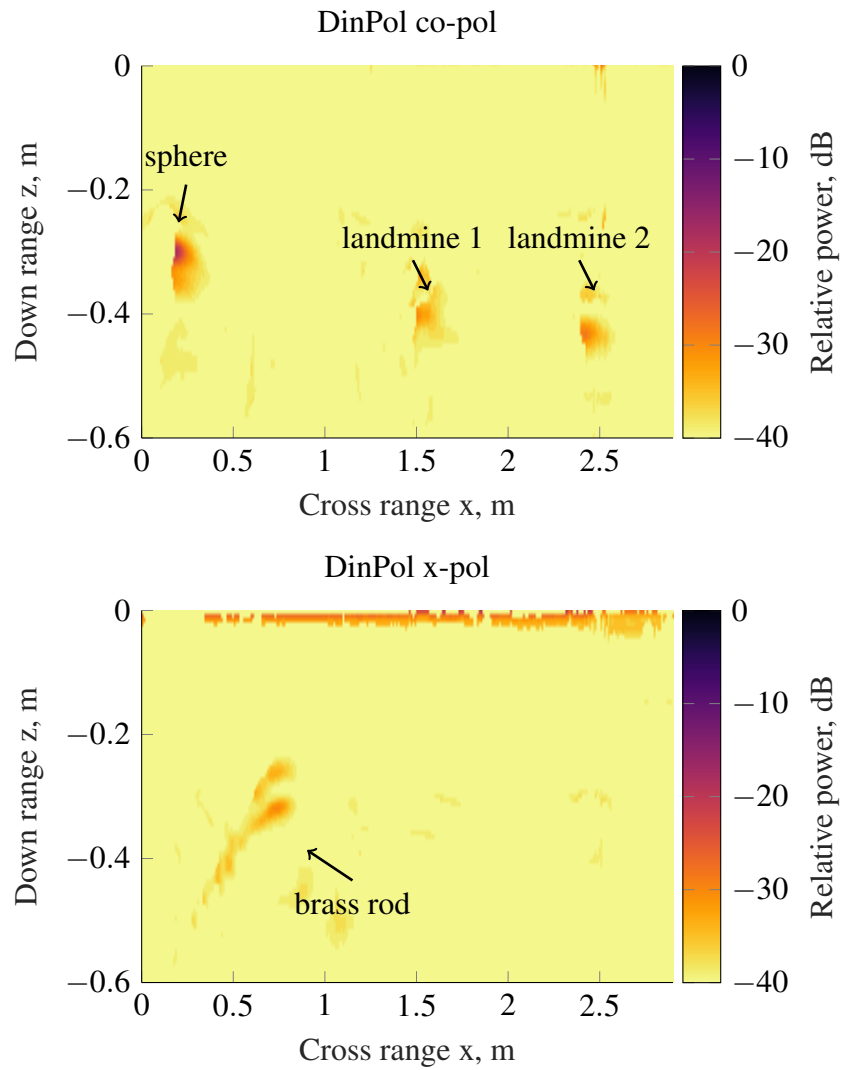


Figure 6.7: Co- and cross-polar DinPol results, indicating a sphere (40 mm) and a brass rod as calibration targets as well as two landmines where landmine 1 is an Italian TS-50 landmine and landmine 2 is a Russian PMN-1 landmine.

6. TEMPORAL IMAGING FOR GROUND PENETRATING RADAR

6.6 Summary Comments

In this chapter the highly accurate Dobson soil model was adapted to precisely predict the complex dielectric changes taking place in the soil as the soil moisture changes. Two sets of experimental data was used to cumulatively observe and plot these microwave electrical phase changes taking place as the soil moisture level change around a buried landmine. The Dobson model confirmed the phase changes and a novel sub-wavelength cumulative phase change imaging product was derived that proves to be very effective at reducing the surface and sub-surface clutter levels, as is is capable to reduce surface clutter significantly and to almost completely suppress subsurface clutter. Further to that a novel differential interferometric polarimetry technique was presented. This DinPol technique utilises phase changes between two polarimetry states and its capabilities to discriminate objects in the subsurface were examined. It was shown that surface and subsurface clutter were suppressed and the placed targets were clearly distinguishable.

6. TEMPORAL IMAGING FOR GROUND PENETRATING RADAR

References

- [1] C. Jackowatz, “Spotlight-mode synthetic aperture radar: A signal processing approach,” 1996.
- [2] D. Daniels, “Ground penetrating radar - 2nd edition,” 2004.
- [3] A. Benedetto and F. Benedetto, “Remote sensing of soil moisture content by gpr signal processing in the frequency domain,” *IEEE Sensors Journal*, vol. 11, no. 10, pp. 2432–2441, 2011.
- [4] R. R. Mohan, A. Pradeep, S. Mridula, and P. Mohanan, “Microwave imaging for soil moisture content estimation,” in *2016 IEEE International Symposium on Antennas and Propagation (APSURSI)*, 2016, pp. 865–866.
- [5] J. E. Hipp, “Soil electromagnetic parameters as functions of frequency, soil density, and soil moisture,” *Proceedings of the IEEE*, vol. 62, no. 1, pp. 98–103, 1974.
- [6] M. T. Hallikainen, F. T. Ulaby, M. C. Dobson, M. A. El-rayes, and L. Wu, “Microwave dielectric behavior of wet soil-part 1: Empirical models and experimental observations,” *IEEE Transactions on Geoscience and Remote Sensing*, vol. GE-23, no. 1, pp. 25–34, 1985.
- [7] A. Edwards-Smith, K. Morrison, S. Zwieback, and I. Hajnsek, “Verification of the virtual bandwidth sar scheme for centimetric resolution subsurface imaging from space,” *IEEE Transactions on Geoscience and Remote Sensing*, vol. 56, no. 1, pp. 25–34, 2018.
- [8] M. T. Hallikainen, F. T. Ulaby, M. C. Dobson, M. A. El-rayes, and L. Wu, “Microwave dielectric behavior of wet soil-part 1: Empirical models and experimental observations,” *IEEE Transactions on Geoscience and Remote Sensing*, vol. GE-23, no. 1, pp. 25–34, 1985.

6. TEMPORAL IMAGING FOR GROUND PENETRATING RADAR

- [9] A. Stogryn, “Equations for calculating the dielectric constant of saline water (correspondence),” *IEEE Transactions on Microwave Theory and Techniques*, vol. 19, no. 8, pp. 733–736, 1971.

Chapter 7

Multistatic Polarimetry in Cluttered Ground

7.1 Introduction

The scope of this chapter is to determine if simultaneous multi-static/multi-perspective polarimetric imagery of the subsurface can better detect and discriminate buried and obscured targets. This is investigated via a series of experiments in which novel forward and backscattering GPR configurations with differing incidence angles and polarisations are used to acquire data on a range of calibration and buried landmine targets. *Sun et al.* [1] and *Catapano et al.* [2] both conducted research on forward looking, vehicle mounted GPR systems. The advantage of a forward looking system is that the lost energy backscattered from the ground that does not penetrate the ground can be reduced. Additionally, a more practical attribute to land-mine detection would be, that such a system may not need to be moved over a mine field but could be moved along a side of a potential mine field.

Another important effect that is examined experimentally in this chapter is the effect of increasing subsurface clutter on the polarimetric performance. The general object of GPR

7. MULTISTATIC POLARIMETRY IN CLUTTERED GROUND

signal processing, including SAP or migration, is to present an image that can be readily interpreted or to distinguish the target. The previous chapters have demonstrated how the additional attribute of the electromagnetic wave polarisation can be exploited to enhance target classification ability. The quantification and determination of the clutter limitation of the GPR set-up is dependent to some extent upon the intended GPR application which are likely to be diverse, numerous and ill defined. These uncertainties have been minimised by considering surface clutter only. A series of experiments are performed with an increasing level of surface clutter is introduced in the form of regular sized pebbles above a buried landmine target underneath. Repeated UWB scans of the radar scene are made and the subsurface imaged. It is acknowledged that the result may not hold for other distributions e.g. volumetric, clustered, different sized pebbles and dielectric values etc. However, the radar scene is representative of the lightly clutter environment that can be encountered in realistic scenarios.

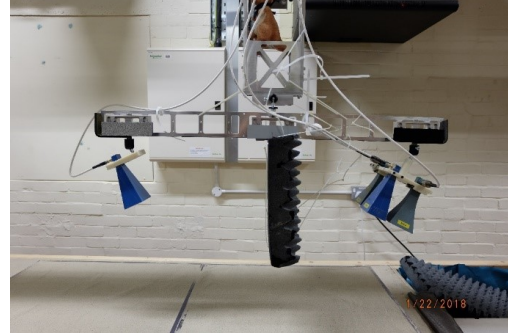
These effects are quantified rigourously via applying polarisation ratios to the data and quantifying the co- and cross-polar responses for different scattering angles, frequencies and polarisation for the different targets.

7. MULTISTATIC POLARIMETRY IN CLUTTERED GROUND

7.2 Methodology



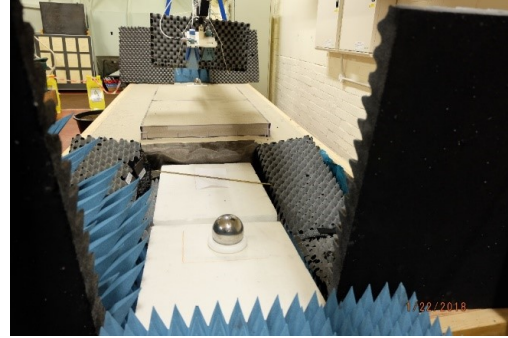
(a) General view of the radar scene.



(b) Close up of the multi-static antennas.



(c) Long view of the radar scene.



(d) View of sphere and rod calibration objects.

Figure 7.1: A range of views of the multi-static full polarimetric GPR setup.

The microwave measurement set up (Figure 7.1) was situated in an open laboratory space of 15 m (l) x 4 m (w) x 5 m (h), which provided a controlled, precision, repeatable, ‘radar-quiet’ measurement environment. The experiments were performed using the UWB technique in High Band (HB), i.e. X-band 8-12 GHz and the antenna arrays were composed of the 3D printed pyramidal horn antennas described in Chapter 3 [3]. The HB spectrum was identified in Chapter 2 as providing a high down range resolution and Mie type high resonance scattering levels from landmine targets of similar dimensions as the wavelength used. Moreover, HB spectrum is representative of many operation remote sensing satellite systems (e.g.

7. MULTISTATIC POLARIMETRY IN CLUTTERED GROUND

TerraSAR-X 9.6GHz [4][5]) and the results may have general applicability.

Because the subsurface target can change the polarisation of the scattered wave to be different from the polarisation of the incident wave, the receiving antenna of a full polarimetric GPR must be designed to receive the different polarisation components of the EM wave [6]. At the same time, to generate EM waves with different polarizations, the transmitting antenna needs to generate signals with components in three orthogonal or basis polarisation directions. Therefore, a full set of scattered radar measurements comprise nine components, which are configured by combining three orthogonal (X,Y,Z) transmitting antennas and three orthogonal (X,Y,Z) receiving antennas. In our GPR setup we will only be operating in the X-Z plane with the two most common basis linear polarisations H-horizontally polarised and V-vertically polarised.

In principle the measurement requires a full polarimetric array system using H and V linear polarisations and must measure four polarimetric modes, HH mode, VV mode, VH mode, and HV mode where the notation has its usual meaning (i.e. the first symbol denotes the polarisation of the transmitting antenna, and the second symbol denotes the polarisation of the receiving antenna). Since the full polarimetric GPR transmit and receive coordinate systems are identical, the role of the transmitting and the receiving antennas can be interchanged. Hence, the HV mode and VH mode have the same function. Consequently, we can reduce the full polarimetric acquisition set to a more compact three polarimetric modes. This only acquires three types of polarimetric GPR data, VV data, HH data, and VH or HV data, at each survey point. Figure 7.1 (b) shows a close up of the array configuration and (c) some of the surface laid calibration objects.

7. MULTISTATIC POLARIMETRY IN CLUTTERED GROUND

7.2.1 Multi-static Measurement Description

The compact polarimetric GPR setup is shown in Figure 7.2 and consists of a 3 m long linear scanner mounted 2.0 m above a 3.8 m (l) x 1.2 m (w) x 0.8 m (h) sand trough filled with kiln-dried sand, a vector network analyser and computer control unit. A ZVL Rohde and Schwarz network analyser was used as the radar receiver with a HB frequency bandwidth 8.2-12.4 GHz and in stepped frequency waveform mode. Data samples were acquired along the aperture at dx intervals, set at 1 cm. The antennas stop at each point along the aperture, transmit a set of 801 spot frequencies at 5.0 MHz steps over the HB spectrum, then move on dx and repeat the process until 289 samples have been collected over a 300 cm aperture. A B-scan image is not collected instantaneously, but takes several minutes to collect, during which time RF and mechanical stability of the radar and buried landmines must be maintained. Each scan provides a single-look A-scan.

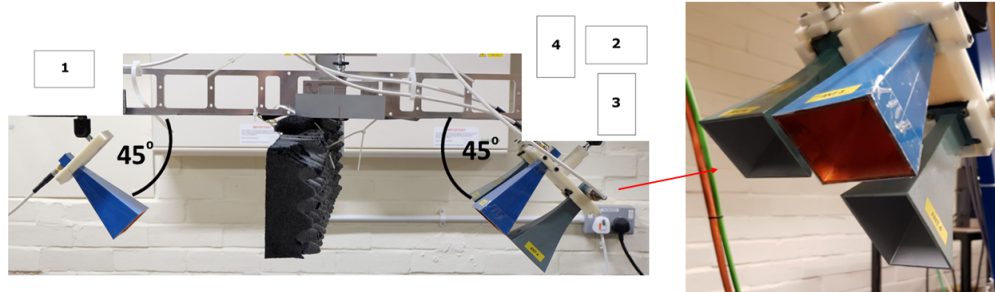


Figure 7.2: (a) Multistatic polarimetric antenna array (b) Monostatic polarimetric antenna array. The distance between the bistatic array was 72 cm and the array heads were 35.5 cm above the surface of the sand.

The antenna array is a novel combination of monostatic and bistatic configurations shown in Figure 7.2. The transmit and receive array are inclined at 45° to the horizontal and have a radar absorbent material (RAM) baffle located centrally between the bistatic array. This size, length and positioning of the baffle was arrived at by trial and error to reduce mutual coupling and stray multi-path propagation from the support boom. The antenna array has three scattering setting, and measures six types of polarimetric modes as described below;

7. MULTISTATIC POLARIMETRY IN CLUTTERED GROUND

1. Backscatter monostatic – VV mode and HV mode – uses all three antennas on the right shown in Figure 7.2.
2. Backscatter monostatic – HH mode and VH mode – uses all three antennas on the right shown in Figure 7.2 but with the array head rotated around by 90° .
3. Forward scatter bistatic – VV mode and VH – uses the antenna on the left in Figure 7.2(a) and two antennas from the right of Figure 7.2(b).

The multistatic polarimetric GPR data sets acquired are a co-registration of the same polarisation basis taken looking at the same ground scene, or footprint, but from a different scattering geometry. The advantage of this combined multi-static GPR configuration is we can use the different polarisation attributes and the different geometric scattering basis of the subsurface target to detect and distinguish the subsurface target.

The radar scene is shown in progress in Figure 7.3, included below the picture is a schematic indicating the location of a number of calibration objects, reference objects and the target anti-personnel landmine. The target and trihedral were both buried at a depth of approximately 15 cm. In addition to objects buried in sand there were also some reference objects placed on RAM. A summary of these objects and the expected response is given in Table 7.1.

The arrangement of these objects allows the system precise calibration to range. Note that the bistatic range to specular ground return will look larger due to bistatic geometry. The monostatic cable length, which is the cable length from the VNA to the monostatic antenna array, is 10.78 m and the bistatic cable length, which is the cable length from the VNA to the antennas separated by the beam used in this chapter, is 11.03 m. Hence, new range to specular ground is 0.5056 m. Thus the ground return appears further away by 0.1506 m. The range profiles align with the ground if the cable length is $11.03 + 0.1506 + 0.06 = 11.2406\text{m}$. Where the extra 6 cm is not accounted for but it is suggestive that the phase center for each

7. MULTISTATIC POLARIMETRY IN CLUTTERED GROUND

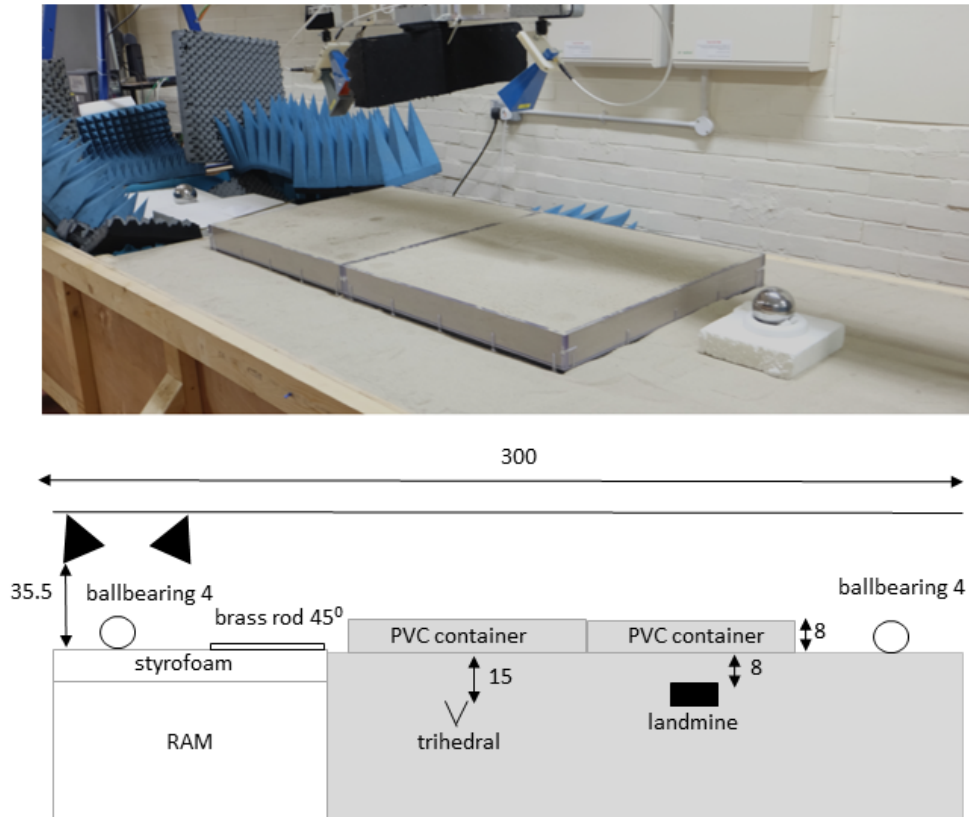


Figure 7.3: Radar scene and schematic diagram of object locations (Dimensions in cm).

horn antenna lies approximately 3 cm behind their aperture. This deduction is consistent with the horn antenna phase center determination given in Chapter 3. The difference in cable length between monostatic and bistatic thus is 0.4606 m and this is the range correction factor which needs to be applied to range profiles to co-register the B-scan polarimetric imagery.

7. MULTISTATIC POLARIMETRY IN CLUTTERED GROUND

Type	Object	Response
Calibration	Sphere (40 mm)	Co-polar calibration target HH, VV provides equal response HV, VH provides no response
Calibration	Rod inclined on the horizontal at 22.5°	Cross-polar calibration target HH, VV provides no response HV, VH provides some response
Reference	Trihedral	Will return equally in both cross and co-polar
Target	PMN-2	Will provide some unknown response
Reference	Sphere (40 mm)	As for calibration sphere but use for reference

Table 7.1: Polarimetric response of objects in the radar scene.

7.3 The Experiments

7.3.1 Experiment 7 D - Multistatic Full Polarimetry Configuration

The optimum scene setup described above was arrived at after several trial and error scanning surveys and analysis of B-scan data. Specifically adjustment of the radar absorbent sheet position and its length was critical to blocking side-lobe radiation from the horn antennas. Several different look angles were investigated, specifically 30° , 45° and 60° inclinations. The 30° inclination proved to be too shallow and the ground footprint too large resulting in very strong ground reflection and weak subsurface signals. The 60° inclination provided a stronger signal but much more side-lobe clutter was present in the scattered signals. Experimentally the 45° inclination provided the lowest clutter level and good signal-clutter performance. This array configuration was obviously related to the types of antennas used and selection of other antennas will likely require adjustments. A multistatic 2D scanning survey was then carried out for Experiment D using this optimum configuration with no ground or surface clutter present in the radar scene.

7. MULTISTATIC POLARIMETRY IN CLUTTERED GROUND

7.3.2 Experiment 7 E – Multistatic Full Polarimetry in Ground Clutter

Experiment 7 E using the same radar scene as described in Experiment 7 D, however, surface clutter is now introduced and incrementally increased onto the sand surface. The clutter is composed of beach pebbles of 6 cm or less randomly distributed over the surface of the sand tray centred above the buried PMN-2 anti-personnel landmine as shown in Figure 7.4. The sand tray is 70 cm x 70 cm in square area. The experiment clutter type and distribution are listed in Table 7.2.

Experiment No.	Clutter type	Surface area %
1	large rock	area of landmine
2	pebbles	10%
3	pebbles	20%
4	pebbles	30%
5	pebbles	40%
6	pebbles	80%
7	pebbles	100%

Table 7.2: List of surface clutter experiments conducted.

7. MULTISTATIC POLARIMETRY IN CLUTTERED GROUND

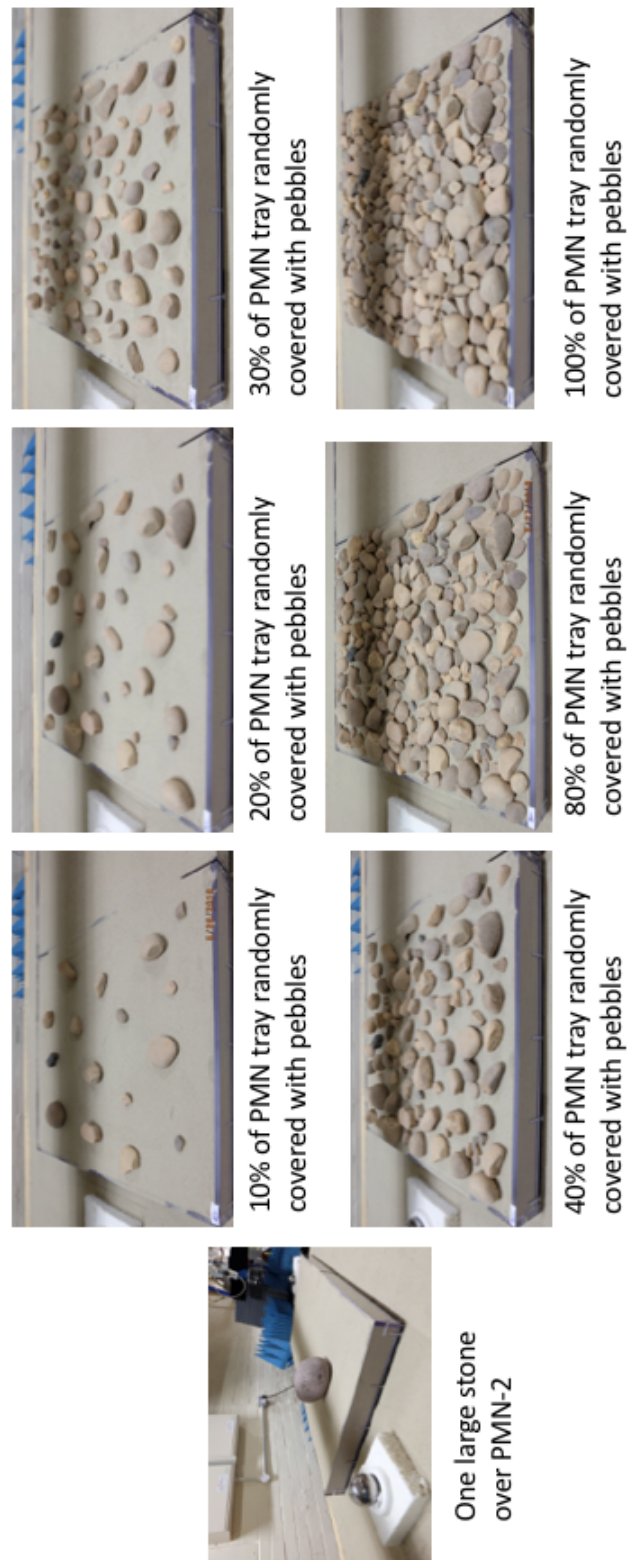


Figure 7.4: Random pebble surface clutter distributions above the buried PMN-2 anti-personnel landmine.

7. MULTISTATIC POLARIMETRY IN CLUTTERED GROUND

7.4 Results and Performance Discussion

7.4.1 Experiment 7 D - Multistatic Full Polarimetry Configuration

7.4.1.1 B-scan Image Analysis

Figure 7.5 shows the bistatic VV and VH polarisation channel B-scan images. Due to the geometric symmetry no slant angle is apparent in the measurement. In addition to the calibration and reference objects that are clearly identifiable, there is also a good detection of the PMN-2 landmine. In VV all the targets have limited hyperbola features and are well localised. Interestingly, the landmine has a strong backscatter signal in this polarisation basis while the trihedral is poor. In the bistatic VH polarisation channel there is negligible detection of the PMN-2 landmine.

Figure 7.6 shows the monostatic HH and HV polarised channels. Note that the targets appear slanted in the image and this is due to the array inclination angle of 45° . All the targets are present as scattering hyperbola but there appears to be some ghost numerical artifacts down range of the trihedral, rod and sphere. However the target PMN-2 landmine is present but not well defined between the sphere and trihedral.

All B-scan polarisation channels have some weak antenna coupling present. The subsurface clutter present surrounding the buried objects is a combination of (i) residual artefact of the FFT processing and (ii) reflection and interactions of waves in the subsurface.

7. MULTISTATIC POLARIMETRY IN CLUTTERED GROUND

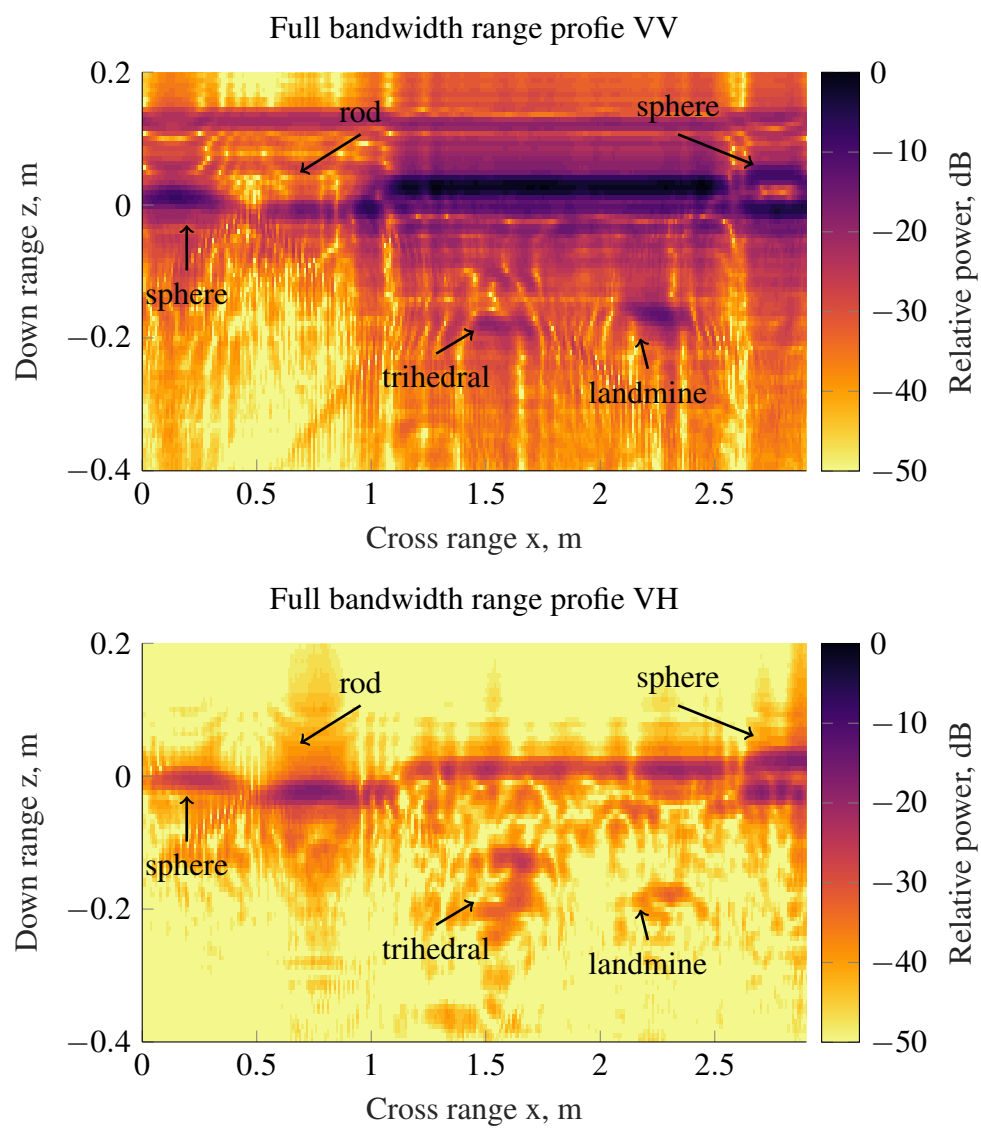


Figure 7.5: Calibrated VV and VH B-scans.

7. MULTISTATIC POLARIMETRY IN CLUTTERED GROUND

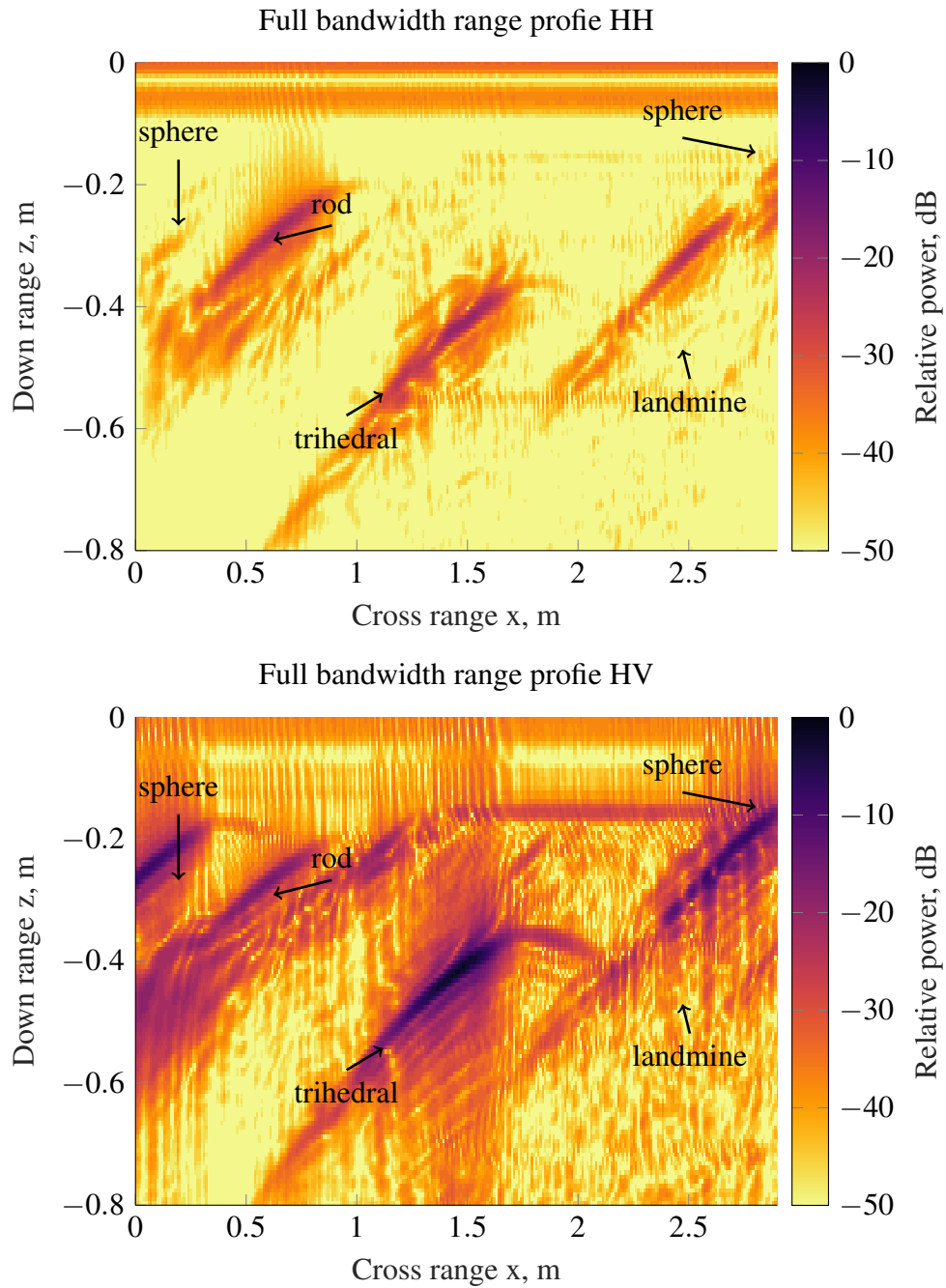


Figure 7.6: Calibrated HH and HV B-scans.

7. MULTISTATIC POLARIMETRY IN CLUTTERED GROUND

7.4.2 Experiment 7 E - Multistatic Full Polarimetry in Clutter

7.4.2.1 B-scan Image Analysis

Figure 7.7 shows the bistatic VV B-scans for 10% and 20% clutter introduced on the surface. The buried land-mine is still clearly distinguishable from the surrounding clutter. Figure 7.8 shows the bistatic VV B-scans for 30% and 40% clutter introduced to the surface. It can be seen, that the threshold for the used measuring set-up is 30% introduced clutter, as the buried land-mine can not be resolved anymore for the 40% clutter case.

7.5 Polarisation Ratios

To attempt to derive target specific parameters in the next step it was looked at polarisation ratios of the targets placed in the scene. Specifically the target ratios for the buried land-mine and the calibration sphere are listed in table 7.3. The polarisation ratios (e.g. VH/VV , HV/HH , VV/HH) have been calculated to the multi-static set-up for the empty test bed and all possible percentages of introduced clutter. The polarisation ratios of the surface laid sphere are constant over all percentages of introduced clutter, and serve as a reference point for the values of the buried land-mine. From the VV/HH ratio of the sphere it can be seen that the channels are well balanced. It is remarked that the values of the VV/HH ratio for the land-mine is positive in some of the percentages of cluttered surface and since the polarisation for the sphere is constant, this seems to result from target specific parameters. The table also shows comparison results for the monostatic measurement set-up introduced in chapter 5. Again the polarisation ratio for the VV/HH case of the land-mine is positive and in performing the same sort of measurements on a range of buried targets, some specific parameters might be derived to enable one to distinguish these from each other.

7. MULTISTATIC POLARIMETRY IN CLUTTERED GROUND

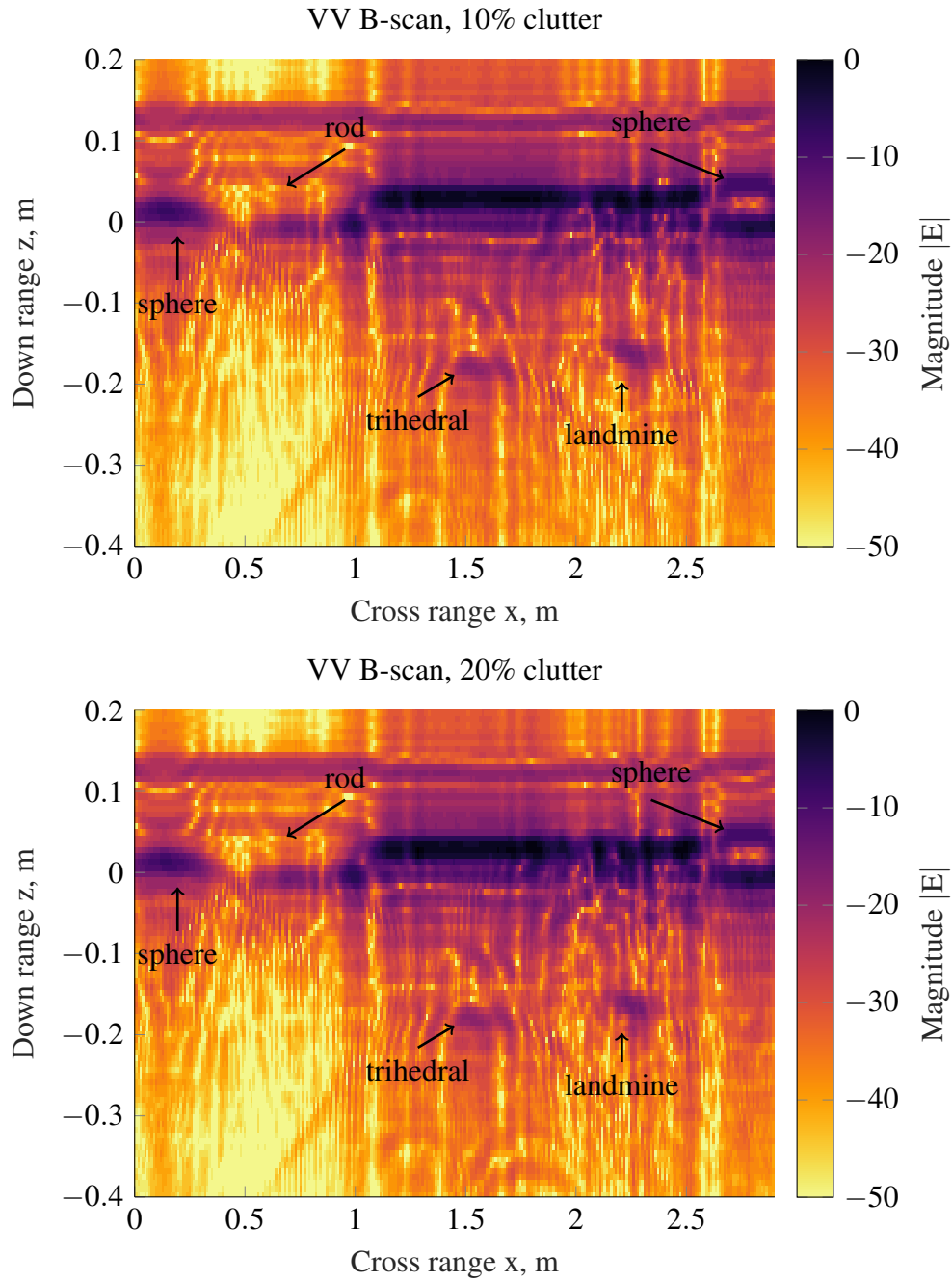


Figure 7.7: Calibrated VV B-scans.

7. MULTISTATIC POLARIMETRY IN CLUTTERED GROUND

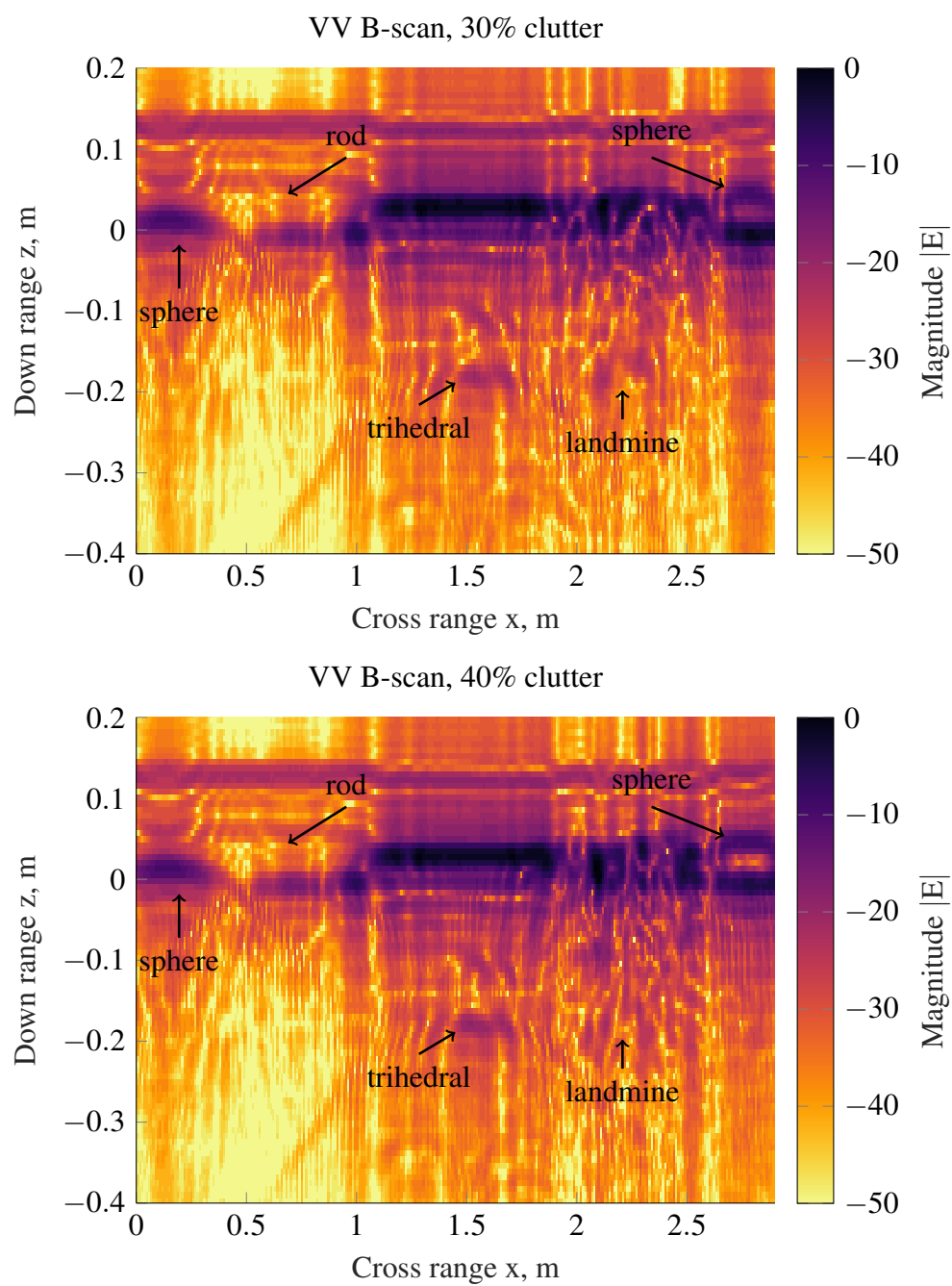


Figure 7.8: Calibrated VV B-scans.

set-up	Target	Pol Ratio	w/o	One Stone	10%	20%	30%	40%	80%	100%
multi-static	mine	VH/VV	-19.49	- 8.82	- 8.65	- 7.72	- 3.52	- 5.15	- 2.69	- 2.06
		HV/HH	-13.83	-21.54	-35.36	-29.73	-26.92	-23.2	-30.69	-31.82
		VV/HH	10	- 5.92	4.94	1.94	-6.44	- 7.22	- 5.45	- 4.40
	sphere	VH/VV	-15.94	-15.88	-15.94	-15.72	-14.44	-15.81	-15.74	-14.37
		HV/HH	-15.89	-15.84	-29.57	-16.05	-16.62	-15.95	-16.08	-15.77
		VV/HH	0	0	- 0.09	- 0.4	- 0.40	- 0.29	- 0.08	0.16
	mine	VH/VV	-27.99							
		VH/HH	-23.98							
		VV/HH	2.18							
monostatic										
	sphere	VH/VV	-29.09							
		HV/HH	-25.19							
		VV/HH	0							

Table 7.3: List of polarisation ratios for sphere and a buried landmine at 45° and 0°.

7. MULTISTATIC POLARIMETRY IN CLUTTERED GROUND

7.6 Summary Comments

This chapter has extended the GPR diversity by integrating multi-perspective imaging of the subsurface. A compact full polarimetric GPR arrays has been developed with polarimetric channels in VV, VH, HH and HV. S-parameters measurements are made of the radar scene in back scattering, monostatic, and forward scattering, bistatic, coordinate frames.

In Experiment D the B-scan results of of an empty scene were taken and compared. The bistatic VV polarisation channel provided the clearest imagery and the strongest land-mine return, whilst the monostatic polarisations returns for the land-mine were generally weaker.

In Experiment E the potential of the polarimetric techniques to suppress or alleviate clutter obscuring a buried anti-personnel land-mine was investigated. The radar scene was repeatedly scan surveyed with increasing levels of surface clutter. It was demonstrated that the threshold surface clutter level that obscured the landmine was approximately 30% of surface area covered with pebbles.

In a further stage it was attempted to derive target specific parameters by looking at polarisation ratios. It was shown that the system channels were well balanced and that there is a potential to derive target specific parameters for buried objects by looking a polarisation ratio in the co-polar case.

7. MULTISTATIC POLARIMETRY IN CLUTTERED GROUND

References

- [1] Y. Sun and J. Li, “Time-frequency analysis for plastic landmine detection via forward-looking ground penetrating radar,” *IEE Proceedings - Radar, Sonar and Navigation*, vol. 150, no. 4, pp. 253–, 2003.
- [2] I. Catapano, F. Soldovieri, and M. A. González-Huici, “Microwave tomography enhanced forward looking gpr: A feasibility analysis,” in *Proceedings of the 15th International Conference on Ground Penetrating Radar*, 2014, pp. 964–968.
- [3] S. G. Wirth, I. L. Morrow, and I. Horsfall, “Fabrication procedure and performance of 3d printed x-band horn antenna,” in *The Loughborough Antennas Propagation Conference (LAPC 2018)*, 2018, pp. 1–4.
- [4] P. Rizzoli, B. Bräutigam, S. Wollstadt, and J. Mittermayer, “X-band backscatter map generation using terrasar-x data,” in *2010 IEEE International Geoscience and Remote Sensing Symposium*, 2010, pp. 3450–3453.
- [5] M. Weber, “Terrasar-x and tandem-x: Reconnaissance applications,” in *2007 3rd International Conference on Recent Advances in Space Technologies*, 2007, pp. 299–303.
- [6] S. G. Wirth, I. L. Morrow, and I. Horsfall, “Near-field microwave imaging using a polarimetric array of 3d printed antennas and lenses,” in *The Loughborough Antennas Propagation Conference (LAPC 2018)*, 2018, pp. 1–6.

Chapter 8

Conclusions and Future Work

8.1 Research Summary

The research has effectively demonstrated that by combining GPR systems employing multi-static array configurations and multi-polarisation channels we can obtain subsurface reconstructed landmine range profiles, from which we can use polarisation attributes and geometric features to enhance the ability of subsurface target classifications from near-field stand-off GPR.

On polarisation decomposition techniques;

- The ability to acquired a full polarimetric data enables the polarisation attributes of subsurface objects and their scattering mechanisms to be presented and more readily interpreted and distinguish the landmine from the clutter. In particular, Experiments 5A and 5B performed a world's first time, demonstrations of subsurface polarimetric decomposition which exposes the scattering characteristics of a subsurface object.
- Stokes, Pauli and Yamaguchi polarimetric decompositions were investigated to provide clutter suppression on data collected for shallow buried land-mines in sand. It was shown, that the air-ground-interface and the antenna cross talk can effectively be

8. CONCLUSIONS AND FUTURE WORK

suppressed co- and cross-polar products while the various scattering mechanisms can be localised.

- Moreover, a novel form of differential polarimetry and decomposition technique was also applied and observed to provide complementary interpretation of subsurface scattering mechanisms.

On Moisture Change based Detection and Imaging;

- A new microwave subsurface imaging product was described which is evolved via time lapsed microwave measurements, over several days, of the soil subsurface. The technique exploits changes in soil moisture levels that occur naturally due to evaporative and percolation processes. A novel mathematical technique was investigated for detecting and discriminating buried targets; it provides a scaled phase weighting procedure to form a cumulative B-scan image of the subsurface.
- The moisture change land-mine detection experiment 6 C provided inconclusive results using the technique. There are two reasons that account for this; Firstly, the experiments were conducted at lower microwave frequencies and the dielectric phase change was relatively small due to small amount of water added. Secondly, in hindsight, locating the buried landmine close to the metallic GPR support stand introduced multipath clutter. Nor did migration resolve the issue since the landmine was on the measurement boundary.
- This inconclusive result altered the research methodology. There was little point to apply a SAP algorithm to poor Bscan polarimetric data. Rather emphasis was placed on achieving good polarimetry measurements and applying and understanding individual polarimetry processing techniques. Of course, migration can still be applied to the polarimetry product.

8. CONCLUSIONS AND FUTURE WORK

- The application of radar absorbent material around the support stand and too isolate calibration targets in the scene much improved the situation in the experiments in Chapter 5 and 6.
- Dual polarisation GPR sensors are able to detect buried targets with polarisation properties. However, targets may not always possess dual polar characteristics in the plane of polarisation that the measurements are taken in. Thus, a fully polarimetric survey of the radar scene is recommended as necessary to completely capture a buried target response.
- 3D printed pyramidal horn antennas were designed and built to form a compact full polarimetric array. The array was used to take CFP measurements in experiments in Chapter 5, 6 and 7. The array demonstrated performance comparable to commercial metal horn antennas and are lightweight and lower cost than commercial horns.
- The Dobson model proved to be a very useful and precise tool to predict phase change in the soil medium surrounding the landmine and results compared very well with measurements.

Taken together these techniques provide significant performance enhancements at least in subsurface image contrast.

8.2 Future Research

As with all 3-4 year research programmes there will inevitably be avenues of research that produce promising and interesting results that merit further investigation and others that, reach a dead end.

Relating to moisture change detection demonstrated in Chapter 6 and the results of experiments suggest potential future investigation;

8. CONCLUSIONS AND FUTURE WORK

- Further research effort on methods to quantify the image improvements and clutter reduction performance of the polarisation decomposition techniques. This is a relatively new topic to the remote sensing community and there is little reported on the subject.
- The use of polarimetric decomposition and attribute analysis methods have only recently begun to be used in GPR for demining and prospecting. This research trend is only likely to increase in future years.
- The Dobson phase change model can be use proactively to predict the likely success of the moisture change detection technique in various regions of the world before a GPR field campaign is planned.
- The 3D printed horn antenna array is very lightweight compared to similar commercial metal arrays. It would be well suited for use on a UAV or autonomous vehicle platform.

Relating to the multi-static polarimetric GPR;

- Research into other multi-static GPR configurations using compact full polarimetric in both monostatic and bistatic arrays is recommend. The number and configuration will depend on the power resources available to the GPR.
- The deployment of 3D printed antenna types with GPR systems maintain light weight, low cost, acceptable performance sensors capable of fitment to UAV or autonomous vehicle. Research is recommend into other GPR antenna types suitable for 3D printing; especially electrically small planar spiral and bowtie and tapered slot antennas.
- The experiment considered only one type of soil in which the landmine is buried. Further experiments and analysis are recommended by varying the soil type or artificially increasing conductivity to identify how this will impact the response of the GPR.

8. CONCLUSIONS AND FUTURE WORK

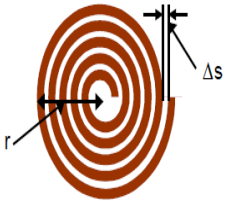
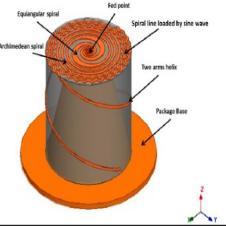
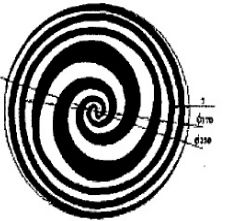
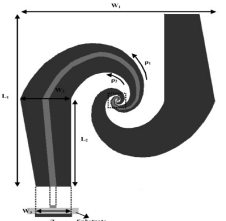
- Chapter 5 and Chapter 6 have highlighted the potential of polarimetry decomposition as a powerful tool to analyse subsurface GPR data for the presence of man made objects and their scattering characteristics. Research is recommended into more recently reported polarimetry decomposition techniques such as Freeman decomposition that may offer superior clutter suppression.
- The extension of the present research into other ways to suppress clutter arising in regions of random propagation (and exploit polarisation) in a form of inverse diffusion propagation similar to Brownian motion might be an option.

Appendices

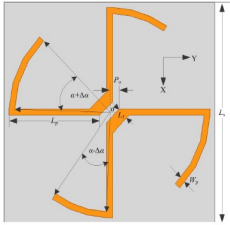
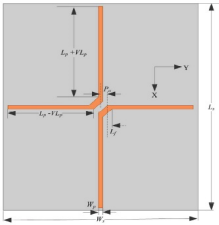
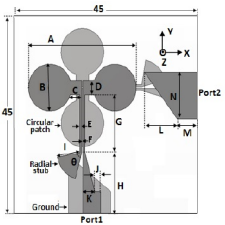
A.1 Antennas

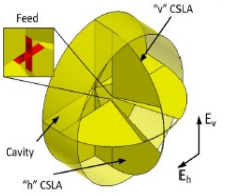
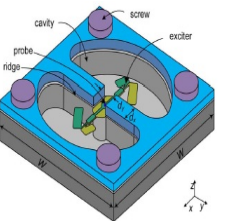
This chapter gives a comprehension of all antennas reviewed for chapter 3. The reader can use this chapter as a reference to get a quick overview of different antenna types, produced from different materials and in different sizes and shapes. For each antenna a picture is shown and the following properties are displayed: impedance bandwidth, frequency range, size, time domain or frequency domain and gain. A smiley indicates, the specific antenna design could be used for UWB GPR. A frowny means the antenna would be insufficient for our application. In case one of the aforementioned parameters is not disclosed in the referenced source this is indicated in the table as N.A. for "not available".

A.1.1 Spiral antenna papers

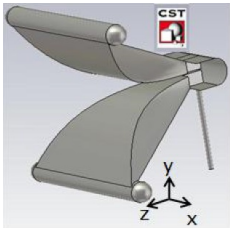
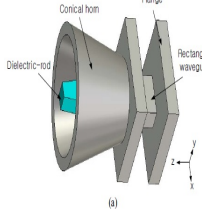
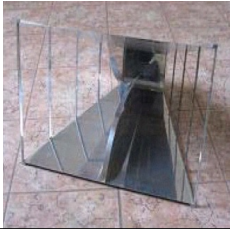
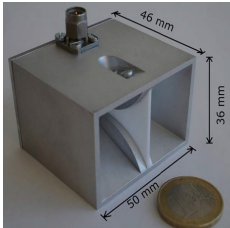
	Antenna	Imp BW	Freq Range	Size	TD/FD	Gain	Application	suitable	Paper
01		112%	3.1 - 10.6 GHz		FD	N.A.		☺	[1]
02		141%	1-18.5 GHz		FD	avg. 6dB		☺	[2]
03		103% 36%	0.4-2 GHz	N.A.	FD	N.A.		☺	[3]
04		131.94%	3.75-18.6 GHz	84.6 mm x 43.26 mm x 0.787 mm	FD/TD	3.5-7 dBi		☺	[4]

A.1.2 Crossed dipole papers

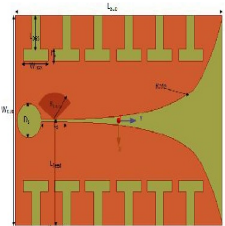
	Antenna	Imp BW	Freq Range	Size	TD/FD	Gain	Application	suitable	Reference
01		11%	2.26 - 2.53 GHz	32mm x 32 mm x 1 mm	FD	max. 1.877 dB at 2.4 GHz max. 1.813 dB at 2.48 GHz		☹	[5]
02		24%	2.163-2.753 GHz	52 mm x 44 mm	FD	max. 1.984 dB at 2.48 GHz		☺	[6]
03		56.95%	5.4 - 9.7 GHz	45 mm x 45 mm	FD	3.7 dB (6.5 GHz) 4 dB (8 GHz)		☺	[7]

	Antenna	Imp BW	Freq Range	Size	TD/FD	Gain	Application	suitable	Reference
04		101%	0.5 - 2 GHz	$r = 150 \text{ mm}$	FD	N.A.		☺	[8]
05		35.4%	27-36.8GHz	18 mm x 18 mm x 3.9 mm	FD	12.4 dB		☺	[9]

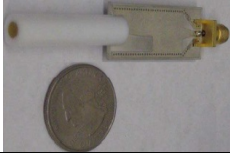




A.1.3 Horn antenna papers

	Antenna	Imp BW	Freq Range	Size	TD/FD	Gain	Application	suitable	Reference
01		153.49%	2 - 19 GHz	N.A.	FD	N.A.		☺	[10]
02		16.22%	33 - 40 GHz	d = 20 mm l = 23.11 mm	FD	15 dBi at 37.4 GHz	NF	☺	[11]
03		175.59%	0.26 - 4 GHz	N.A.	FD/TD	max. 12 dBi at 2 GHz		☺	[12]
04		N.A.	6-20 GHz	H: 36mm L: 50 mm W: 46 mm	FD	max. 16.77 dBi at 20 GHz	FF	☺	[13]

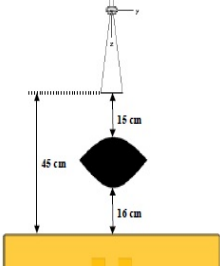

A.1.4 Vivaldi antenna papers

	Antenna	Imp BW	Freq Range	Size	TD/FD	Gain	Application	suitable	Reference
01		22% 130%	35 - 300 MHz	W: 525 L: 750	FD	4 dBi (35 MHz) 6 dBi (130 MHz)		☺	[14]


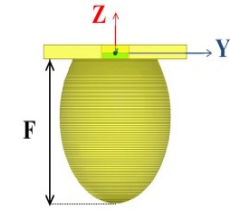
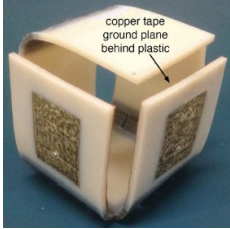
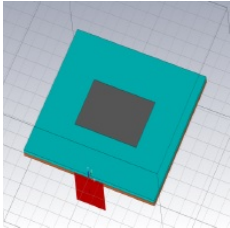
A.1.5 Dielectric rod antenna papers

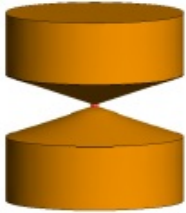
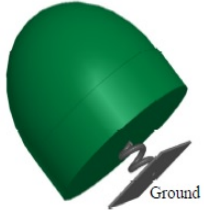

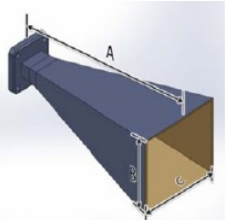
	Antenna	Imp BW	Freq Range	Size	TD/FD	Gain	Application	suitable	Reference
01		56.41%	7 - 12.5 GHz	d1 = 4 mm d2 = 8 mm	FD	4.76 (10 GHz)		☺	[15]
02		N.A.	7 - 12.5 GHz	d1 = 4 mm d2 = 8 mm	FD	4.0 GHz (10 GHz)		☺	[15]
03		N.A.	7 - 12.5 GHz	d1 = 4 mm d2 = 8 mm	FD	4.76 dBi (10 GHz)		☺	[15]
04		N.A.	7 - 12.5 GHz	d = 8 mm	FD	4.43 dBi (10 GHz)		☺	[15]
05		17.86%	5.1 - 6.1 GHz	r = 20 mm		16.7 dBi at 5.6 GHz range 15.9 - 17.2 dBi		☹	[16]

A.1.6 Lense papers

	Lenses	Imp BW	Freq Range	Size	TD/FD	Gain	Application	suitable	Reference
01		N.A.	8 - 12 GHz	d = 28 cm H: 15 cm		N.A.	NF	☺	[17]
02		N.A.	12 - 18 GHz	d = 12 cm H: 18.5 cm		8 - 10 dBi	NF	☺	[18]

A.1.7 3D printed antenna papers:

	Antenna	Imp BW	Freq Range	Size	TD/FD	Gain	Application	suitable	Reference
01		96%	3.2 - 12.6 GHz	25 mm x 45 mm x 45 mm	FD	1.4 dBi at 3.1 GHz -0.5 dBi at 6.85 GHz -1.7 dBi at 10.6 GHz		☺	[19]
02		16%	115 - 135 GHz	2.2 mm x 2.2 mm x 10 mm	FD	12.5 dBi at 115 GHz 17.5 dBi at 125 GHz 11 dBi at 135 GHz		☹	[20]
03		3.96%	2.23 - 2.32 GHz	5.7 cm x 5.7 cm thickness: 3 mm	FD	4.2 dBi at 2.31 GHz		☹	[21]
04		15.85%	2.15 - 2.52 GHz	116.25mm x 90mm x 1.5mm	FD	N.A.		☹	[22]

	Antenna	Imp BW	Freq Range	Size	TD/FD	Gain	Application	suitable	Reference
05		180%	0.430- 8.4 GHz 0.770 - 26.5 GHz	$r = 9 \text{ cm}$ $h = 20 \text{ cm}$	FD	N.A.		☺	[23]
06		108%	6 - 20 GHz	35 mm x 81 mm	FD	16.4 dBi at 9.4 GHz		☺	[24]
07		24.18%	6.8 - 8.7 GHz	2 cm x 2 cm x 1 cm	FD	N.A.		☺	[25]
08		N.A.	12 - 15 GHz	145.1 x 52.8 X 66.2	FD	19.02		N.A.	[26]

	Antenna	Imp BW	Freq Range	Size	TD/FD	Gain	Application	suitable	Reference
09		55.42 %	3 - 5.3 GHz	80 mm x 120 mm	FD	N.A.		☺	[27]
10		117%	700 - 2700 MHz	20cm x 20 cm x 3.175 cm	FD	5dB at 2.7 GHz		☺	[28]
11	 (a)	N.A.	16GHz	40 mm x 40 mm x 5 mm	FD	10dB		☺	[29]

References

- [1] M. Karlsson and Shaofang Gong, “An integrated spiral antenna system for uwb,” in *2005 European Microwave Conference*, vol. 3, 2005, pp. 4 pp.–2010.
- [2] Na Liu, Pengfei Yang, and Weijiang Wang, “Design of a miniaturized ultra-wideband compound spiral antenna,” in *2013 IEEE INTERNATIONAL CONFERENCE ON MICROWAVE TECHNOLOGY COMPUTATIONAL ELECTROMAGNETICS*, Aug 2013, pp. 255–258.
- [3] Song Zhao-hui, Qiu Jing-hui, and Li Hong-mei, “Novel planar complex spiral ultra-wideband antenna,” in *ICMMT 4th International Conference on, Proceedings Microwave and Millimeter Wave Technology, 2004.*, Aug 2004, pp. 35–38.
- [4] S.-G. Mao, J.-C. Yeh, and S.-L. Chen, “Ultrawideband circularly polarized spiral antenna using integrated balun with application to time-domain target detection,” *Antennas and Propagation, IEEE Transactions on*, vol. 57, no. 7, pp. 1914–1920, July 2009.
- [5] G. Pan, Y. Li, Z. Zhang, and Z. Feng, “Isotropic radiation from a compact planar antenna using two crossed dipoles,” *Antennas and Wireless Propagation Letters, IEEE*, vol. 11, pp. 1338–1341, 2012.
- [6] ———, “An isotropic-radiated planar antenna using two crossed dipoles,” in *Microwave and Millimeter Wave Technology (ICMMT), 2012 International Conference on*, vol. 3, May 2012, pp. 1–4.
- [7] R. Kumar, B. Huyart, J. Cousin, and K. Mabrouk, “Dual-circular polarized dumbbell-shaped crossed-dipole planar antenna for uwb application,” in *Antennas and Propagation (EuCAP), 2013 7th European Conference on*, April 2013, pp. 1474–1478.
- [8] A. Elsherbini and K. Sarabandi, “Dual-polarized coupled sectorial loop antennas for uwb applications,” *Antennas and Wireless Propagation Letters, IEEE*, vol. 10, pp. 75–78, 2011.

-
- [9] X. Bai, S.-W. Qu, and R.-L. Xia, "Ka-band cavity-backed detached crossed dipoles for circular polarization," *Antennas and Propagation, IEEE Transactions on*, vol. 62, no. 12, pp. 5944–5950, Dec 2014.
- [10] A. A. Jamali and R. Marklein, "Design and optimization of ultra-wideband tem horn antennas for gpr applications," in *2011 XXXth URSI General Assembly and Scientific Symposium*, 2011, pp. 1–4.
- [11] H. Lee and H. Lee, "A compact dielectric rod-loaded conical horn antenna for millimeter-wave applications," in *Proceedings of 2012 5th Global Symposium on Millimeter-Waves*, 2012, pp. 182–185.
- [12] M. Strycek, I. Hertl, R. Pavlik, and V. Polacek, "Tapered slot antennas for ground penetrating radar," in *Ground Penetrating Radar (GPR), 2010 13th International Conference on*, June 2010, pp. 1–4.
- [13] B. Panzner, A. Jöstingmeier, and A. Omar, "A tiny double-ridged horn antenna for sub-surface radar applications," in *Antennas and Propagation (EuCAP), 2013 7th European Conference on*, April 2013, pp. 1322–1325.
- [14] D. M. Elsheakh and E. A. Abdallah, "Novel shape of vivaldi antenna for water detection using gpr," in *The 2nd Middle East Conference on Antennas and Propagation*, 2012, pp. 1–4.
- [15] R. Kazemi and A. Fathy, "Dielectric rod antenna with substrate integrated waveguide planar feed for wide band applications," in *Antennas and Propagation Society International Symposium (APSURSI), 2012 IEEE*, July 2012, pp. 1–2.
- [16] C. Kumar, V. V. Srinivasan, V. K. Lakshmeesha, and S. Pal, "Design of short axial length high gain dielectric rod antenna," *IEEE Transactions on Antennas and Propagation*, vol. 58, no. 12, pp. 4066–4069, Dec 2010.

-
- [17] A. Teggatz, A. Jostingmeier, and A. S. Omar, "Application of a dielectric lens for focusing of a gpr," in *2007 IEEE Antennas and Propagation Society International Symposium*, 2007, pp. 1461–1464.
- [18] S. Zhang, Y. Vardaxoglou, W. Whittow, and R. Mittra, "3d-printed flat lens for microwave applications," in *2015 Loughborough Antennas Propagation Conference (LAPC)*, 2015, pp. 1–3.
- [19] A. Garcia Lopez, E. Lopez C, R. Chandra, and A. Johansson, "Optimization and fabrication by 3d printing of a volcano smoke antenna for uwb applications," in *Antennas and Propagation (EuCAP), 2013 7th European Conference on*, April 2013, pp. 1471–1473.
- [20] A. Bisognin, D. Titz, C. Luxey, G. Jacquemod, F. Ferrero, D. Lugara, A. Bisognin, R. Pilard, F. Giancesello, D. Gloria, J. Costa, C. Laporte, H. Ezzeddine, E. Lima, and C. Fernandes, "A 120 ghz 3d-printed plastic elliptical lens antenna with an ipd patch antenna source," in *Ultra-WideBand (ICUWB), 2014 IEEE International Conference on*, Sept 2014, pp. 171–174.
- [21] J. Kimionis, M. Isakov, B. Koh, A. Georgiadis, and M. Tentzeris, "3d-printed origami packaging with inkjet-printed antennas for rf harvesting sensors," *Microwave Theory and Techniques, IEEE Transactions on*, vol. 63, no. 12, pp. 4521–4532, Dec 2015.
- [22] K. A. Nate, J. Hester, M. Isakov, R. Bahr, and M. M. Tentzeris, "A fully printed multilayer aperture-coupled patch antenna using hybrid 3d / inkjet additive manufacturing technique," in *Microwave Conference (EuMC), 2015 European*, Sept 2015, pp. 610–613.
- [23] J. Andriambeloson and P. Wiid, "Hyperband conical antenna design using 3d printing technique," in *Radio and Antenna Days of the Indian Ocean (RADIO), 2015*, Sept 2015, pp. 1–2.

-
- [24] M. Farooqui and A. Shamim, "A 3d printed helical antenna with integrated lens," in *Antennas and Propagation USNC/URSI National Radio Science Meeting, 2015 IEEE International Symposium on*, July 2015, pp. 324–325.
- [25] M. Mirzaee, S. Noghanian, L. Wiest, and I. Chang, "Developing flexible 3d printed antenna using conductive abs materials," in *Antennas and Propagation USNC/URSI National Radio Science Meeting, 2015 IEEE International Symposium on*, July 2015, pp. 1308–1309.
- [26] C. Garcia, R. Rumpf, H. Tsang, and J. Barton, "Effects of extreme surface roughness on 3d printed horn antenna," *Electronics Letters*, vol. 49, no. 12, pp. 734–736, June 2013.
- [27] W.-S. Chen and C.-H. Kao, "A study of the broadband printed rectangular slot antenna with a 3d microstrip-line feed," in *Antennas and Propagation Society International Symposium, 2005 IEEE*, vol. 2A, July 2005, pp. 545–548 vol. 2A.
- [28] J.-M. Floch, B. El Jaafari, and A. El Sayed Ahmed, "New compact broadband gsm/umt-s/lte antenna realised by 3d printing," in *Antennas and Propagation (EuCAP), 2015 9th European Conference on*, April 2015, pp. 1–4.
- [29] J. Wu, X. Yu, M. Liang, and H. Xin, "Antenna radiation pattern control through 3d printed inhomogeneous dielectrics," in *Radio Science Meeting (Joint with AP-S Symposium), 2015 USNC-URSI*, July 2015, pp. 353–353.